Manufacturing of silk particles using diamond turning

by

Zhengjian Wang

Submitted to the Department of Design, Manufacturing and Engineering Management in partial fulfilment of the requirements for the degree of

Doctor of Philosophy in Mechanical Engineering

at the

University of Strathclyde

May 2022

Declaration Statement

This thesis is the result of the author's original research. It has been composed by the author and has not been previously submitted for examination, which has led to the award of a degree.

Signed: ZH. J. WANG

Date: 10/05/2022

Abstract

Silk fibroin has robust mechanical properties with superior biocompatibility and biodegradability. Therefore, it has great potential as surgical sutures and scaffolds for cartilage reconstruction. In addition, silk fibroin particles (hereinafter referred to as silk particles) have shown significant capability as ideal drug carriers for anti-tumour and intra-articular agents. However, most manufacturing methods for silk particles are chemical-based or instrument-based, which requires chemical agents or costly instruments. Some mechanical manufacturing techniques, such as ball milling and bead milling, have been used to fabricate silk particles. However, the dimensional consistency of the fabricated silk particles is often poor, not to mention the low productivity of these techniques. More importantly, most manufacturing approaches can only make spherical silk particles and lack the ability to fabricate particles with helical or filamentous shapes and specified sizes that are believed to have better drug delivery efficacy. Therefore, this thesis aims to develop a new low-cost, chemical-free manufacturing process using diamond turning to obtain silk particles in the form of cutting chips whose geometries can be tailored by processing parameters.

The machinability of silk fibroin in diamond turning was first investigated through cutting experiments from the aspects of specific cutting force and chip morphology. The ductile mode cutting of silk fibroin was achieved. Moreover, long helical silk particles with a tunable radius of curvature were manufactured using a sharp point tool with a feed rate of less than 2.5 μm/rev. The feed rate can be used to customise the radius of curvature of helical particles. Long ribbon silk particles were also generated using a round nose tool. The folding wavelength of the ribbon particles can be tailored

by tuning the cutting speed and depth of cut. All experimental results demonstrated the feasibility of manufacturing geometry-controllable silk particles using diamond turning. A chip chart for diamond turning of silk fibroin was created, indicating that the breakability of silk chips increases at a reduced feed rate and depth of cut. This tendency is opposite to what is commonly observed on metallic materials due to the soft but highly tough property of silk fibroin. Although short and discontinuous folded particles were also manufactured, the dimensional consistency of the particles is extremely low, demonstrating the low chip-breaking efficiency when simply changing the processing parameters due to the ductility of silk fibroin.

The serrated chip formation mechanism in diamond turning of silk fibroin was then studied using hybrid finite element and smoothed particle hydrodynamics (FE-SPH) numerical simulations. The Cowper-Symonds material parameters for silk fibroin were preliminarily determined to be $p = 7$ and $D = 1140\ s^{-1}$. The specific cutting force obtained by this model was 49.0% smaller than the experimental value. Nevertheless, good prediction accuracy regarding chip morphology was achieved. The simulation results revealed that the shear band formation was ascribed to the conjunction of two parts of the plastic deformation localized at the cutting zone. Specifically, one part propagates from the cutting edge to the free surface, while the other part initiates on the free surface and propagates towards the cutting edge. The link between the serrated chip formation and the hierarchical structure of silk fibroin was also revealed with the aid of this hybrid FE-SPH model.

A high-frequency elliptical vibrator for diamond turning with tunable operational frequency and amplitude was developed as a chip breaker to obtain filamentous silk particles. The designed elliptical vibrator adopts a flexure-hinge structure that

combines the leaf spring flexure hinge (LSFH) and the notch hinge prismatic joint (NHPJ). This configuration can not only transmit and connect the reciprocating displacements of the diamond tool but also offer an improved operational frequency. The finite element analysis (FEA) results indicate that a decrease in the neck thickness of the NHPJ can reduce the cross-axis coupling ratio. Meanwhile, a reduction in the thickness of the LSFH can reduce the first natural frequency of this vibrator and change the sequence of its vibrational mode shapes.

A series of performance evaluation tests was conducted on a prototype of the designed elliptical vibrator. The test results show that this elliptical vibrator can achieve a high-frequency and non-resonant working mode with an acceptable cross-axis coupling ratio and thermal generation. Moreover, the elliptical tool trajectories with different amplitudes were generated by tuning the operational frequency, input voltage and phase angle. This elliptical vibrator can work at an operational frequency of up to 5 kHz. Its vibration amplitude can reach 2 μm. Preliminary diamond turning experiments were conducted on a copper workpiece to verify its chip-breaking effectiveness.

Finally, the manufacturing of filamentous silk particles was studied through elliptical vibration diamond turning experiments and hybrid FE-SPH numerical simulations. The influence of processing parameters such as horizontal speed ratio (HSR) and depth ratio on chip breakability was thoroughly studied in cutting experiments and simulations. It was found that a large HSR and a small depth ratio can help to achieve effective chip breaking and obtain filamentous silk particles due to the reduced average tool velocity angle θ_a. The simulation results show that a decrease in the average tool velocity angle can decrease the ductility of silk fibroin and

make the chip easy to break due to the reduced hydrostatic pressure and enhanced shearing action of the diamond tool. The critical average tool velocity angle θ_c was confirmed to be 22.6° for elliptical vibration diamond turning of silk fibroin. The average tool velocity angle should always be kept below this critical value to obtain filamentous silk particles.

Acknowledgement

The completion of this PhD study could not have been possible without the guidance and support of Prof Xichun Luo, my beloved supervisor. His immense knowledge and insight in this study steered me throughout my PhD research. I also want to extend my gratitude to my internal and external examiners. Thanks for helping strengthen this work.

I also want to acknowledge my secondary supervisor, Prof Yi Qin, for his support and encouragement. I would like to express my gratitude and appreciation for Prof Jining Sun, Dr Philipp Seib and Dr Suttinee Phuagkhaopong, who paved the way for my research on silk fibroin.

I am most grateful to my family for all the support they have given me in this long journey of more than four years, especially during the pandemic. Also, I would like to thank my girlfriend Qiaojia, my best friend and companion. Thank you for coming into my life and making it amazing. You have coloured my life with your love and laughter.

My sincere thanks will also go out to my friends and colleagues; Dr Wenlong Chang, Dr Quanren Zeng, Prof Yukui Cai, Dr Wenbin Zhong, Dr Fei Ding, Dr Yankang Tian, Dr Qi Liu, Dr Song Yang, Mr Beiya Yang, Mr Jian Gao, Mr Xiuyuan Chen, Mr Yonghang Jiang, Mr Charles Walker and all colleagues at the Centre for Precision Manufacturing. It's my great honour to meet and work with those wonderful people.

The list of who has helped me is quite long. Please forgive me that I cannot list them all considering the spacing limits, but thanks again for their help, patience and kindness.

In the end, I would like to gratefully acknowledge the financial support from EPSRC (EP/K018345/1, EP/T024844/1, EP/V055208/1), UK Royal Society- International Exchange Scheme (IEC/NSFC/181474) to this research and China Scholarship Council to sponsor stipend.

List of Publications

Journal papers

[1] **Wang Z**, Luo X, Sun J, Seib P, Phuagkhaopong S, Chang W, et al. Investigation of chip formation mechanism in ultra-precision diamond turning of silk fibroin film. J Manuf Process 2022;74:14–27.

[2] **Wang Z**, Luo X, Liu H, Ding F, Chang W, Yang L, et al. A high-frequency non-resonant elliptical vibration-assisted cutting device for diamond turning microstructured surfaces. Int J Adv Manuf Technol 2021;112:3247–61.

[3] Yang L, Luo X, Chang W, Tian Y, **Wang Z**, Gao J, et al. Manufacturing of anti-fogging super-hydrophilic microstructures on glass by nanosecond laser. J Manuf Process 2020;59:557–65.

[4] Ding F, Luo X, Chang W, **Wang Z**. In Situ Measurement of Spindle Radial and Tilt Error Motions by Complementary Multi-probe Method. Nanomanufacturing Metrol 2019;2:225–34.

Conference papers

[1] **Wang Z**, Cai Y, Luo X. Modelling and Simulation of Cutting Process by Smoothed Particle Hydrodynamics (SPH): A Review. 2019 25th Int. Conf. Autom. Comput., IEEE; 2019, p. 1–6.

Table of Contents

Nomenclature

α	Tool clearance angle
α_c	Shape coefficient of the chip cross-section
α_d	Constant depends on the dimensions
β	Material hardening parameter
ΔU_f	Rotational energy of each notch hinge
ΔU_y	Rotational energy of each NHPJ (cutting direction)
ΔU_z	Rotational energy of each NHPJ (depth of cut direction)
Δy	Maximum parasitic displacement (cutting direction)
Δz	Maximum parasitic displacement (depth of cut direction)
$\delta(\boldsymbol{x})$	Dirac delta function
δ_c	Constant related to the chip cross-section
$\dot{\varepsilon}^*$	Normalized strain rate (Johnson-Holmquist model)
$\dot{\varepsilon_p}^*$	Normalized effective plastic strain rate (Johnson-Cook model)
ε^P	Actual plastic strain (Johnson-Holmquist model)
ε_f^P	Plastic strain to fracture under actual pressure (Johnson-Holmquist model)
$\dot{\varepsilon}$	Actual strain rate (Johnson-Holmquist model)
$\dot{\varepsilon_0}$	Reference strain rate (Johnson-Cook model)(Johnson-Holmquist model)
$\dot{\varepsilon}_d$	Dynamic strain rate (Cowper-Symonds model)
$\dot{\varepsilon_p}$	Effective plastic strain rate (Johnson-Cook model)
ε_b	Chip tensile strain
ε_c	Actual chip strain

ε_d	Dynamic strain (Cowper-Symonds model)
ε_p	Effective plastic strain (Johnson-Cook model)
θ	Tool velocity angle
$\theta(t)$	Transient tool velocity angle
θ_a	Average tool velocity angle
θ_c	Critical average tool velocity angle
θ_{max}	Maximum tool velocity angle
θ_y	Angular displacements of hinges located along the cutting direction
θ_z	Angular displacements of hinges located along the depth of cut direction
κ	Constant that determines the effective area of the smoothing function
κ_γ	Cutting edge angle
λ_d	Wavelength of the machined microstructures
λ_f	Folding wavelength of the ribbon chips
ν	Poisson's ratio
π	Mathematical constant, 3.1415926
ρ	Density of the material
ρ_j	Density of particle j
Σ	Surface of the integral domain
σ^*	Normalized effective stress (Johnson-Holmquist model)
σ_f^*	Normalized fracture stress (Johnson-Holmquist model)
σ_i^*	Normalized intact equivalent stress (Johnson-Holmquist model)
σ	Actual effective stress (Johnson-Holmquist model)(Cowper-Symonds model)

σ_d	Dynamic yield stress (Cowper-Symonds model)
σ_{HEL}	Effective stress in HEL
σ_s	Static yield strength (Cowper-Symonds model)
σ_y	Yield stress (Johnson-Cook model) (Cowper-Symonds model)
φ	Phase angle between two input signals
Ω	Integral domain
A	Material parameter (Johnson-Cook model)(Johnson-Holmquist model)
A_c	Undeformed chip cross-section
a	Tool path dimension (cutting direction)
B	Material parameter (Johnson-Cook model)(Johnson-Holmquist model)
b	Tool path dimension (depth of cut direction)
b_1	Width of NHPJ
b_2	Width of LSFH
C	Material parameter (Johnson-Cook model)(Johnson-Holmquist model)
C_1	Cross-axis coupling ratio
C_2	Cross-axis coupling ratio
C_p	Capacitance of the piezo actuator
D	Material parameter (Cowper-Symonds model)
D_1	Material damage parameter (Johnson-Holmquist model)
D_2	Material damage parameter (Johnson-Holmquist model)
D_d	Material damage parameter (Johnson-Holmquist model)
D_{ins}	Instantaneous cutting diameter
D_y	Linear displacements of the hinges (located along the cutting direction)

D_z	Linear displacements of the hinges (located along the depth of cut direction)
d_c	Depth of cut
d_{cr}	Critical depth of cut
d_n	Nominal depth of cut
d_y	Maximum output displacements (cutting direction)
d_z	Maximum output displacements (depth of cut direction)
E	Young's modulus
E_p	Plastic hardening modulus
E_{TAN}	Tangent modulus
F_c	Measured cutting force
F_s	Specific cutting force
F_y	Actuation force (cutting direction)
F_z	Actuation force (depth of cut direction)
$f(\boldsymbol{x})$	An arbitrary field function of the position vector $\boldsymbol{x}$
$<f(\boldsymbol{x})>$	Kernel approximation of the function $f(\boldsymbol{x})$
f	Vibration frequency
f_{cr}	Critical feed rate
h	Smoothing length
h_d	Height of the machined microstructures
K	Proportion of the power consumption converted into heat
K_α	Rotary stiffness of NHPJ
K_d	Stiffness of LSFH
K_{eql}	Equivalent stiffness of the combination of LSFH and NHPJ

L	Distance between two notch hinges
L_1	Length of LSFH
l	Thickness of LSFH
l_c	Chip length
M	Total number of SPH particles
m	Material parameter (Johnson-Cook model)(Johnson-Holmquist model)
m_j	Mass of the particle j
N	Spindle speed
$\boldsymbol{n}$	Unit vector normal to the surface Σ
n	Material parameter (Johnson-Cook model)(Johnson-Holmquist model)
O	Geometric centre of the elliptical tool trajectory
P^*	Normalized pressure (Johnson-Holmquist model)
P_t^*	Normalized tensile hydrostatic pressure (Johnson-Holmquist model)
P	Actual pressure (Johnson-Holmquist model)
P_{HEL}	Actual pressure in HEL (Johnson-Holmquist model)
P_h	Heat generation power
P_t	Maximum tensile hydrostatic pressure (Johnson-Holmquist model)
p	Material parameter (Cowper-Symonds model)
p_1, p_2,...	Points marked in the chip
R	Chip radius of curvature
R_0	Initial chip up-curl radius
Ra	Surface roughness
R_c	Tool nose radius

R_L	Critical chip up-curl radius before getting tangled
R_n	Radius of NHPJ
R_s	Chip side-curl radius
R_u	Chip up-curl radius
r	Relative distance between two vectors
r_d	Depth ratio
r_e	Tool edge radius
r_{ij}	Distance between particle i and j
S	Shear band spacing
T^*	Normalized temperature (Johnson-Cook model)
T	Actual temperature (Johnson-Cook model)
T_0	Ambient temperature (Johnson-Cook model)
T_m	Material melting temperature (Johnson-Cook model)
t	Time
t_c	Chip thickness
t_m	Maximum chip thickness
t_n	Neck thickness of NHPJ
U	Peak-to-peak voltage
u	Upfeed per cycle of the workpiece
V_{cri}	Critical workpiece velocity
V_j	Volume of particle j
V_w	Nominal cutting speed
$\boldsymbol{v}$	Transient tool velocity vector

v_y, $v_y(t)$ y-component of the transient tool velocity vector

v_z, $v_z(t)$ z-component of the transient tool velocity vector

W Smoothing (kernel) function

W_{ij} Smoothing (kernel) function for particles

W_v Virtual work done by actuation forces

w_c Chip width

$\boldsymbol{x}$, $\boldsymbol{x}'$ Position vector

y, $y(t)$ Tool displacements in the cutting direction

y_1, y_2,... y-coordinate of point p_1, p_2,...

z, $z(t)$ Tool displacements in the cutting direction

z_1, z_2,... z-coordinate of point p_1, p_2,...

List of Abbreviations

1D	One-dimensional
2D	Two-dimensional
3D	Three-dimensional
B. mori	*Bombyx mori*
FE	Finite element
FEA	Finite element analysis
FEM	Finite element method
FE-SPH	Finite element and smoothed particle hydrodynamics
HEL	Hugoniot Elastic Limit
HSR	Horizontal speed ratio
H-bond	Hydrogen bond
LSFH	Leaf spring flexure hinge
MLS	Moving least squares
NHPJ	Notch hinge prismatic joint
ODE	Ordinary differential equation
PDE	Partial differential equation
SEM	Scanning electron microscope
SPH	Smoothed particle hydrodynamics

List of Tables

List of Figures

Chapter 1

Introduction

1.1 Research background

Cancer is one of the leading causes of death worldwide, accounting for almost 10 million deaths in 2020, or nearly one in six deaths, according to data from the World Health Organization [1]. The major reason for this high mortality rate lies in the difficulty of delivering therapeutic agents only to the tumour sites without damaging healthy tissues and organs [2]. After several decades of development, drug delivery systems based on engineered particles have shown great promise in solving this problem [3]. Among the numerous materials for manufacturing engineered particles, silk fibroin is renowned for its excellent mechanical properties, biocompatibility and biodegradability [4,5].

Silk fibroin is extracted from the *Bombyx mori* (*B. mori*) silkworm silk (see Figure 1.1) that mainly consists of two proteins: 70–80% fibroin and 20–30% sericin [6]. Not only for cancer treatments, silk particles (sized from tens of nanometres to hundreds of microns) have also shown significant potential as ideal carriers for intra-articular agents [7]. Compared with free drugs, drug-loaded silk particles can improve the blood residence time of drug molecules, thus dramatically increasing their pharmacokinetics and cellular uptake [8].

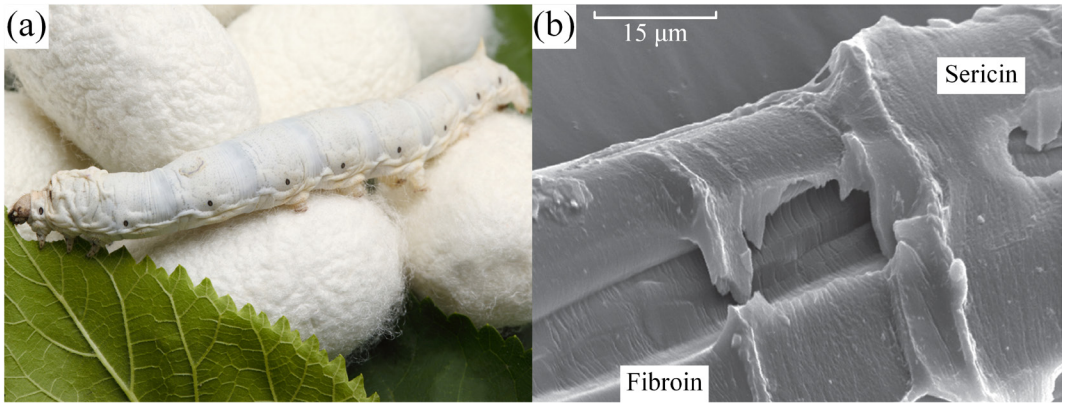

Figure 1.1 (a) *B. mori* silkworm and cocoons [9]; (b) silk filament that consists of fibroin and sericin [10].

Silk particles are generally made using chemical processing methods, such as desolvation [11] and salting out [12]. These production methods require chemical agents that result in contamination of the environment and the potential degradation of fibroin structures. Apart from chemical methods, instrument-based methods such as electrospraying [13] and laminar jet break-up [14] have been extensively investigated. However, these methods require expensive instruments and complicated operations [15]. In addition, several mechanical techniques have been adopted, such as ball milling [16] and bead milling [17]. But the productivity of these mechanical manufacturing approaches is low, and the dimensional consistency of the fabricated silk particles is often poor.

More importantly, most of the existing manufacturing approaches can only make spherical silk particles, as shown in Figure 1.2. However, particles with helical [18] or filamentous [19,20] shapes and specified sizes are believed to have better efficacy in terms of targeting and immune clearance for drug delivery than their spherical counterparts [21].

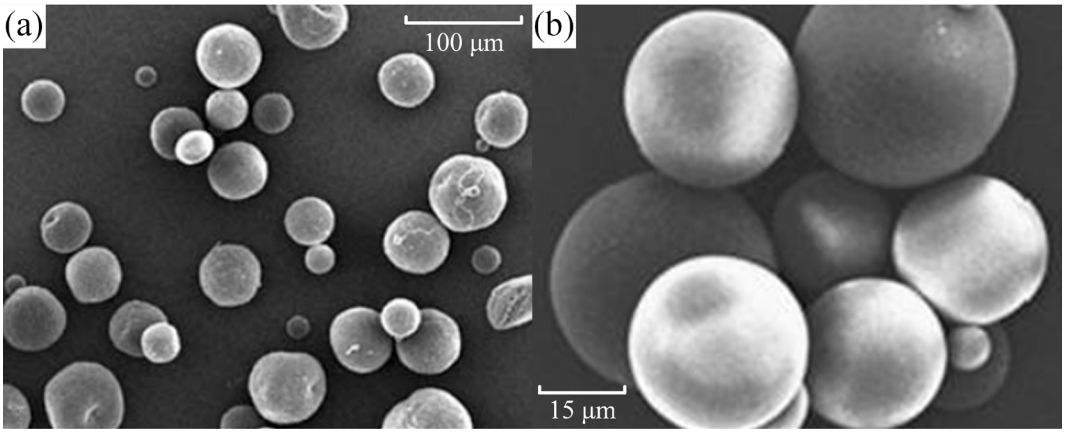

Figure 1.2 (a) Silk microspheres prepared by Imsombut et al. [22]; (b) silk microspheres prepared by Baimark et al. [23].

In contrast to the previously mentioned methods, diamond turning is a low-cost and chemical-free manufacturing approach in which different chip morphologies can be obtained through changing processing parameters [24–26]. Therefore, this thesis will investigate the feasibility of using diamond turning to manufacture silk particles (i.e. cutting chips) with controllable geometries.

To the best of the author's knowledge, diamond turning of silk fibroin has never been attempted before, in which the chip formation mechanism is, therefore, a knowledge gap. Silk fibroin has a hierarchical structure, and its beta-sheet crystallites are embedded in the amorphous matrix [27]. The crystallites and amorphous matrix have entirely different degrees of strength, stiffness and toughness, which will reduce the machinability of silk fibroin.

An understanding of how this hierarchical structure influences the chip morphology is pivotal to the success of process control to obtain silk particles with different geometries.

It is very difficult to reveal the cutting mechanism using only the experimental approach due to the restriction of in-situ experimental observation in diamond turning. Numerical simulation has been widely used as an effective alternative to investigate the underlying cutting mechanism, along with post-experimental cutting chip characterizations. It is well known that an accurate constitutive description of the non-linear dynamic behaviour of the machined material is essential for numerical simulations, which is usually in the form of a set of material parameters in analytical material models. However, there is no material model available that can fully describe the damage behaviour in diamond turning of silk fibroin. This presented one research challenge in the numerical simulation study that will be addressed in this research.

In order to manufacture filamentous silk particles, effective chip breaking is required in diamond turning of silk fibroin. However, the efficiencies of chip breaking through tuning processing parameters or using chip breakers are extremely low for ductile materials. One solution to address this issue is to use elliptical vibration diamond turning. But the use of a high-frequency non-resonant elliptical vibrator for diamond turning is still rare, limiting its possibilities for chip control to obtain filamentous silk particles. This is because of the unique tool/spindle configuration in diamond turning and the low structural stiffness of existing vibrators. Moreover, significant problems, such as the cross-axis coupling and the overheating of piezo actuators, are usually encountered, which proposes serious design challenges for a high-frequency non-resonant elliptical vibrator.

In addition, elliptical vibration diamond turning of silk fibroin has never been conducted. A clear understanding of how the processing parameters affect chip

breakability presents another knowledge gap, which will be thoroughly studied in this thesis.

1.2 Aim and objectives

This thesis aims to establish a new manufacturing approach to obtain silk particles with different geometries using diamond turning. The principal objectives are as follows:

(1) To evaluate the machinability of silk fibroin in diamond turning and to provide the recommended processing parameters for manufacturing silk particles with different geometries.

(2) To reveal the chip formation mechanism in diamond turning of silk fibroin through cutting experiments and numerical simulations and to determine the influence of the hierarchical structure of silk fibroin on chip formation.

(3) To develop a high-frequency non-resonant elliptical vibrator that can effectively improve the chip-breaking efficiency.

(4) To achieve an in-depth understanding of how the processing parameters in elliptical vibration diamond turning affect chip breakability of silk fibroin and to present the optimal processing parameters for manufacturing filamentous silk particles.

1.3 Thesis structure

The thesis is divided into eight chapters. The logical information flow is illustrated in Figure 1.3.

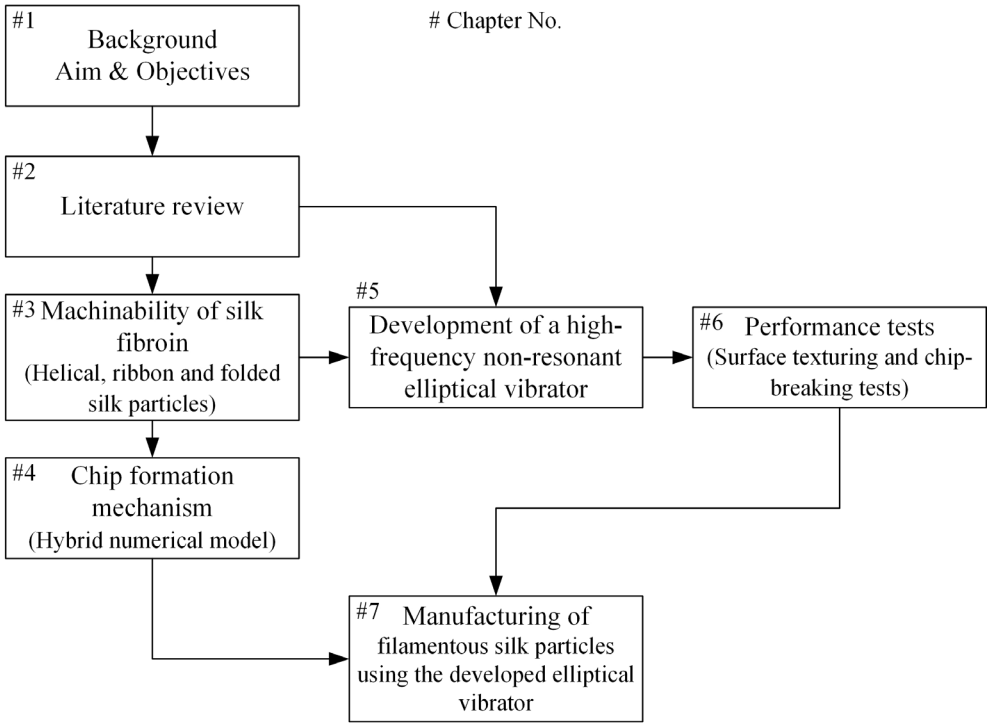

Figure 1.3 Flowchart of the thesis structure.

Chapter 1 explains the background, aim and objectives. The thesis structure is also illustrated.

Chapter 2 reviews the chip morphology and chip breaking methods in diamond turning, as well as the modelling and simulation of micro-cutting using SPH technique. Thus, the research challenges and knowledge gaps can be identified.

Chapter 3 evaluates the machinability of silk fibroin in diamond turning with regard to cutting force and chip morphology. Thus, the recommended processing parameters for generating silk particles with different geometries are provided. The limitations of controlling chip geometry by simply changing processing parameters in diamond turning will also be discussed, which motivates the design of an elliptical vibrator for chip breaking in Chapter 5.

Chapter 4 establishes a hybrid numerical model to investigate the chip formation

mechanism in diamond turning of silk fibroin, together with a determination of its material parameters. The link between the chip formation mechanism and the hierarchical structure of silk fibroin will also be revealed.

Chapter 5 concerns the development of a flexure-based non-resonant elliptical vibrator for diamond turning to achieve the goal of high operational frequency.

Chapter 6 presents the experimental performance tests for the proposed elliptical vibrator. Preliminary chip-breaking tests will be performed.

Chapter 7 reveals how the processing parameters in elliptical vibration diamond turning affect the chip breakability of silk fibroin by means of numerical simulations and experiments. The optimal processing parameters for manufacturing filamentous silk particles are recommended.

Chapter 8 summarises the conclusions of this thesis and its contributions to knowledge. Study limitations and future research recommendations are also provided.

Chapter 2

Literature review

2.1 Introduction

This chapter first reviews the influence of the geometries of silk particles in drug delivery. After that, typical manufacturing methods of silk particles are summarised. Then, the chip morphology and chip breaking methods in diamond turning are reviewed. Previous attempts to study micro-cutting using SPH technique are presented. Finally, the research challenges and knowledge gaps are identified.

2.2 Influence of geometries of silk particles in drug delivery

Silk particles have a high potential in drug delivery, whose geometries can be modified accordingly based on the applications (see Figure 2.1).

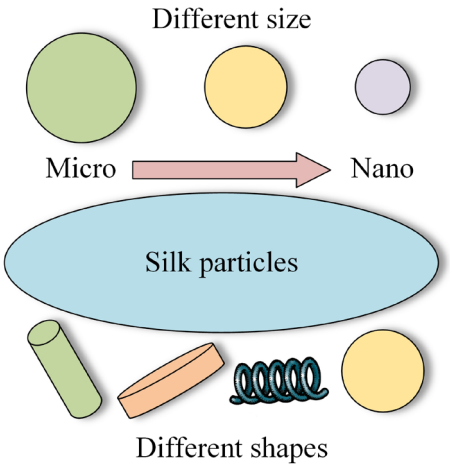

Figure 2.1 Geometries of silk particles.

Most silk particles for drug carriers are spherical as this shape is easy to manufacture. However, the sphere is not always the best geometry for drug delivery; indeed, shape

is emerging as a key factor dictating circulation time, biodistribution, cellular uptake and intracellular trafficking [28]. The shape evolution of viruses and bacteria endows them with exquisite capabilities to deliver their cargo and evade the immune system. For example, inspired by the helical structure of tobacco mosaic virus that can escape degradation, helical particles are expected to have a critical influence on next-generation medicines [18,29]. The possible shape effects of natural filoviruses were also investigated [19]. Geng et al. [30] found that filamentous particles remained in the blood circulation for up to one week after injection, which is almost ten times longer than their spherical counterparts. The obtained filomicelles delivered paclitaxel and effectively shrank the human-derived tumours in mice. Petros and DeSimone [31] pointed out that filamentous particles with dimensions of up to 18 μm were reported to exhibit considerably longer circulation half-lives than even stealth liposomes. Instead, the rigid spheroids were almost immediately cleared from the circulation.

The size of silk particles also has important effects on drug delivery. During medicine formation, the smaller the particles, the higher proportion of the drug that will have access to the aqueous phase, which leads to substantial loss of payload and lower drug loading. In general, microparticles are unlikely to cross most biological barriers, which must be delivered directly to the tissue of interest. For instance, silk microparticles with diameters of 1–21.6 μm were fabricated as carriers for intra-articular drug delivery, which increased the sustained residence time in the joint space [32]. On the contrary, nanoparticles can cross biological barriers due to their smaller size, although smaller particles are more likely to aggregate. Overall, what size is optimal and what barriers can be crossed is often a matter of your targets [33]. Size also has a significant impact on drug retention time in tissues. Kohane et al. [34] argued

that microparticles remained where they were injected, whereas nanoparticles with the same material and mass were already eliminated in the same time frame.

In summary, the shape and size of silk particles are two important parameters that will greatly influence the performance of a drug delivery system. Therefore, research and development of novel manufacturing approaches that are capable of accurately tuning the geometry of particles are of great importance for the development of next-generation medicines.

2.3 Manufacturing techniques for silk particles

So far, numerous methods have been developed for manufacturing silk particles. All the methods can be divided into two categories: the top-down and the bottom-up, which are summarised in Table 2.1.

Table 2.1 Manufacturing techniques for silk particles.

Categories	Techniques	Comments	Particle dimensio
Top-down	Ball milling [16]	Cheap equipment; easy operation; low dimensional consistency; particle aggregation.	0.2-4 μm
Top-down	Bead milling [17]	Easy operation; time-consuming.	0.3-7 μm
Bottom-up	Electrospraying [13]	Tunable particle size; high dimensional consistency; costly equipment.	59-75 nm
Bottom-up	Laminar jet break-up [14]	No organic solvent; large particle dimension; costly equipment.	100-440 μm
Bottom-up	Desolvation [11]	Easy operation; chemical residues.	300 nm
Bottom-up	Salting out [12]	Easy to scale up; chemical residues.	0.5-2 μm

In general, mechanical processes (e.g. ball milling [16] and bead milling [17]) are required in the top-down method to downsize the raw materials, such as silk fibroin fibre and regenerated silk fibroin, to become silk particles. However, the productivity of these mechanical manufacturing approaches is low, and the dimensional consistency of the fabricated silk particles is often poor. More importantly, it is not easy to precisely control the geometry of silk particles.

The bottom-up methods can be classified into two categories: instrument-based and chemical-based. They both have advantages in controlling particle size. However, the former group often relies on expensive instruments and expertise. As for chemical-based methods, chemical agents are usually required, which may potentially degrade the fibroin structures and contaminate the environment.

Overall, most available manufacturing techniques can only produce spherical silk particles. A low-cost and chemical-free manufacturing method for silk particles with tunable geometry is rare and urgently needed. Diamond turning can potentially provide an alternative solution to obtain geometry-controlled silk particles in the form of cutting chips through tuning processing parameters.

2.4 Chip morphology and chip breaking in diamond turning

2.4.1 Mechanics of chip breaking

Chip formation initiates from the curling of the cutting chips, which is then dramatically affected by a number of processing parameters such as cutting speed, feed rate and depth of cut. Bradley Jared and Thomas Dow indicated that chip morphology could be characterized using two parameters, namely chip flow angle and chip radius

of curvature [35,36], which can be applied to characterize the chip breaking in diamond turning [37].

Currently, two primary approaches are applied to investigate the underlying mechanism of chip breaking. The first category focuses on the development of a database based on the machining trials on chip breaking [38,39], which is time and money consuming. On the other hand, the chip breaking can also be investigated by material stress analysis which is mainly based on the numerical simulation analysis and chip curvature analysis. FEA is the most commonly used numerical simulation method to describe mechanics in chip breaking [40]. Still, it is not the optimal solution to model material fracture and crack formation in chip breakage due to its mesh-based nature.

In chip curvature analysis, the relationship between chip radius of curvature and chip breaking is usually described by using Nakayama's [41] and Li's [42] chip-breaking criteria theoretically, which will be considered in more detail as follows:

- *Nakayama's chip-breaking criterion*

In Nakayama's theory, chip strain ε_c is proportional to the ratio of chip thickness t_c and chip up-curl radius R_u:

$$\varepsilon_c \propto \frac{t_c}{R_u} \tag{2-1}$$

Generally, the chip starts to form with an up-curl radius R_0. As the chip is continuously formed, the chip radius is increased correspondingly. The chip usually breaks when the actual chip strain ε_c is larger than chip tensile strain ε_b. A preferred chip breaking should happen before the chip gets tangled to protect the machined

surface from scratching. At this moment, the chip radius of curvature reaches its critical value R_L. Therefore, the actual chip strain ε_c can be derived as:

$$\varepsilon_c = \alpha_c t_c \left(\frac{1}{R_0} - \frac{1}{R_L}\right) \tag{2-2}$$

where α_c is the shape coefficient of the chip cross-section.

- *Li's chip-breaking criterion*

In general, most metallic materials satisfy the theory of chip-breaking limits. The chip will always break when the feed rate and depth of cut are higher than its critical value. On the basis of this, Li proposed a semi-empirical chip-breaking criterion. The critical feed rate f_{cr} is given below:

$$f_{cr} = \frac{\varepsilon_c}{\alpha_c \left(\frac{1}{R_0} - \frac{1}{R_L}\right) \frac{\sin \kappa_\gamma \cdot t_c}{d_c}} \tag{2-3}$$

where κ_γ is the cutting edge angle, and d_c is the depth of cut.

Likewise, the critical depth of cut d_{cr} can be defined as follows:

$$d_{cr} = \begin{cases} \dfrac{\varepsilon_b R_s \cos \delta_c}{\alpha_c} - \left(\dfrac{\pi}{2} - 1\right) R_c; \ (d_c \geq R_c) \\ \cos\left(\dfrac{57.3 \varepsilon_b R_s \cos \delta_c}{\alpha_c R_c}\right) - R_c; \ (d_c < R_c) \end{cases} \tag{2-4}$$

where R_s is the radius of curvature of side-curl chips. δ_c is a constant related to chip cross-section. R_c is the tool nose radius.

In short, it can be inferred that chip breaking can be achieved through changing processing parameters. However, it is difficult to realise the effective chip breaking on ductile materials by only adjusting processing parameters. Thus, chip breaking method is required to produce filamentous silk particles in the form of discontinuous chips.

2.4.2 Chip breaking method in diamond turning

Besides the use of changing processing parameters [35,36], a broad type of strategies can be applied to precisely control the geometry of cutting chips, such as using chip breakers [43,44], tool vibrations [45–47] and coolants (e.g. gas or fluid jets) [39,48]. However, for ductile material, the chip breaker cannot generate discontinuous chips in high efficiency [37]. The introduction of coolants brings difficulty in collecting the chips as fluid jets will blow chips away, not to mention their environmental contamination. Hence, this thesis will investigate the feasibility of using elliptical vibration diamond turning to achieve effective chip breaking.

2.5 Existing designs for elliptical vibrators

Generally, elliptical vibrators can be classified into two types based on the operational frequency mode: resonant mode and non-resonant mode. Resonant elliptical vibrators can obtain ultrasonic operational frequency [49,50] and large vibration amplitude over tens of micrometres [51] due to the high energy efficiency of the resonant mode. Figure 2.2 illustrates two typical designs of resonant elliptical vibrators.

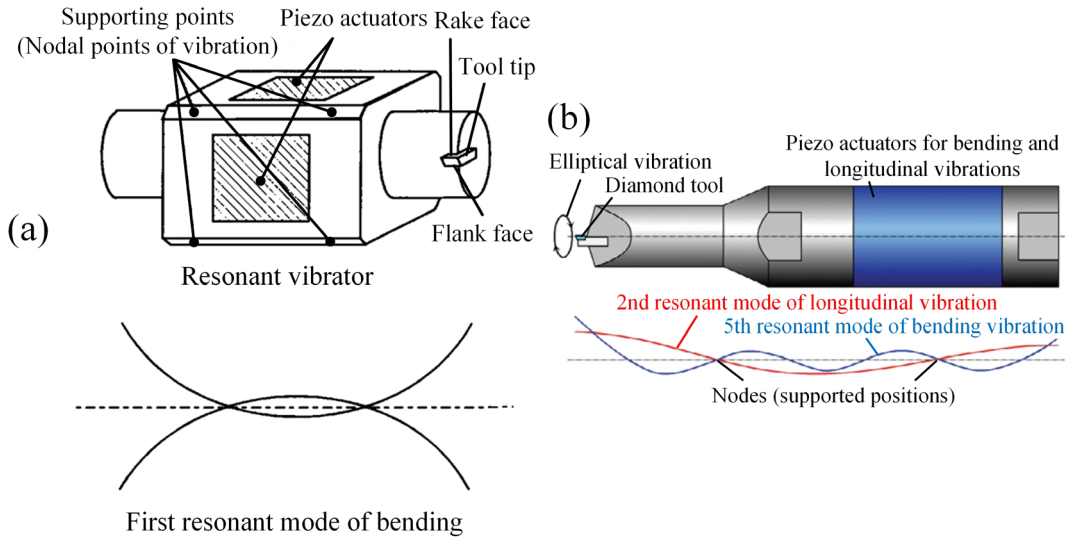

Figure 2.2 Resonant elliptical vibrators proposed by: (a) Moriwaki and Shamoto [52]; (b) Suzuki [53].

However, resonant elliptical vibrators can only work under a fixed frequency (i.e. resonant frequency) and vibration amplitude. They lack the ability to effectively tailor the size of the discontinuous chips [54,55].

In contrast, both the operational frequency and vibration amplitude of non-resonant elliptical vibrators could be adjusted [45]. Thus, they emerged to overcome the problems of resonant vibrators. For non-resonant vibrators, vibrations are generally applied directly [56] or through flexure hinges [57]. Figure 2.3 shows the configurations of several existing non-resonant elliptical vibrators.

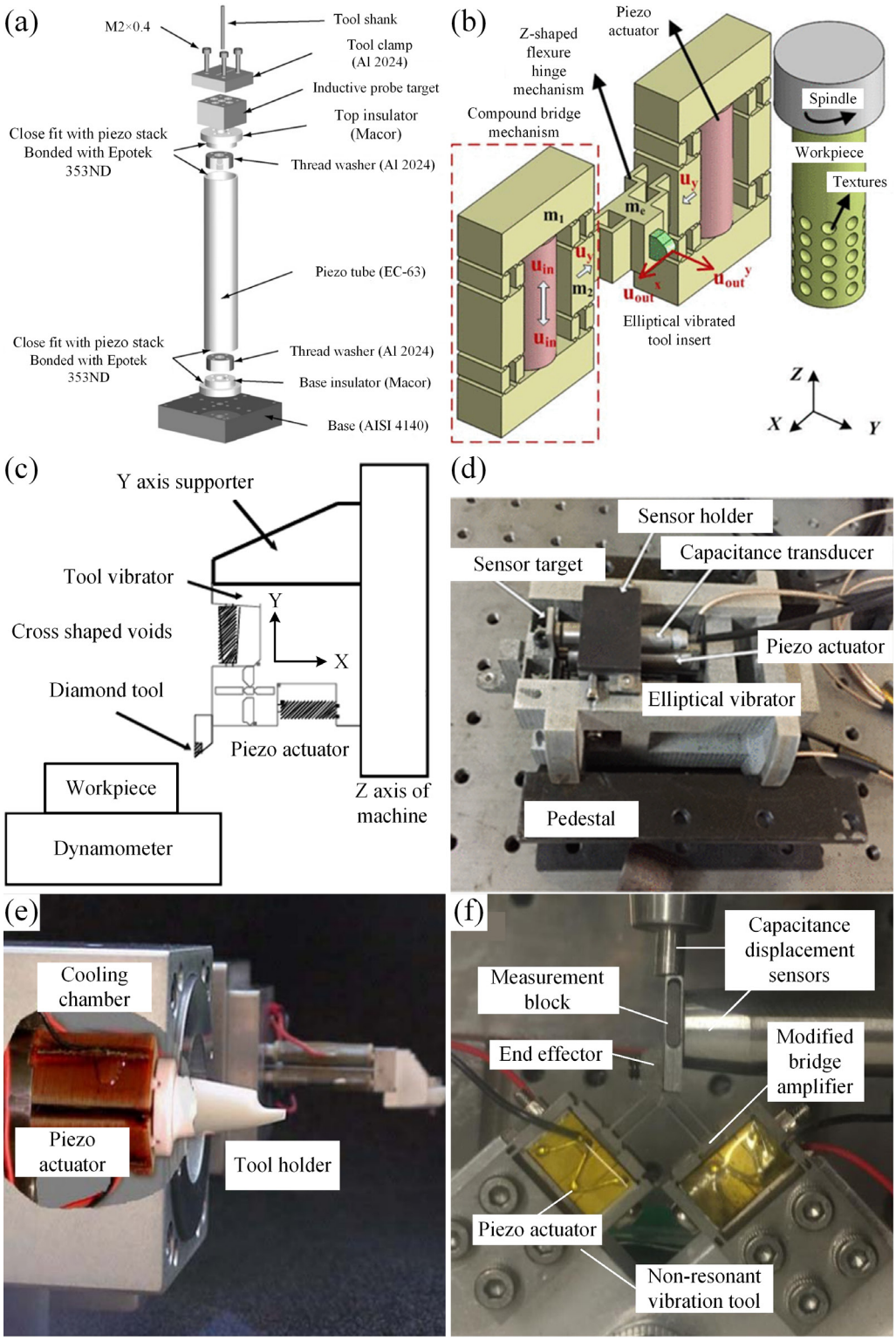

Figure 2.3 Non-resonant elliptical vibrators proposed by: (a) Heamawatanachai and Bamberg [58]; (b) Zhu et al. [59,60]; (c) Ahn et al. [61]; (d) Han et al. [62]; (e) Negishi and Dow [46]; (f) Wang et al. [63].

Heamawatanachai and Bamberg [58] developed a micro-cutting vibrator driven by a piezo tube. Although it can generate elliptical tool trajectories with an amplitude of up to 10 μm, its operational frequency can only reach 300 Hz. Zhu et al. [59,60] developed an elliptical vibrator with a novel Z-shaped flexure hinge. This high-stiffness configuration enables it to achieve an operational frequency of up to 500 Hz. Ahn et al. [61] proposed a flexure-based non-resonant elliptical vibrator, which can be operated at a frequency of 1 kHz. Han et al. [62] proposed a flexure-based vibrator for diamond turning. The frequency sweep test revealed that this vibrator could obtain the first natural frequency of up to 1.8 kHz. Negishi and Dow [46] developed a non-resonant elliptical vibrator with which a high-frequency working mode at 4 kHz could only be achieved with an additional cooling system, indicating the vital importance of the thermal control of the high-frequency non-resonant elliptical vibrator. They also developed another kind of non-resonant elliptical vibrator without the cooling system, but it could only work at up to 400 Hz [64]. A non-resonant vibration cutting tool was recently developed by Wang et al. [63] for surface texturing that claimed a working bandwidth of up to 6 kHz based on the results of the frequency sweep test. Nevertheless, it was specially designed for a three-linear-axis machine setup that is incapable of diamond turning.

In summary, high-frequency (i.e. over 4 kHz) non-resonant elliptical vibrators for diamond turning are still rare. This is not only due to the tool and spindle configuration for diamond turning but also the low structural stiffness of existing vibrators, especially in the direction perpendicular to the tool trajectory plane. High-frequency vibration can easily trigger the twisting motion of the diamond tool in this direction, which severely distorts the tool's trajectory. In addition, high-frequency input signals

require high power input for piezo actuators, leading to an increased heat generation. However, the overheating of piezo actuators will worsen the machining performance of the non-resonant elliptical vibrator and even cause a system failure. Thus, it is another critical problem that must be overcome.

The existing non-resonant elliptical vibrators can only reach relatively low operational frequency, which results in low machining efficiencies and hinders their industrial applications. Moreover, in diamond turning, as the excessive cross-axis coupling between two reciprocating displacements of the cutting tool can distort the elliptical tool trajectory, it must be strictly limited, as excessive coupling will distort the elliptical tool trajectory. Therefore, the dimensional parameters of a non-resonant elliptical vibrator must be reasonably determined to strike a delicate balance between operational frequency, vibration amplitude, coupling effect and heat generation. Overall, the development of a high-frequency non-resonant elliptical vibrator for diamond turning with an acceptable coupling ratio and heat generation is a complicated and challenging task, which will be one of the research focuses of this thesis.

2.6 Control of chip geometry using elliptical tool vibration

Figure 2.4 illustrates the schematic of elliptical vibration diamond turning.

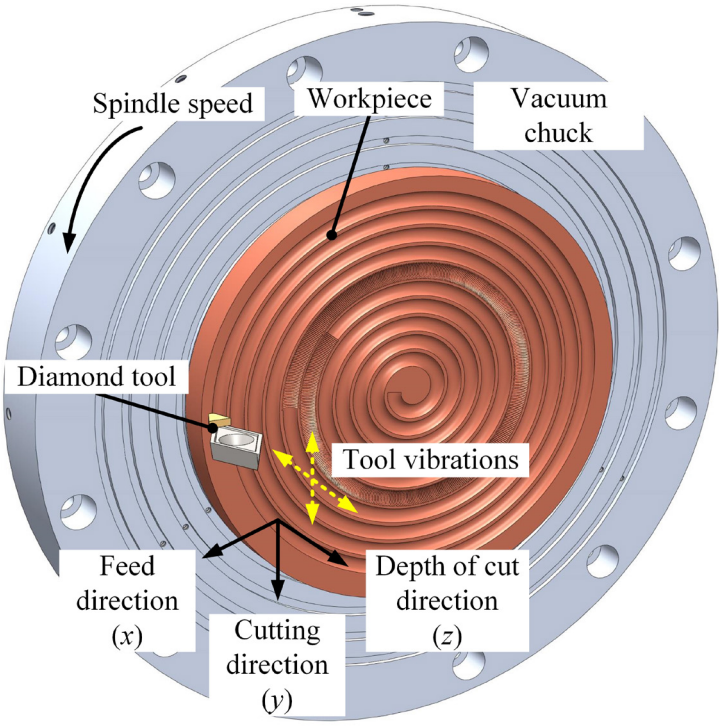

Figure 2.4 Schematic of elliptical vibration diamond turning.

As a 2D machining technique, the tool trajectory generated by the elliptical vibrator can be split into two displacements in the cutting and depth of cut directions, which can be described as:

$$\begin{bmatrix} y(t) \\ z(t) \end{bmatrix} = \begin{bmatrix} asin(2\pi ft) \\ bsin(2\pi ft + \varphi) \end{bmatrix} + \begin{bmatrix} V_w t \\ 0 \end{bmatrix} \tag{2-5}$$

where $y(t)$ and $z(t)$ are tool displacements in the y- (cutting) and z- (depth of cut) directions, respectively. a and b are tool path dimensions in the corresponding direction. Therefore, the tool vibration amplitudes (peak-to-peak) in the cutting and depth of cut direction are equal to $2a$ and $2b$, respectively. f is the vibration frequency. φ is the phase angle between two tool displacements. V_w is the nominal cutting speed of the workpiece that equals $\pi D_{ins} N$. D_{ins} is the instantaneous cutting diameter, and N is the spindle speed.

A parameter, HSR, can be used to characterize the elliptical vibration diamond turning process. It is defined as the ratio of V_w over the critical workpiece velocity V_{cri}:

$$HSR = \frac{V_w}{V_{cri}} = \frac{V_w}{2\pi f a} \tag{2-6}$$

The tool trajectories between two successive vibration cycles will overlap when V_w is smaller than V_{cri} (HSR < 1). In this case, the diamond tool and workpiece will contact intermittently, and thus the interrupted cutting can be achieved.

Figure 2.5 shows the chip formation principle in overlapping elliptical vibration diamond turning. The tool cutting path can be simplified as a series of overlapping ellipses, each one of which approximately represents a vibration cycle [45]. The function of upfeed per cycle u is shown in the following equation:

$$u = \frac{V_w}{f} \tag{2-7}$$

The nominal depth of cut d_n is the vertical distance between the workpiece surface and the deepest point that the diamond tool can reach. Depth ratio r_d is the ratio of the nominal depth of cut d_n and the tool path dimension b:

$$r_d = \frac{d_n}{b} \tag{2-8}$$

It can be expected that the discontinuous chips can be generated when d_n is less than the vertical dimension b (r_d < 1). In order to accomplish the geometry control over the silk chips, the discontinuous chip is of interest in this work.

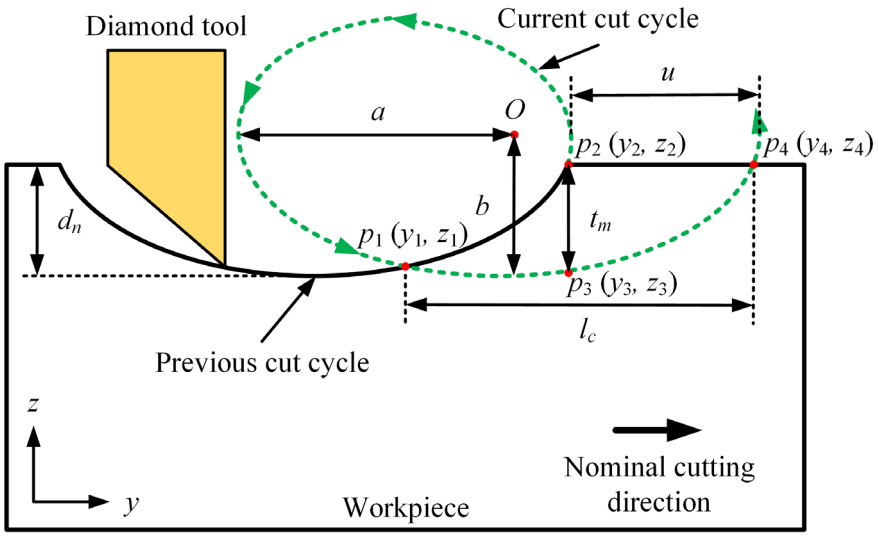

Figure 2.5 Chip formation principle in overlapping elliptical vibration diamond turning.

Point *O* is the geometric centre of the elliptical tool trajectory. The ellipse function of the current cut cycle is shown below:

$$\frac{y^2}{a^2}+\frac{z^2}{b^2}=1 \tag{2-9}$$

The equation for the previous cut cycle can be derived from Equation 2-9 with an offset u in y-axis:

$$\frac{(y+u)^2}{a^2}+\frac{z^2}{b^2}=1 \tag{2-10}$$

From the geometry relationship illustrated in Figure 2.5, the chip length l_c and maximum chip thickness t_m can be expressed below:

$$l_c=|y_4|+\frac{u}{2} \tag{2-11}$$

$$t_m=|z_3|-|z_2| \tag{2-12}$$

Points p_2 and p_4 align in the same horizontal line, whereas p_2 and p_3 align in the same vertical line. Thus:

$$|z_2| = |z_4| = b - d_n \tag{2-13}$$

$$|y_2| = |y_3| = a\sqrt{1 - \frac{(b - d_n)^2}{b^2}} \tag{2-14}$$

The expressions for chip length l_c and maximum chip thickness t_m can be converted into the following format:

$$l_c = a\sqrt{1 - \frac{(b - d_n)^2}{b^2}} + \frac{1}{2}u \tag{2-15}$$

$$t_m = \sqrt{(b - d_n)^2 + \frac{2ub^2\sqrt{1 - \frac{(b - d_n)^2}{b^2}}}{a} - \frac{u^2b^2}{a^2}} - (b - d_n) \tag{2-16}$$

In contrast, when V_w is greater than V_{cri} (HSR > 1), the tool trajectory will not overlap, as shown in Figure 2.6. However, intermittent cutting can still be achieved if the nominal depth of cut d_n is less than $2b$. Under this circumstance, the maximum chip length can reach the same value as upfeed per cycle u, and the maximum chip thickness can reach up to $2b$.

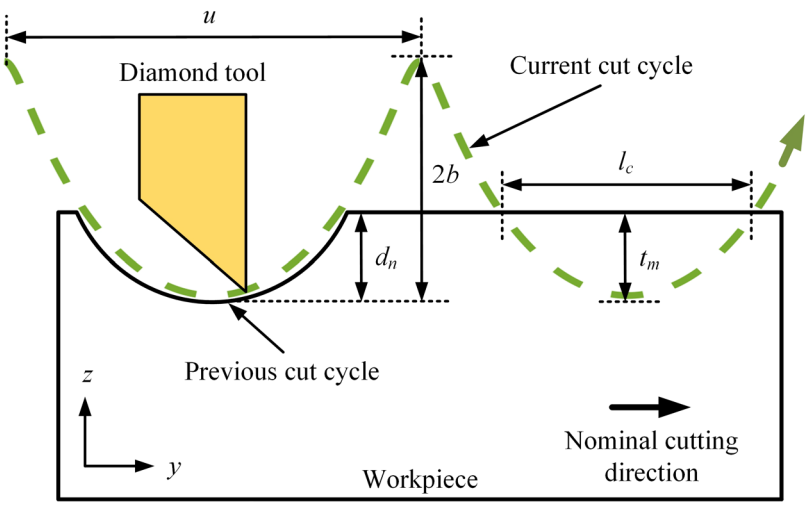

Figure 2.6 Chip formation principle in non-overlapping elliptical vibration diamond turning.

In summary, the chip length l_c and the maximum chip thickness t_m are deeply influenced by tool path dimensions a, b and vibration frequency f, which can be used to customise the chip geometry.

2.7 Numerical modelling of material fracture

Chip breakage often initiates with the material fracture on the free surface of the cutting chips [65]. Therefore, the chip formation and chip-breaking processes generally indicate the fracture and failure characteristics of the machined material [66]. Numerical modelling methods have been proven as a significant tool in understanding the material fracture process. Most of them can be divided into two subsections, i.e. mesh-based and meshless. The mesh-based methods for reproducing the initiation and propagation of cracks mainly consist of two types: 'Inter-Element Separation Model' and 'Arbitrary Crack-Path Model' [67]. In the former one, the cracks initiate and propagate along FE boundaries. This technique is simple and easy to manipulate but

with low computational accuracy, as the crack paths do not always coincide with element edges under practical conditions. Moreover, the ultra-fine mesh is usually required.

In order to overcome the shortcoming of 'Inter-Element Separation Models', 'Arbitrary Crack-Path Models', remeshing and eXtended finite element method (FEM) were proposed. However, the computing cost of remeshing is extremely high, as the amount of remeshing required can be enormous in the case of dynamic crack growth. eXtended FEM enables the cracks to pass through elements arbitrarily by introducing local enrichment equations to the stress and strain fields, so remeshing is not required during its evolution. However, a separate surface model is needed to track the crack location and identify the nodes that require enrichment. But this process is complex and costly.

The meshless method, such as SPH, does not require a fixed mesh grid to connect discrete nodes and therefore gets rid of mesh entanglement issues when workpiece material undergoes large deformations. Furthermore, meshless methods also reproduce a more arbitrary and realistic crack path as no mesh lines, and thus pre-defined directions are required for a crack to follow. The fracture algorithm used in SPH formulation is straightforward; the particles are no longer connected when the inter-particle distance becomes larger than the smoothing length. Hence, the SPH scheme will be used to model and predict the chip formation and chip-breaking processes in diamond turning of silk fibroin.

2.8 Modelling and simulation of micro-cutting using SPH

2.8.1 Theories of SPH formulation

The conventional SPH formulation was initially proposed to solve astrophysics problems. It has been widely used to investigate the underlying mechanism in various fields of science and technology [68], such as the micro-cutting process. In most circumstances, the dynamic problems governed by the partial differential equations (PDEs) are quite difficult to be solved analytically. Many efforts have been taken to get numerical solutions for PDEs. The problem domain of the PDEs is first discretized. Next, SPH formulation is introduced to achieve an approximation for the values of the field functions and their derivatives at any point in the problem domain. The PDEs are then rewritten into ordinary differential equations (ODEs) in a discretized form with time as the independent variable. This set of ODEs can then be solved following a standard integration routine.

The SPH formulation can be applied to achieve the tasks mentioned above, which mainly consists of two key steps: kernel approximation of the field functions and their particle approximation.

In the first step, the kernel approximation is a manipulation of the integral representation. The definition of the integral representation of the field function is shown below:

$$f(\boldsymbol{x}) = \int_{\Omega} f(\boldsymbol{x}')\,\delta(\boldsymbol{x}-\boldsymbol{x}')\,d\boldsymbol{x}' \tag{2-17}$$

where $f(\boldsymbol{x})$ is an arbitrary field function of the position vector $\boldsymbol{x}$. Ω is the integral domain where vector $\boldsymbol{x}$ is located.

$\delta(\boldsymbol{x})$ is a Dirac delta function:

$$\delta(\boldsymbol{x}-\boldsymbol{x}') = \begin{cases} 1; & (\boldsymbol{x}=\boldsymbol{x}') \\ 0; & (\boldsymbol{x}\neq\boldsymbol{x}') \end{cases} \tag{2-18}$$

Equation 2-17 reveals that a field function can be written into an integral form. In addition, the integral representation for $f(\boldsymbol{x})$ is exact as long as $f(\boldsymbol{x})$ is continuous in integral domain Ω.

Then, if a smoothing function (sometimes called kernel function) W is employed to replace the Dirac delta function. Equation 2-17 can be transformed into the following format:

$$f(\boldsymbol{x}) = \int_{\Omega} f(\boldsymbol{x}')\, W(\boldsymbol{x} - \boldsymbol{x}', h)\, d\boldsymbol{x}' \tag{2-19}$$

where h is the smoothing length which determines the effective area of the smoothing function W. The interaction between the central particle and its neighbours will be ignored outside the effective area.

However, as the smoothing function W is employed to approximate the Dirac delta function, the integral representation in Equation 2-19 can only be an approximation instead of an exact value. That is why this manipulation is called kernel approximation.

In this regard, Equation 2-19 should be revised as follows:

$$< f(\boldsymbol{x}) >= \int_{\Omega} f(\boldsymbol{x}')\, W(\boldsymbol{x} - \boldsymbol{x}', h)\, d\boldsymbol{x}' \tag{2-20}$$

where $<f(\boldsymbol{x})>$ denotes the kernel approximation of $f(\boldsymbol{x})$.

It should be noted that a smoothing function must satisfy several conditions. The first one is given below:

$$\int_{\Omega} W(\boldsymbol{x} - \boldsymbol{x}', h)\, d\boldsymbol{x}' = 1 \tag{2-21}$$

The above equation refers to the *normalization* condition.

The second condition is named *Delta function property*:

$$\lim_{h\to 0} W(\boldsymbol{x}-\boldsymbol{x}',h)=\delta(\boldsymbol{x}-\boldsymbol{x}') \tag{2-22}$$

Equation 2-22 shows that when the smoothing length h approaches 0, the smoothing function can be regarded as a Dirac delta function.

The third one is the *compact* condition, which is given below:

$$W(\boldsymbol{x}-\boldsymbol{x}',h)=0;\ when\ |\boldsymbol{x}-\boldsymbol{x}'|>\kappa h \tag{2-23}$$

Constant κ determines the effective area around $\boldsymbol{x}$. The mathematical term for the effective area is support domain, whose radius is usually κh. The value of constant κ varies from problem to problem.

For example, the smoothing function proposed by Monaghan and Lattanzio [69] based on the cubic spline function is given in Figure 2.7.

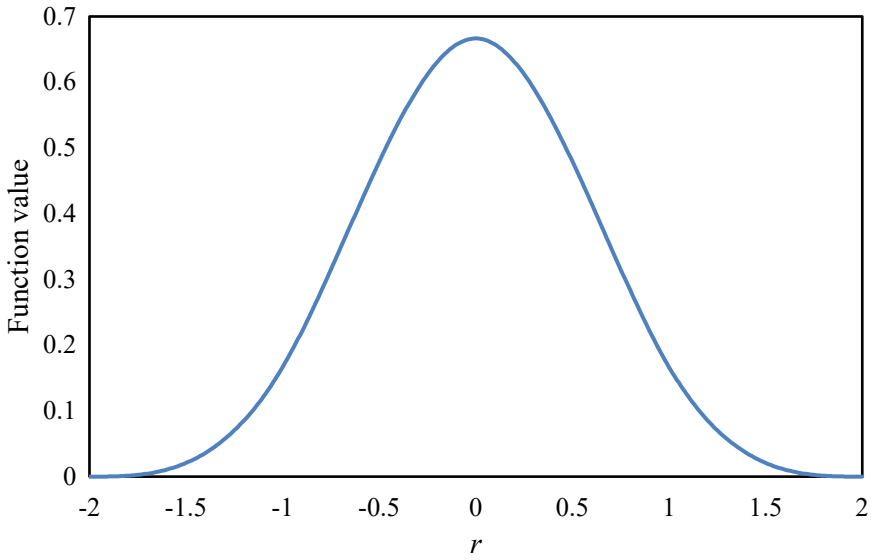

Figure 2.7 Cubic spline smoothing function.

As shown in Figure 2.7, a new variable r is introduced to simplify the expression of the smoothing function, and it denotes the relative distance between two vectors:

$$r=\frac{|\boldsymbol{x}-\boldsymbol{x}'|}{h} \tag{2-24}$$

Therefore, the expression for the smoothing function W can be rewritten into:

$$W(\boldsymbol{x}-\boldsymbol{x}',h)=W(r,h)=\alpha_d\times\begin{cases}\frac{2}{3}-r^2+\frac{1}{2}r^3;\ (0\le r<1)\\ \frac{1}{6}(2-r)^3;\ (1\le r<2)\\ 0;\ (r\ge 2)\end{cases} \tag{2-25}$$

α_d is a normalization constant that depends on dimensions, which gives:

$$\alpha_d=\begin{cases}\frac{1}{h};\ (1\mathrm{D})\\ \frac{15}{7}\pi h^2;\ (2\mathrm{D})\\ \frac{3}{2}\pi h^3;\ (3\mathrm{D})\end{cases} \tag{2-26}$$

Figure 2.7 shows that an increase in the relative distance between two position vectors will monotonically decrease the value of the smoothing function. Besides, a smoothing function must be smooth and even, also called the *even function* condition. Therefore, any function that satisfies the above-mentioned conditions can be chosen as a smoothing function.

Then, the integral representation for the derivative of the field function can be obtained by substituting $f(\boldsymbol{x})$ in Equation 2-20 with $\nabla\cdot f(\boldsymbol{x})$:

$$<\nabla\cdot f(\boldsymbol{x})>=\int_{\Omega}[\nabla\cdot f(\boldsymbol{x}')]\,W(\boldsymbol{x}-\boldsymbol{x}',h)\,d\boldsymbol{x}' \tag{2-27}$$

It can be further converted into the following form based on Gauss's theorem:

$$<\nabla\cdot f(\boldsymbol{x})>=\int_{\Sigma}f(\boldsymbol{x}')\,W(\boldsymbol{x}-\boldsymbol{x}',h)\cdot\boldsymbol{n}dS-\int_{\Omega}f(\boldsymbol{x}')\cdot\nabla W(\boldsymbol{x}-\boldsymbol{x}',h)\,d\boldsymbol{x}' \tag{2-28}$$

where Σ is the surface of the integral domain Ω, and $\boldsymbol{n}$ is the unit vector normal to the surface Σ. From the above derivation, it is easy to conclude that the complicated differential operation on the function $f(\boldsymbol{x})$ has been migrated to similar procedures on smoothing function W. In other words, the kernel approximation of the derivative of

function $f(\boldsymbol{x})$ is merely determined by the values of $f(\boldsymbol{x})$ and the derivatives of smoothing function W, simplifying the solution process significantly.

If the support domain is located within the integral domain, the surface integral in Equation 2-28 should equal zero. Thus, in this case, Equation 2-28 can be simplified as follow:

$$< \nabla \cdot f(\boldsymbol{x}) >= - \int_{\Omega} f\ (\boldsymbol{x}') \cdot \nabla W(\boldsymbol{x} - \boldsymbol{x}', h)\, d\boldsymbol{x}' \tag{2-29}$$

In SPH formulation, the system is divided into many particles carrying physical quantities and material properties, so the next step is to achieve particle approximation.

The particle approximation is obtained by substituting the infinitesimal volume $d\boldsymbol{x}'$ in kernel approximation with the finite volume of particle j (V_j) where $d\boldsymbol{x}'$ is located. The relationship between the volume of particle j and its mass (m_j) is shown below:

$$V_j = \frac{m_j}{\rho_j}\ (j = 1, 2, \dots, M) \tag{2-30}$$

where ρ_j denotes the density of each particle. M is the number of SPH particles inside the support domain centred on particle j.

Therefore, the function $f(\boldsymbol{x})$ can be rewritten into:

$$f(\boldsymbol{x}) = \sum_{j=1}^{M} \frac{m_j}{\rho_j} f(\boldsymbol{x}_j) W(\boldsymbol{x} - \boldsymbol{x}_j, h) \tag{2-31}$$

At particle i, the particle approximation of function $f(\boldsymbol{x})$ can be accordingly obtained by simply changing $\boldsymbol{x}$ into $\boldsymbol{x}_i$:

$$\begin{cases} < f(\boldsymbol{x}_i) >= \sum_{j=1}^{M} \frac{m_j}{\rho_j} f(\boldsymbol{x}_j) W_{ij} \\ W_{ij} = W(\boldsymbol{x}_i - \boldsymbol{x}_j, h) \end{cases} \tag{2-32}$$

where W_{ij} is the smoothing function for particles.

The particle approximation for the derivative of function $f(\boldsymbol{x})$ can be presented in the same fashion:

$$\begin{cases} < \nabla \cdot f(\boldsymbol{x}_i) >= -\sum_{j=1}^{M} \frac{m_j}{\rho_j} f(\boldsymbol{x}_j) \nabla_i W_{ij} \\ \nabla_i W_{ij} = \frac{\boldsymbol{x}_i - \boldsymbol{x}_j}{r_{ij}} \frac{\partial W_{ij}}{\partial r_{ij}} = \frac{\boldsymbol{x}_{ij}}{r_{ij}} \frac{\partial W_{ij}}{\partial r_{ij}} \end{cases} \tag{2-33}$$

where r_{ij} is the distance between particle i and particle j.

It is worth mentioning that several derivation steps and results were omitted. More techniques for deriving SPH formulations can be found in available monographs [70,71].

Since then, the codes of SPH formulation have been embedded in commercial engineering software such as ANSYS/LS-DYNA and Abaqus/Explicit. Figure 2.8 illustrates the calculation cycle of SPH formulation in LS-DYNA [72].

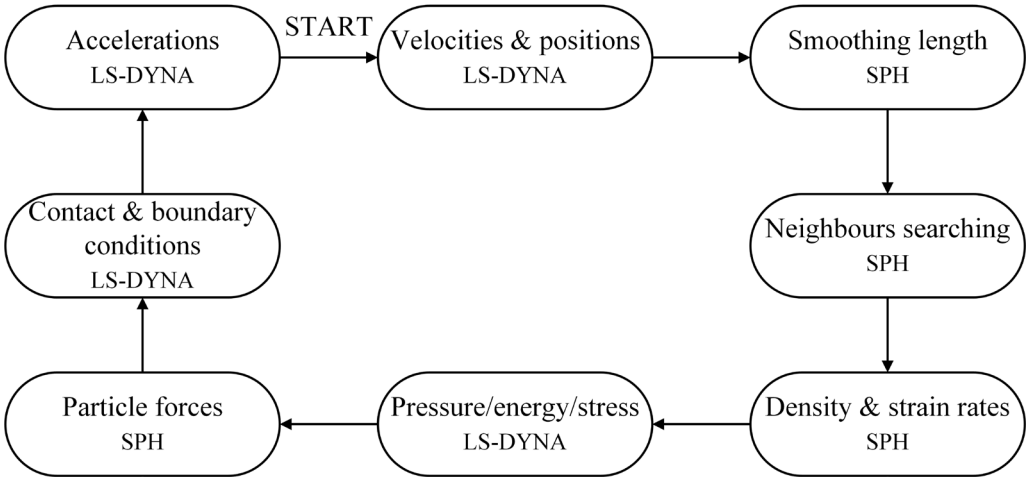

Figure 2.8 Calculation cycle of SPH formulation in LS-DYNA.

In addition, the use of pre-post processing software, such as LS-PrePost, also accelerates the implementation of SPH algorithm in modelling and simulation of micro-cutting.

2.8.2 Corrected SPH formulation

It has been over a decade since the first application of conventional SPH formulation to the modelling and simulation of high-speed metal cutting [73]. However, researchers are still encountering several tough and common problems, such as underestimation of the cutting force, chip thickness and chip curve [74–76]. Compared with FE modelling, straight chips instead of curled ones were generated when using conventional SPH formulation. This is due to the absence of neighbours for the particles on the boundary. So the conventional SPH cannot correctly approximate on the boundary where chip bending happens. Not only that, in such a mesh-free numerical method, the particle distribution severely impacts its calculation accuracy [77]. The squeeze between tool and workpiece will trigger a great disorder of particle distribution, decreasing the accuracy and stability of the simulation. In conclusion, although the conventional SPH method is suitable for modelling and simulation of the micro-cutting process, corrected SPH algorithms are desperately needed to improve its accuracy and stability. Many attempts have been made to overcome these defects [78–83].

For instance, based on the efforts of Randles et al. [84] and Vila [85], LS-DYNA developed a corrected SPH formulation. This correction is named renormalization or renormalized SPH formulation [86]. After its adoption, a better prediction on the chip curve can be observed compared with conventional SPH formulation [87]. In addition, the evolution of chip morphology from continuous to discontinuous was also accurately reproduced without defining the chip separation criterion.

Another popular corrected algorithm named density correction has been employed to correct the density field, using Moving Least Squares (MLS) formulation [81]. This correction has already been applied to the simulation of interfacial flow [88]. Impact surface erosion (usually treated as a micro-cutting process) was also studied using MLS correction [89]. Note that MLS corrected formulation only modify the kernel function and its gradient, so this correction can be conveniently manipulated without changing the main structure of the SPH codes.

2.8.3 Hybrid FE-SPH formulation

In general, the calculation efficiency of SPH formulation is lower than FEM. In addition, SPH formulation has inherent limitations in treating boundary conditions compared with FEM. Thus, the hybrid FE-SPH formulation was proposed to combine both advantages of SPH and FEM, and it has been applied to simulate a wide range of dynamic problems [90,91], including the micro-cutting process [92–94]. One of the first hybrid formulations was developed by Attaway et al. [95]. A contact algorithm was employed in this formulation, coupling SPH nodes with FE surfaces [96,97]. The FE surface is the master surface, whereas the SPH nodes are the slave nodes. Thus this coupling is also known as master-slave coupling [98]. The coupling contact algorithm is available in LS-DYNA, and the flowchart of the coupling process is shown in Figure 2.9 [91].

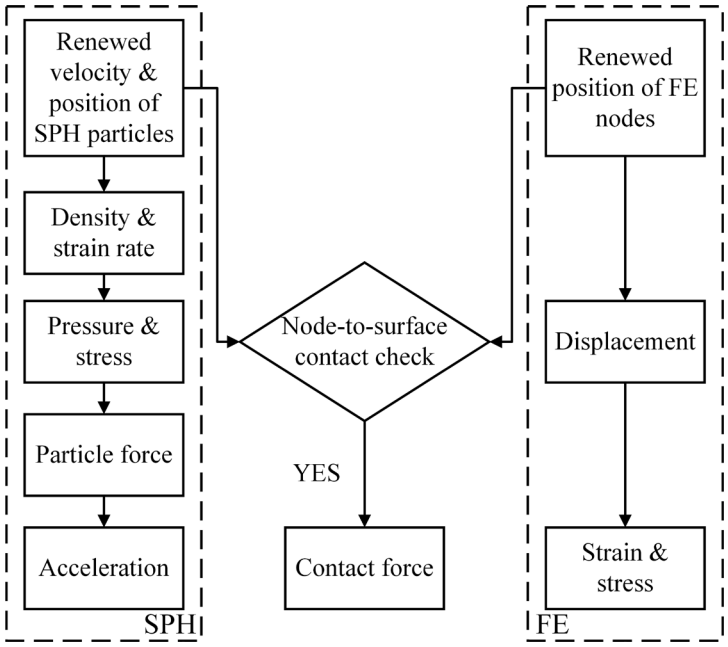

Figure 2.9 Flowchart of FE-SPH coupling process.

The modelling strategy used in this thesis is as follows. The cutting zone with a large strain and strain rate is modelled using the SPH domain to address the issue of large deformation. In contrast, the FE domains represent the cutting tool and the remaining workpiece to decrease the model scale and shorten the computing time.

2.8.4 Material constitutive model

Material constitutive models are essential in SPH simulation of the micro-cutting process, as they determine the dynamic behaviour of damaged material. Various material models have been employed in the SPH method.

2.8.4.1 Johnson-Cook material model

Johnson-Cook model is widely used to describe the material properties of ductile materials such as copper, aluminium and steel [99–101]. This constitutive model was initially developed by Johnson and Cook [102] to describe the dependence of yield

stress (σ_y) on effective plastic strain (ε_p), normalized effective plastic strain rate ($\dot{\varepsilon_p}^*$) and normalized temperature (T*) for ductile materials:

$$\begin{cases} \sigma_y = \left[A + B(\varepsilon_p)^n\right]\left[1 + C\, ln(\dot{\varepsilon_p}^*)\right]\left[1 - (T^*)^m\right] \\ \dot{\varepsilon_p}^* = \dfrac{\dot{\varepsilon_p}}{\dot{\varepsilon_0}} \\ T^* = \dfrac{(T - T_0)}{(T_m - T_0)} \end{cases} \tag{2-34}$$

where $\dot{\varepsilon_p}$ is the effective plastic strain rate. $\dot{\varepsilon_0}$ represents the reference strain rate. T_0 is the ambient temperature, and T_m is the material melting temperature. T is the actual temperature. Johnson-Cook model has wide applications in predicting the yield strength and failure process of ductile materials under large strains, high strain rates and temperatures. The material parameter A is the initial yield stress at a low strain. Parameter B is the strain hardening constant, and C reflects the strain rate effect. m and n are constants related to material properties.

Olleak et al. [103] studied the influence of five sets of Johnson-Cook material parameters on the SPH cutting simulation of AISI 316L stainless steel, based on available literature [104–106]. The simulation results show that the selection of material parameters can seriously impact the cutting force and the distribution of residual stress. Similar research was conducted on titanium alloy Ti-6Al-4V [107], based on four groups of material parameters [108–111]. Hence, all the material parameters should be determined prudently.

2.8.4.2 Johnson-Holmquist damage material model

Johnson-Holmquist model is mainly used to model the damage behaviours of brittle materials, such as ceramics and optical glass [112,113], under large pressures, shear

strain and high strain rates. It is the revised version of Johnson-Holmquist model after introducing Hugoniot Elastic Limit (HEL). The normalized effective stress σ^* is:

$$\begin{cases} \sigma^* = {\sigma_i}^* - D_d\left({\sigma_i}^* - {\sigma_f}^*\right) \\ {\sigma_i}^* = A(P^* + {P_t}^*)^n(1 + C\ ln\ \dot{\varepsilon}^*) \\ {\sigma_f}^* = B(P^*)^m(1 + C\ ln\ \dot{\varepsilon}^*) \end{cases} \tag{2-35}$$

where σ_i^* represents the normalized intact equivalent stress and σ_f^* is the normalized fracture stress. A, B, C, m and n are material parameters. D_d is the material damage parameter.

The general form of normalized stresses (σ^*, σ_i^* and σ_f^*) is shown below:

$$\sigma^* = \sigma/\sigma_{HEL} \tag{2-36}$$

where σ is the actual effective stress, and σ_{HEL} denotes the effective stress in HEL. Likewise, the normalized pressure is $P^*=P/P_{HEL}$, and P represents actual pressure. Besides, P_{HEL} is the pressure in HEL. The normalized tensile hydrostatic pressure is $P_t^*= P_t/P_{HEL}$. P_t is the maximum tensile hydrostatic pressure.

The normalized strain rate $\dot{\varepsilon}^*=\dot{\varepsilon}/\dot{\varepsilon_0}$. $\dot{\varepsilon}$ is the actual strain rate. The reference strain rate $\dot{\varepsilon_0}$ is generally 1.0 s^{-1}.

The definition of damage parameter D_d ($0 \le D_d \le 1$) is:

$$\begin{cases} D_d = \sum \dfrac{\varepsilon^P}{\varepsilon_f^P} \\ \varepsilon_f^P = D_1(P^* + {P_t}^*)^{D_2} \end{cases} \tag{2-37}$$

where ε^P is the actual plastic strain. ε_f^P is the plastic strain to fracture under actual pressure P. D_1 and D_2 are material parameters related to damage. The material is intact when $D_d = 0$, whereas the fracture occurs when $D_d = 1$.

2.8.4.3 Cowper-Symonds material model

Cowper-Symonds material model is a simple elastoplastic material model considering the isotropic/kinematic hardening plasticity. The stress-strain curve of this model consists of two linear stages (i.e. elastic stage and plastic stage) [114]:

$$\begin{cases} E = \dfrac{d\sigma}{d\varepsilon}, \sigma < \sigma_y \\ E_{TAN} = \dfrac{d\sigma}{d\varepsilon}, \sigma > \sigma_y \end{cases} \tag{2-38}$$

where E is the Young's modulus of the work material. σ is the actual effective stress. σ_y is the yield stress. E_{TAN} is the tangent modulus which is the slope of the stress-strain curve at the plastic stage. In general, the tangent modulus equals a few percentages of the material's Young's modulus [115,116].

Moreover, Cowper-Symonds model scales the quasi-static yield stress by two factors related to the dynamic strain rate [92,117]:

$$\begin{cases} \sigma_d = \left[1 + \left(\dfrac{\dot{\varepsilon}_d}{D}\right)^{1/p}\right](\sigma_s + \beta E_p \varepsilon_d) \\ E_p = E_{TAN} E/(E - E_{TAN}) \end{cases} \tag{2-39}$$

where σ_d is the dynamic yield stress and σ_s is the static yield strength. ε_d and $\dot{\varepsilon}_d$ are the dynamic strain and strain rate, respectively. E_p is the plastic hardening modulus. D and p are a set of material parameters. Parameter p is dimensionless, while parameter D has the same unit as strain rate. Parameter β is the material hardening parameter, which can be used to manipulate isotropic, kinematic or a mix of isotropic and kinematic hardening.

2.8.4.4 Other material models and equations

The selection of the constitutive model has a significant influence on simulation accuracy. For example, the Johnson-Cook model has a good performance in low strain

rate conditions [72], but it cannot handle dynamic problems such as angular impact with a high strain rate in the order of 10^5 s^{-1}. Takaffoli and Papini [92] set the material parameter *C* in Johnson-Cook model as zero and substituted it with Cowper-Symonds model [118]. The performance of this modification was evaluated when modelling the angular impact of Al6061-T6. In this case, the angular impact was regarded as a pure orthogonal micro-cutting process. The simulation results show that the Cowper-Symonds model predicts the penetration depth, crater pile-up height, and rebound velocity with higher accuracy than Johnson-Cook model does.

Calamaz et al. [119] made a similar modification to Johnson-Cook model when modelling the machining process of titanium alloy Ti-6Al-4V. In this modified formulation, a new method named Hyperbolic TANgent was introduced to consider the effect of strain softening. The simulation results reveal that the chip formation and strain distribution predicted using this new formulation are consistent with experimental results. Niu et al. [120] expanded this new formulation to the simulation of Ti-6Al-4V micro-cutting using SPH method, also demonstrating its high accuracy compared with the conventional Johnson-Cook model.

Besides the models mentioned above, Puff hardening model [121] was introduced to simulate the micro-cutting process of the fibre-reinforced composite. A numerical model for orthogonal cutting of copper [122] was developed using Wilkins radial return plasticity model [123]. The depth of cut was in hundreds of nanometres in this work. The modelling of bone tissue was achieved using Hill's anisotropic yield criterion and progressive material degradation [124]. Crystal-plasticity constitutive model based on Schmid law [125] was introduced to model crystal copper. Chen and Kulasegaram [81] proposed a novel SPH methodology that combines penalty

formulation with a bilinear interface cohesive law [126]. This method can handle the fibre/particulate interface without material homogenization and has been applied to simulate the debonding process within the particulate composites.

2.8.5 Particle density

As a numerical method, the selection of optimal solver parameters is of vital importance for SPH formulation, which is also called sensitivity analysis. This is because the solver parameters even have the same level of influence on the simulation accuracy as the material constitutive models [127]. Several solver parameters, such as smoothing length, mass-scaling, and particle density, are usually concerned in SPH technique. Hence it has to be determined reasonably. Related research indicated that particle density has a more significant effect on prediction accuracy for micro-cutting than smoothing length and mass-scaling [127].

The total number of particles in an SPH model affects the computing time. But their relationship is not a linear function. Instead, there is a $M\log M$ relationship between computation time and the total number of SPH particles M [128]. Heisel et al. [127] investigated the influence of particle density (also called spacing or resolution in some references) on the computing time and simulation error. The distance between each neighbour particle is usually used to represent the particle density. A higher particle density denotes a larger initial particle distance. They pointed out that a higher particle density would decrease the computation time but increase the simulation error. Thus, to seek the delicate balance between computing time and simulation accuracy, many efforts have been made to conduct sensitivity analysis on particle density [92,129]. Takabi et al. [130] observed an opposite convergence trend in FE and SPH

formulations. A finer FE mesh resulted in a higher cutting force, whereas a similar phenomenon can only be observed under a coarse particle distribution for SPH method. This is because, under a higher particle density, every particle represents a higher volume of the workpiece. Therefore, a larger-size chip is accumulated, leading to a higher cutting force. Rosswog et al. [131] argued that the cutting force has already converged to a constant level when the particle resolution is not very high (8000 particles per cm^3). It is worth mentioning that blindly increasing the number of SPH particles will not help increase the simulation accuracy but bring about huge computational costs.

2.8.6 Studies on cutting mechanics and mechanism

As shown in Figure 2.10, SPH method has made a good contribution to investigating cutting mechanics and mechanisms in micro-cutting. For example, the chip formation and its morphology, the material removal mechanism of brittle materials, especially the initiation and propagation of cracks, and the effects of crystal anisotropy have been studied with the aid of SPH method.

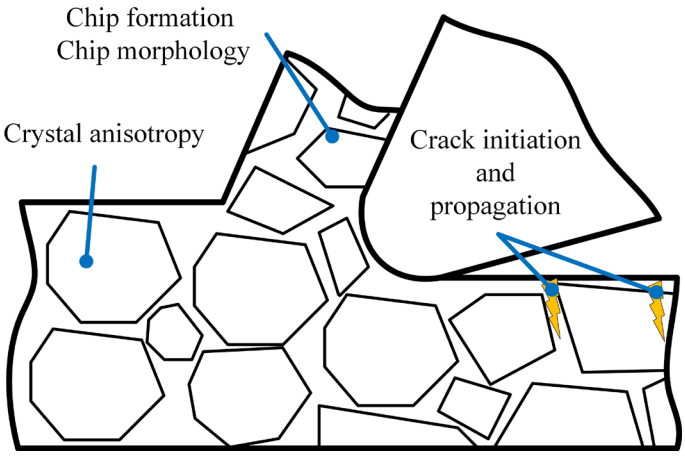

Figure 2.10 Typical research topics in micro-cutting.

2.8.6.1 Stress and strain distribution

As the fundamental variables in micro-cutting mechanics, stress, strain and strain rate are needed to be identified for further research on cutting mechanisms. Compared with FEM, especially Eulerian formulation, SPH method has a better performance in predicting the distribution of residual stress in the machined surface [132–134]. For example, Islam [135] argued that the stress and strain distribution predicted using SPH method agrees well with the results from cutting experiments on 1100 aluminium [136,137].

In most cases, the accumulation of residual stress on the machined surface can shorten the operating life of the components, but residual stress is desirable in certain situations. The effect of sequential cutting of oxygen-free copper was studied by Zhao et al. [138]. In this study, the residual stress can be observed on the machined surface after the first cut. After that, more curling and thinner chips were generated in the second cut. The cutting force in the second cut is smaller than those in the first cut, even with the same depth of cut. In this case, the residual stress induced by the first cut has a positive effect because the advent of residual stress makes the material easier to be peeled off. Due to the thermal softening effect, the micro-cutting becomes easier with the assistance of the laser beam. Balbaa and Nasr [139] found the difference between conventional and laser-assisted cutting. They pointed out that conventional cutting would trigger tensile residual stresses. However, the laser beam induced the compressive residual stresses, which resulted in a lower cutting force in the subsequent machining process.

The formation of shear bands and shear-localized chips can be attributed to the accumulation of shear stress in the cutting chips. With the aid of SPH technique, Xi et al. [93] found that cracks can always initiate and propagate in the primary shearing zone where maximum shear stress is localized in micro-cutting of Ti-6Al-4V alloy. SPH technique also captured the shear stress within the cutting zone when machining carbon steels 45R and 60R [107].

Besides ductile materials, the stress and strain distribution in grinding of the brittle material (e.g. SiC) was studied with the aid of SPH simulation [140]. When the indentation depth is smaller than 0.105 μm, wave-like stress can be observed in the workpiece surrounding the indenter, but no plastic strain is detected. The crack initiates, and the plastic strains start to be observed after increasing the indentation depth. The plastic strain can be observed on the workpiece surface and along the tips of the cracks. This phenomenon is consistent with the experimental results [141–143].

2.8.6.2 Chip formation and chip morphology

Chip formation is a fundamental issue in micro-cutting, as it indicates the material removal behaviours under specific cutting conditions and the interactions at the tool/chip interface. SPH simulation is becoming an effective method to research the mechanism of chip formation and its morphology in the micro-cutting process due to its natural tool/workpiece separation and ability to handle large deformation. An SPH numerical model was first developed by Limido et al. to investigate the chip formation in high-speed micro-cutting of Al6061-T6 and 4340 steel [144]. Figure 2.11 (a) shows that this novel model successfully predicted and visualized the formation of continuous

chips with up-curling. Both primary and secondary shear zones can be observed despite the underestimated chip thickness.

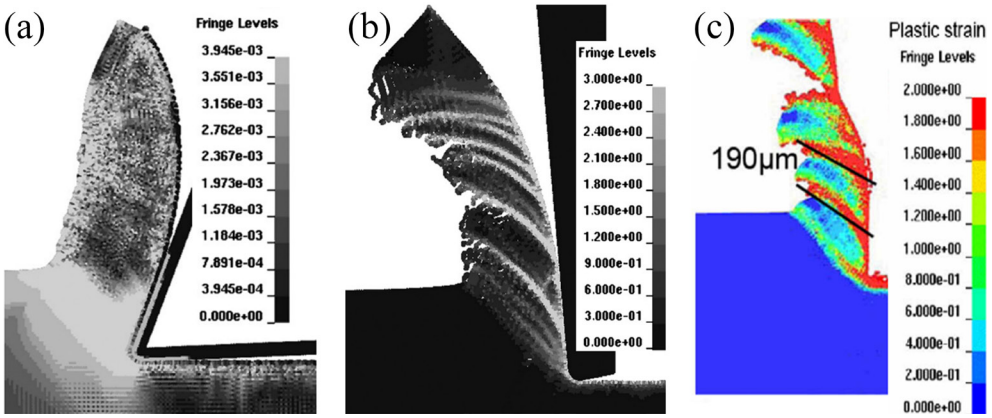

Figure 2.11 Simulated chips morphologies: (a) continuous chip [144]; (b) serrated chip [144]; (c) serrated chip [107].

In the simulation of micro-cutting of 4340 steel, the cyclic adiabatic shear band-dominated serrated chip formation was also observed [144]. Moreover, it was found that both cutting forces in tangential and normal directions obtained from SPH simulation were about 10% and 30% smaller than the experimental values.

Inspired by this pioneering research, many researchers are trying to adopt SPH to investigate micro-cutting of steel. A similar SPH simulation work for diamond turning of 4340 steel was conducted [145]. The maximum shear stress and plastic strain were observed at the primary deformation zone, where intense extrusion and material slip took place. The chip formation process can be divided into three phases: elastic mode, plastic mode and breaking separation mode, despite underestimating the chip radius of curvature. Also, a sequential cutting model for multi-grain micro-cutting of armour steel 4043 was developed [146]. Simulation results show that a heat-affected zone was formed due to a large quantity of heat generated by crashing and extruding between

the first two grains and the workpiece. The interferences phenomenon among three grains in chip formation was observed. The chip generated by the third grain was squeezed to fracture because of the material softening effect of the heat-affected zone. For the same reason, the cutting force from the last grain was the smallest.

The formation of serrated chips is a typical phenomenon in the micro-cutting of titanium-based materials. An SPH micro-cutting model for Ti-6Al-4V titanium alloy with a new and worn tungsten carbide tool edge was constructed [107]. Figure 2.11 (c) illustrates that serrated chips were successfully obtained. Nevertheless, the distance between two adjacent shear bands in simulations is 20% shorter than those in experiments.

Demiral [147] conducted the first investigation on the influence of vibration parameters (e.g. frequency and amplitude) on chip morphology in vibration-assisted cutting of titanium alloy. The simulation results reveal that the tool vibration can significantly reduce the cutting force. Besides, due to the external energy applied to the cutting tool, localized stress and temperature in the cutting area increased significantly, thereby influencing the chip morphology. The chip curve is therefore increased, and the chip thickness is decreased with the increase of vibration amplitude. At the same time, the vibration amplitude has a much greater influence on chip morphology than the frequency does.

In summary, chips with different shapes were predicted successfully in micro-cutting of aluminium, steel and titanium alloy. The initiation and evolution mechanism of the chip formation was revealed with the aid of SPH simulation. However, the underestimation of chip thickness and chip radius of curvature is a common issue for many SPH simulations. It might be due to the less of neighbour particles on the

boundary of the workpiece and the distorted particle distribution on chips. As discussed before, corrected SPH algorithms are desperately needed to improve the prediction accuracy on chip morphology.

2.8.6.3 Material removal mechanism of brittle materials

In order to get high-quality machined surfaces without cracks, micro-cutting of brittle materials should always take place in the ductile mode where the work material is removed continuously. The maximum depth of cut under the ductile mode cutting is usually called critical depth of cut. Thus, it is essential to determine the critical depth of cut of brittle materials.

Duan et al. [148] conducted the hybrid FE-SPH simulation for the scratching process of monocrystal SiC, which was simplified as a micro-cutting process. Three material removal mode of SiC was illustrated through the simulation results: ductile removal mode, ductile-brittle transition mode and brittle removal mode. SPH simulation and experimental analysis were investigated by Liu et al. [149] to predict the critical depth of cut of SiC. The three-mode material removal evolution was observed from the simulation results with the continuous increase of depth of cut. According to the crack evolution, surface roughness and the peak value of cutting force, the critical depth of cut of ductile-brittle transition was determined to be 0.35 μm.

Similar work on K9 glass was carried out by Nam et al. [150]. The discontinuous chips were obtained, and residual stress distribution was observed below the machined surface. The model proposed in this literature aims to guide the selection of appropriate processing parameters such as cutting speed and depth of cut to improve the machined surface profile. The modelling and simulation for diamond turning of K9 glass were

investigated by Guo et al. [151] to identify its critical depth of cut. The SPH simulation results imply that the ductile mode cutting can be achieved once the depth of cut is between 0.2 μm and 0.3 μm.

2.8.6.4 Effect of crystal anisotropy

Crystal anisotropy has a critical influence on chip formation, machined surface quality and cutting productivity because the work material has different mechanical properties on different crystal orientations.

Anisotropic materials can be addressed by SPH technique after introducing corresponding constitutive models. As mentioned before, the bone tissue was modelled as a homogenized elastoplastic material with isotropic properties after adopting Hill's anisotropic yield criterion and progressive material degradation [124]. Its simulation results reveal that the cutting forces have a large dependency on orientations. Higher cutting forces were observed in the direction that is perpendicular to osteons compared with those in the parallel direction.

A similar study was carried out by Zahedi et al. on f.c.c. copper [94]. The orthogonal micro-cutting process of f.c.c. copper was modelled using a crystal-plasticity material model. Chips with different thicknesses were generated on (100), (101) and (111) planes, illustrating the significant influence of crystal orientation on chip morphology. At the same time, the cutting force on (101) plane was the largest among all these three., Abolfazl et al. [152] developed an SPH model for vibration-assisted cutting of f.c.c. single crystal, in which the tool vibration was treated as a displacement boundary condition. The simulation results illustrated that the cutting force on (101) orientation with a 30° cutting direction is the smallest.

In summary, bone tissue, a typical composite material, has been successfully modelled using a homogenization treatment [124]. Inspired by this work, a similar treatment will be employed for silk fibroin to simplify its modelling process.

2.9 Summary of knowledge gaps and research challenges

Literature review studies reveal that silk particles with helical or filamentous shapes and specified sizes are believed to have better efficacy for drug delivery than their spherical counterparts. However, current manufacturing approaches are only applicable to the production of spherical particles. In addition, most of them require chemical agents or expensive instruments.

As demonstrated in the literature, controllable chip morphology and chip breaking in diamond turning can be achieved by changing processing parameters. It provides a promising low-cost and chemical-free manufacturing method to realise the scalable production of silk particles with controlled geometry, potentially driving a novel manufacturing paradigm shift of carriers for next-generation medicine.

However, diamond turning of silk fibroin has never been attempted. The underlying chip formation mechanism in diamond turning of silk fibroin is a knowledge gap. Especially, it remains unclear how the hierarchical structure of silk fibroin influences its chip morphology, which is pivotal to the success of process control to obtain silk particles.

Elliptical vibration diamond turning has been proven to be an effective method for chip breaking, so it will be used to obtain filamentous silk particles. Designing and developing a high-frequency non-resonant elliptical vibrator that can be used as a chip breaker in diamond turning is still a technical bottleneck. Significant problems, such

as low structural stiffness, severe cross-axis coupling and overheating of piezo actuators, are needed to be overcome in the design process of a high-frequency non-resonant elliptical vibrator.

SPH formulation can be adopted to predict the chip formation and chip-breaking processes in diamond turning of silk fibroin due to its talent in handling material fracture. However, the lack of an accurate material model that can fully describe the damage behaviour of silk fibroin in diamond turning is also a research challenge.

In addition, to manufacture filamentous silk particles, a clear understanding of how the processing parameters in elliptical vibration diamond turning of silk fibroin affect its chip breakability presents another knowledge gap.

Chapter 3

Evaluation of machinability in diamond turning of silk fibroin

3.1 Introduction

Until now, diamond turning of silk fibroin has never been attempted. As depicted before, the silk fibroin has a hierarchical structure in which its beta-sheet crystallites are embedded in the amorphous matrix. The difference in the mechanical properties of the crystallites and amorphous matrix may reduce the machinability of silk fibroin. Therefore, the machinability in diamond turning of silk fibroin is first investigated.

In the chapter, the silk fibroin solution is firstly prepared and then regenerated into silk fibroin film (hereinafter referred to as silk film) for machining trials. The machinability of silk fibroin is evaluated from the aspects of specific cutting force and chip morphology. The processing parameters that can be used to control the geometry of cutting chips as silk particles are recommended.

3.2 Cutting experiments

3.2.1 Silk fibroin solution preparation

The silk fibroin solution is required to be regenerated into films for diamond turning experiments, which was made from *B. mori* cocoons based on the reported protocol [153]. In brief, the cocoons were boiled for 1 hour in 25 mM Na_2CO_3. The degummed silk was dissolved in 9.3 M LiBr at 60°C for 3 hours and then dialyzed against water over 48 hours (molecular weight cut-off 3500 Da), yielding a 5–6% w/v silk fibroin

solution. The silk solution was diluted to a working concentration of 4% w/v with distilled water.

3.2.2 Preparation of silk film discs

After an overnight air-dry, silk films were regenerated using 5 ml of silk solutions cast on a 70 mm diameter aluminium mould. This procedure was repeated three times to form thicker semitransparent films. The formed amorphous water-soluble silk films have 15.6 mg of silk fibroin per surface unit (cm^2). The samples were kept in a dry vacuum environment at 25°C and 60% relative humidity to avoid structural changes before diamond turning trials. Figure 3.1 illustrates two silk film discs.

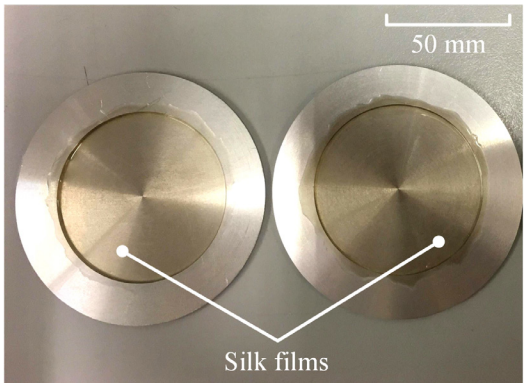

Figure 3.1 Silk film samples on aluminium discs.

3.2.3 Experimental setup

A couple of diamond turning experiments were conducted on a three-axis diamond turning machine. Figure 3.2 illustrates the experimental setup.

A silk disc was mounted on a vacuum chuck of the air spindle. A round nose tool with a rake angle of 0°, a clearance angle of 15° and a nose radius of 0.2 mm was installed on a tool holder to conduct overlapping and non-overlapping cutting trials.

Another group of diamond turning experiments were performed using a 55° sharp point tool with the same rake angle and clearance angle as the round nose tool. A three-component dynamometer (9129AA, Kistler) was mounted underneath the tool holder for measurement of cutting force. Before being collected by a data acquisition card (USB-1608HS, Measurement Computing), the force signals were amplified with a charge amplifier (5070A, Kistler). Furthermore, a scanning electron microscope (SEM) (FEI Quanta 3D FEG) was used to observe the cutting chips.

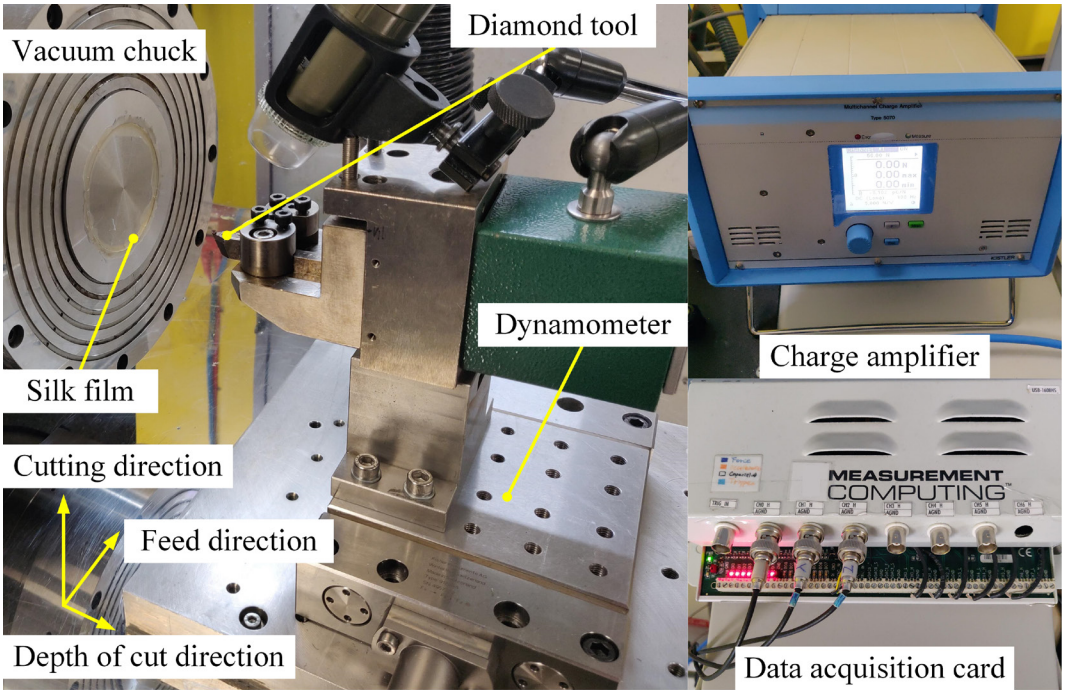

Figure 3.2 Setup for diamond turning experiments.

3.2.4 Processing parameters and procedure

In diamond turning experiments, the dimension relationship between the depth of cut and the nose radius of the diamond tool is illustrated in Figure 3.3 A_c is the undeformed chip cross-section area. R_c is the tool nose radius, and d_c is the depth of cut. All the experiments fall into five sets, which are designated by Roman numerals

I, II, III, IV and V in Table 3.1. Experiments of set I were performed to study the effects of cutting speed and depth of cut on the specific cutting force and chip morphology. The influences of feed rate and tool shapes (i.e. sharp-point tool and round nose tool) on chip morphology were studied in experiments of sets II and III. Moreover, experiments of sets IV and V were conducted to investigate the effect of processing parameters (i.e. cutting speed, depth of cut and feed rate) on chip morphology.

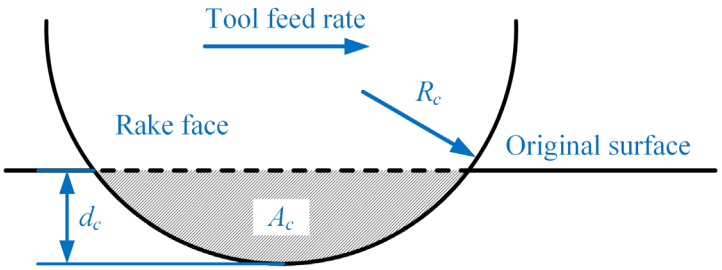

Figure 3.3 View normal to the rake face of a round nose tool in diamond turning experiments.

Table 3.1 Processing parameters chosen for diamond turning experiments.

Set	Cutting mode	Nose radius (mm)	Cutting speed (m/s)	Depth of cut (μm)	Feed rate (μm/rev)
I	Non-overlapping	0.2	0.027; 0.054; 0.108; 0.27; 0.81: 1.35	1.5; 2	150
II	Overlapping	0.2	1.35	5	1; 2.5; 5
III	Sharp-point cutting	N/A	1.35	5	1; 2.5; 5
IV	Non-overlapping	0.5	0.027; 0.054; 0.27	1; 1.5; 2	150
V	Overlapping	0.5	1.35; 2.7	1; 1.5; 2	2.5; 5; 20

Based on the relationship illustrated in Figure 3.3, while using the round nose tool, it can be expected that overlapping cutting will be carried out when the feed rate is less than 20 μm/rev. Meanwhile, when the feed rate is 150 μm/rev, the experiments will be performed under non-overlapping cutting mode.

In non-overlapping cutting, the specific cutting force F_s were calculated on the basis of equivalent cutting area to correlate with the simulation results in the following chapters:

$$\begin{cases} F_s = \dfrac{F_c}{A_c} \\ A_c = \dfrac{4\sqrt{2}}{3}\sqrt{R_c {d_c}^3} \end{cases} \tag{3-1}$$

where F_c is the cutting force measured in experiments.

3.3 Results and discussion

3.3.1 Specific cutting force

Figure 3.4 illustrates the specific cutting forces with different cutting speeds and depths of cut in the experiments of set I. It can be demonstrated that the specific cutting forces for 1.5 μm depth of cut are higher than those for 2 μm, which is due to the size effect of the removed chips. This phenomenon typically occurs when the dimension of depth of cut is approaching the scale of the tool edge radius and therefore increases the energy dissipation. Specifically, a smaller depth of cut will trigger higher shear stress and strain rate. Hence the specific cutting force is increased. The results are consistent with similar studies on copper [154], aluminium alloy [155] and polymethyl methacrylate [156]. The specific cutting force can reach about 3700 $\mu N/\mu m^2$ at the cutting speed of 0.027 m/s, and then it decreases dramatically with an increase in the cutting speed. One explanation of this mechanism is that a faster cutting speed will cause more severe thermal softening [157]. However, the decline rate of the specific cutting force begins to decrease when the cutting speed is over 0.27 m/s. It should be due to the fact that with a further increase in cutting speed, a higher amount of heat generated in the primary deformation zone is removed by the cutting chip. Thus the thermal softening is counteracted. In more detail, when the cutting speed is 1.35 m/s, the specific cutting force for 2 and 1.5 μm depth of cut is 529.6 and 640.2 $\mu N/\mu m^2$, respectively.

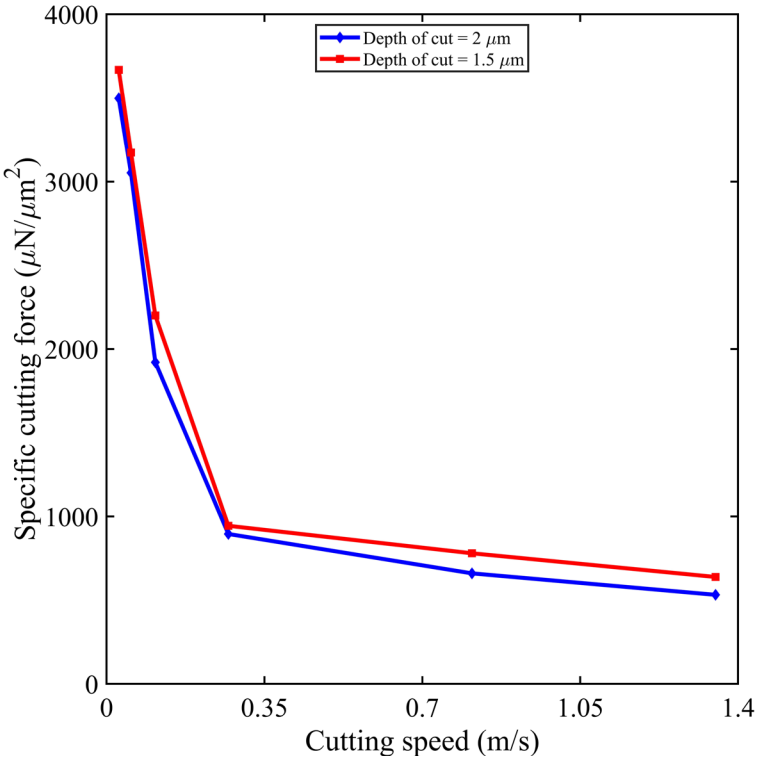

Figure 3.4 Relationship between specific cutting force, cutting speed and depth of cut.

3.3.2 Chip morphology

The SEM images of the silk chips formed in the experiments of set I with a cutting speed of 1.35 m/s are illustrated in Figure 3.5.

The serrated chips were obtained under both depths of cut, where the shear strain localization and chip segmentation can be identified. The back surfaces of the chips are pretty smooth. The chip morphology can be further analyzed using the dimension parameter such as shear band spacing, which will be discussed in Chapter 4 in more detail.

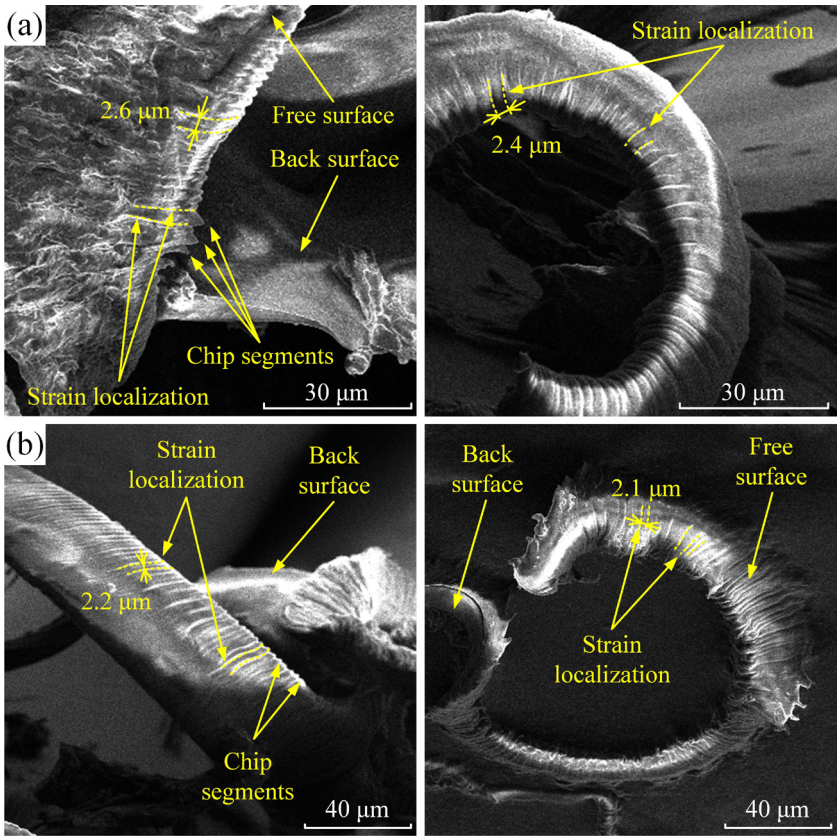

Figure 3.5 Chip morphology obtained in the experiments of set I with a cutting speed of 1.35 m/s: (a) depth of cut d_c = 2 µm; (b) depth of cut d_c = 1.5 µm.

In the experiments of set II, the ribbon particles with periodic folds were obtained, whose schematic is shown in Figure 3.6. The folding wavelength λ_f and chip width w_c are two important dimensional parameters to characterize the morphology of ribbon particles. The SEM images of the silk chips generated in this set of experiments are displayed in Figure 3.7. Moreover, Figure 3.8 illustrates the SEM images of the silk chips generated in set III using the sharp point tool.

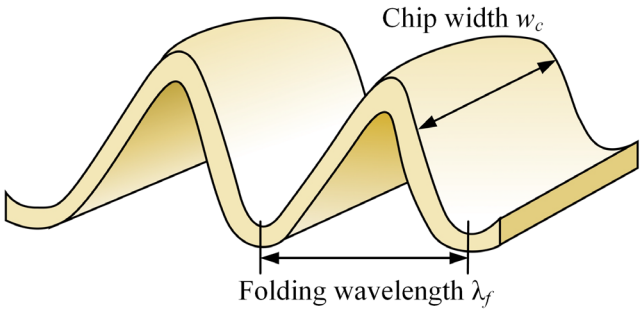

Figure 3.6 Schematic of ribbon particles with periodic folds.

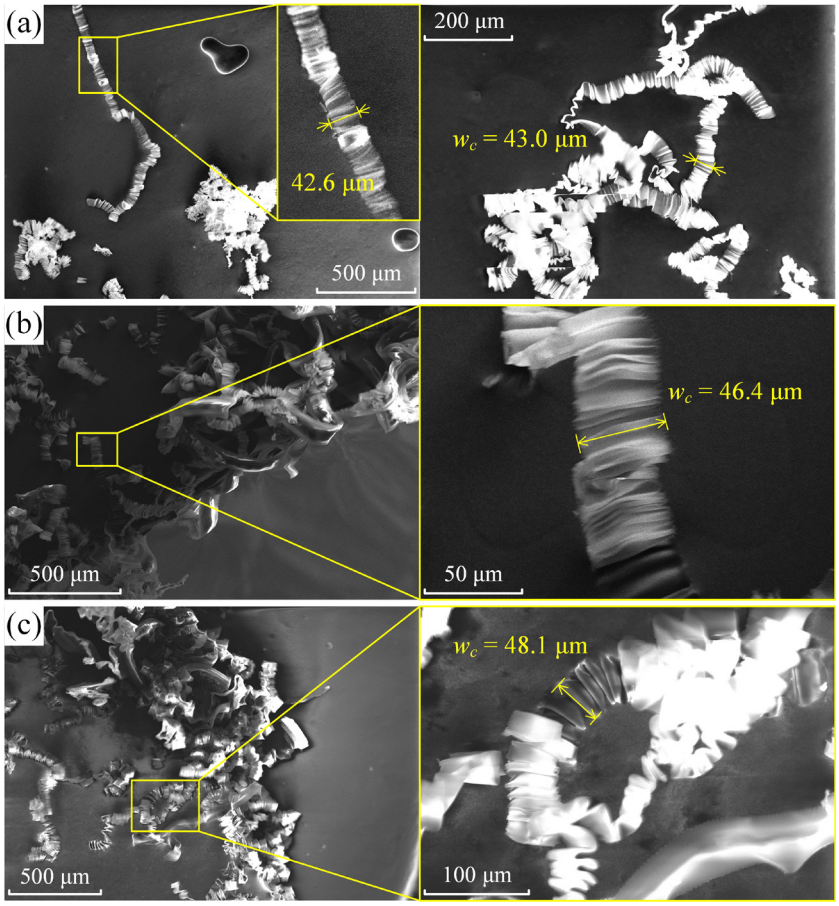

Figure 3.7 Chip morphology obtained in the experiments of set II: (a) 1 µm/rev; (b) 2.5 µm/rev; (c) 5 µm/rev.

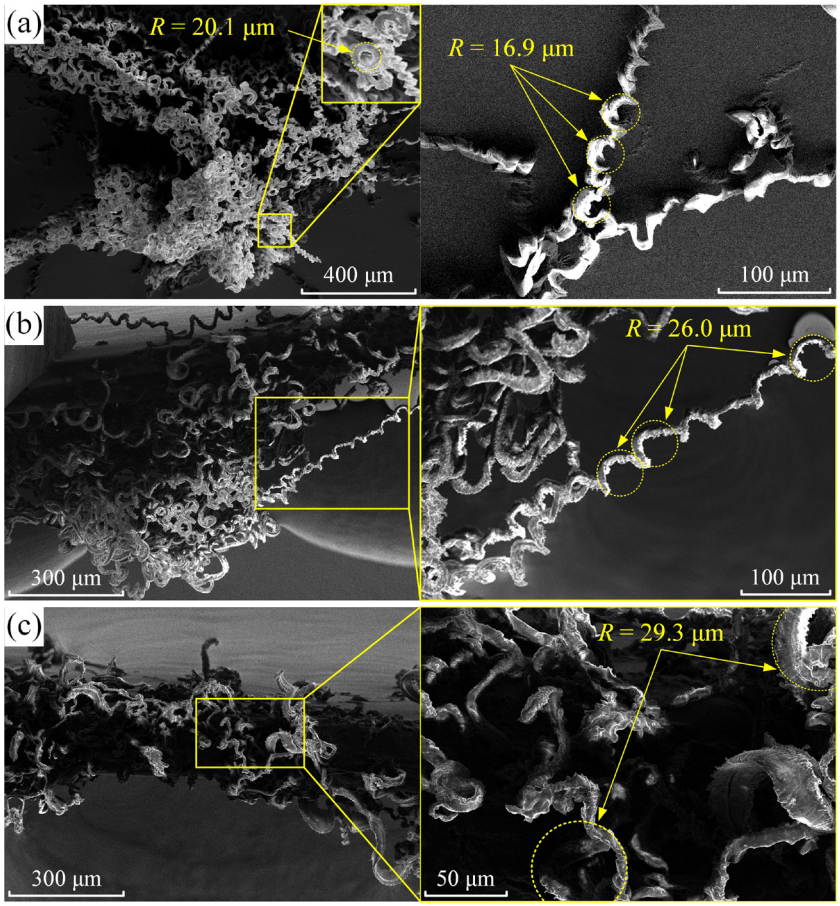

Figure 3.8 Chip morphology obtained in the experiments of set III: (a) 1 μm/rev; (b) 2.5 μm/rev; (c) 5 μm/rev.

As shown in Figure 3.7, the chip width w_c increases continuously with the increase of feed rate. In addition, the helical chips with the tunable radius of curvature R are found in Figure 3.8 (a) and (b). Figure 3.8 (c) illustrates that the helical chips become snarled as the feed rate continuously grows. The chips develop a larger radius of curvature as the feed rate increases, which is because a higher feed rate will increase the chip cross-section and therefore increase the chip stiffness. Overall, a sharp point tool under a lower feed rate (i.e. less than 2.5 μm/rev) processing parameters is preferred to generate helical silk particles.

The SEM images of silk particles generated in the experiments of set IV with a depth of cut of 1, 1.5 and 2 μm are illustrated in Figure 3.9, 3.10 and 3.11, respectively. Long ribbon particles with periodic folds can be identified in all three figures. Figure 3.12 displays the influence of cutting speed and depth of cut on folding wavelengths λ_f. The error bars represent the standard deviation in measurements.

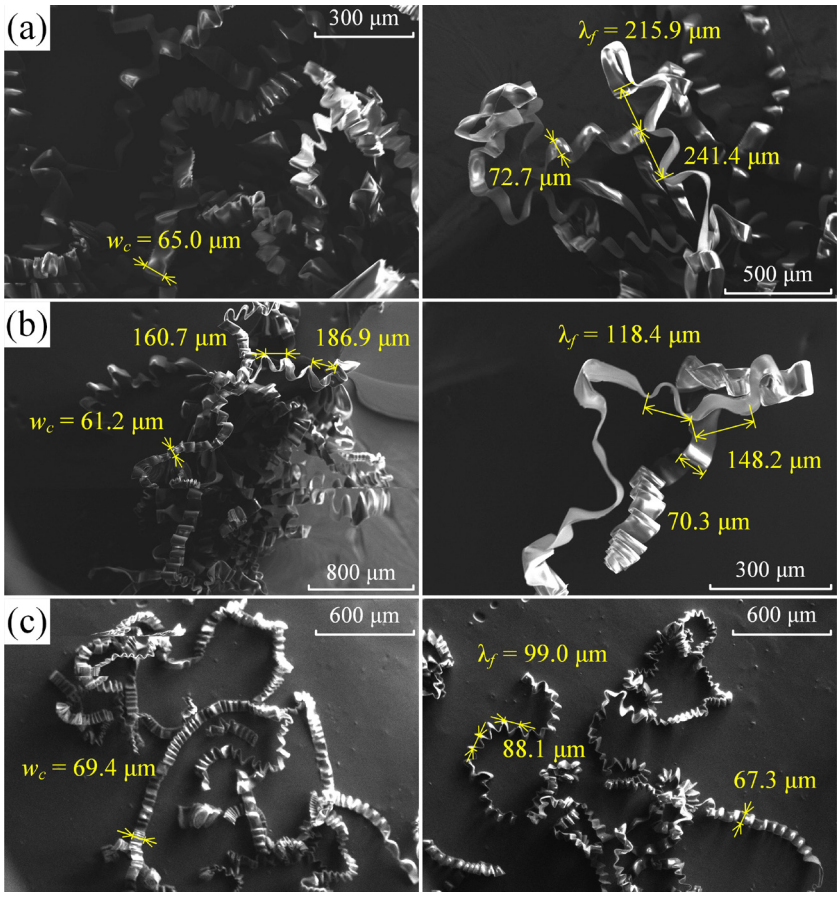

Figure 3.9 Chip morphology obtained in the experiments of set IV with a depth of cut of 1 μm: (a) 0.027 m/s; (b) 0.054 m/s; (c) 0.27 m/s.

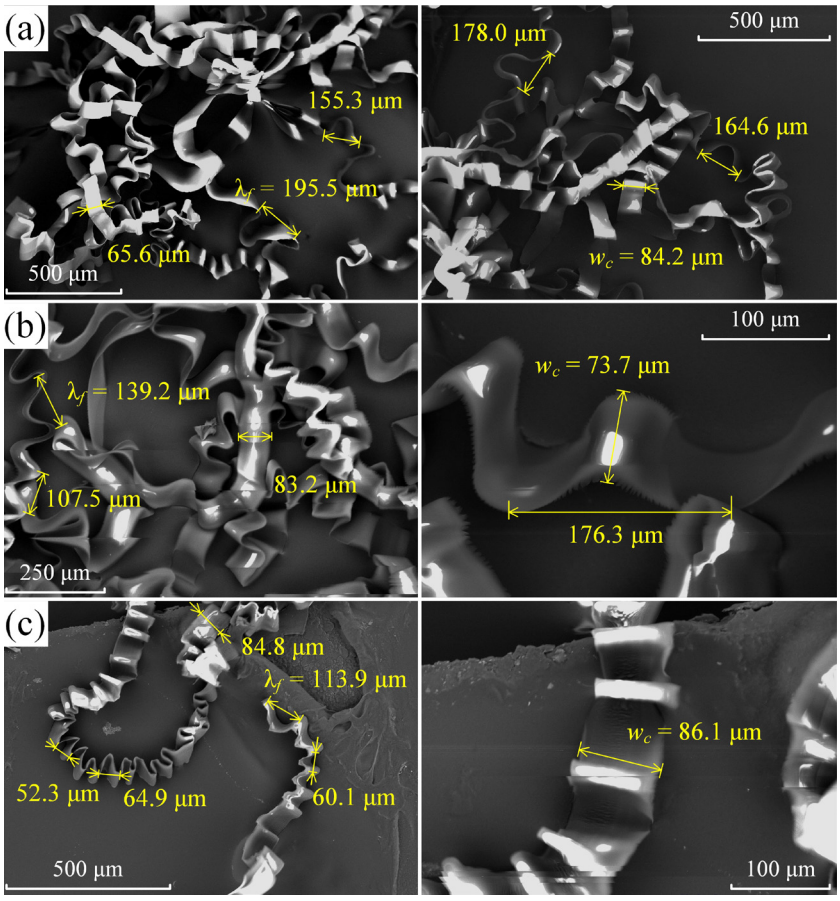

Figure 3.10 Chip morphology obtained in the experiments of set IV with a depth of cut of 1.5 µm: (a) 0.027 m/s; (b) 0.054 m/s; (c) 0.27 m/s.

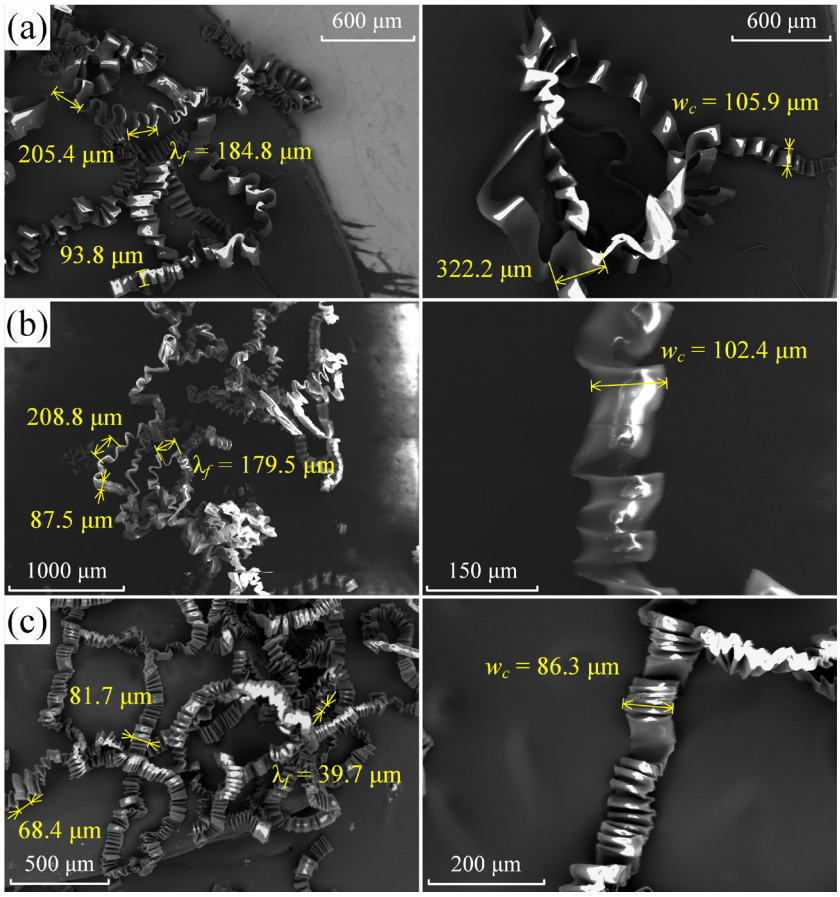

Figure 3.11 Chip morphology in IV with a depth of cut of 2 µm: (a) 0.027 m/s; (b) 0.054 m/s; (c) 0.27 m/s.

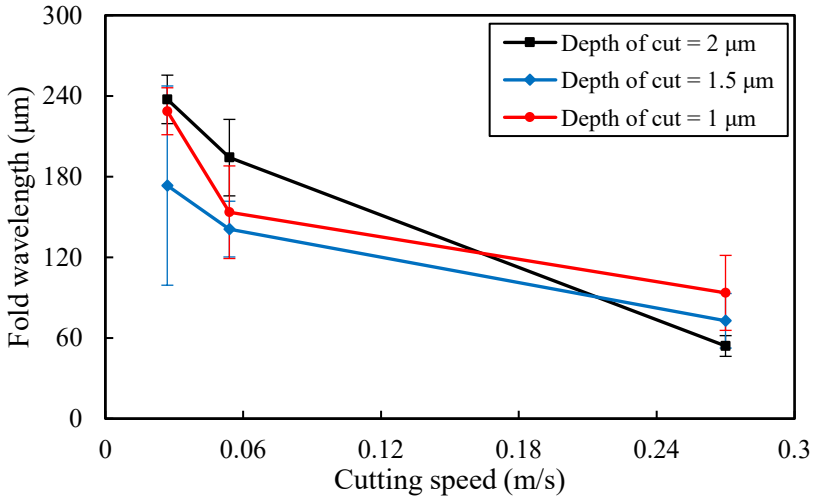

Figure 3.12 Folding wavelength of long ribbon particles obtained in the experiments of set IV.

It can be seen in Figure 3.12 that the folding wavelength λ_f decreases with the increase of cutting speed. As the cutting speed increases, the curling speed of the chip tends to be lower than the chip generation speed. In this case, the chips will undergo a larger deformation under the squeezing action of the cutting tool, thus leading to the decrease of the folding wavelength. Meanwhile, as shown in Figure 3.12, a reduction in the depth of cut will also trigger a smaller folding wavelength due to a smaller chip cross-section.

The chip chart that maps the geometries of silk particles over a feed rate (μm/rev) and depth of cut (μm) matrix is an effective tool for evaluating the machinability of silk fibroin. Figure 3.13 illustrates the chip chart based on the experiments of set V with a cutting speed of 2.7 m/s.

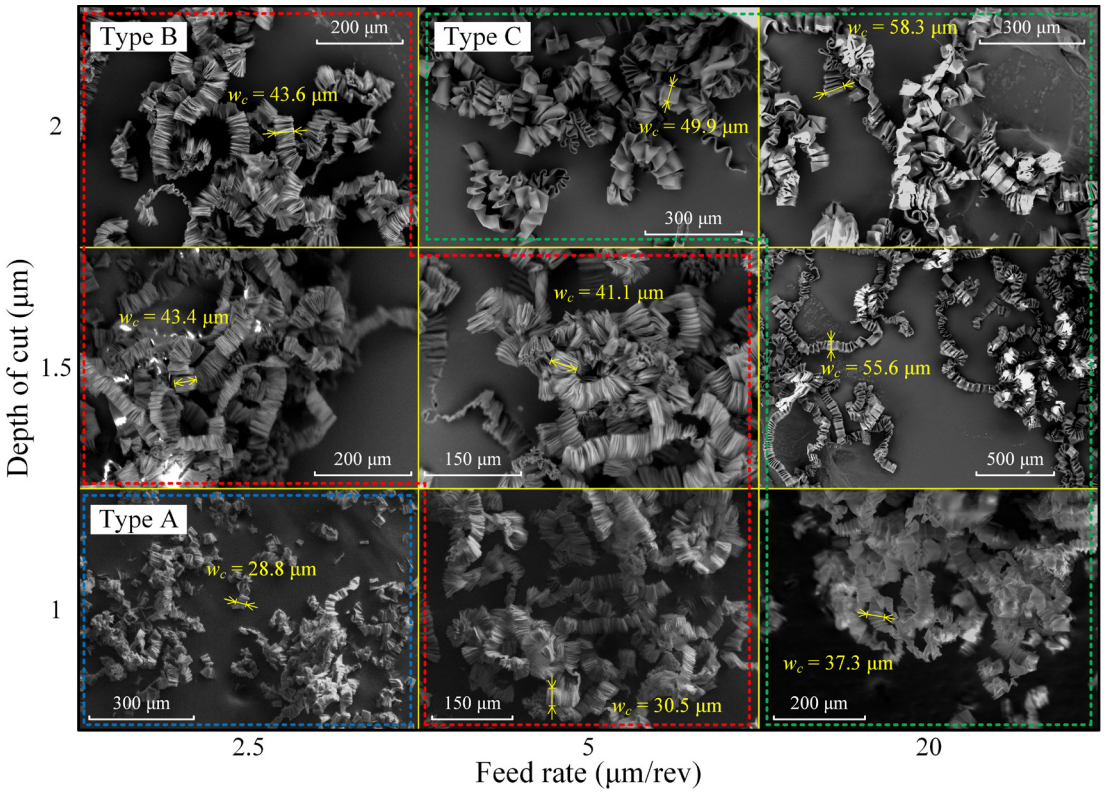

Figure 3.13 Chip chart showing morphologies of silk particles across a feed rate-depth of cut matrix.

As feed rate and depth of cut are reduced simultaneously, the silk particles undergo a significant change from a long ribbon shape (Type C) to a long folded shape (Type B). When the feed rate further decreases to 2.5 μm/rev, and the depth of cut reduces to 1 μm, short and discontinuous folded silk particles (Type A) can be obtained. This means that the breakability of the silk chips increases at reducing feed rate and depth of cut, which is fundamentally different from conventional metallic materials such as 1045 hardened steel [43] and 304 stainless steel [37]. Literature reveals that higher feed rates and depths of cut are beneficial to breaking the steel chips. This difference stems from the soft but highly tough characteristic of silk fibroin.

However, as shown in Figure 3.13, the dimensional consistency of short folded silk particles (Type A) is extremely low, which indicates that it is hard to achieve effective chip breaking on silk fibroin by simply changing processing parameters.

In addition, in order to further investigate the effect of cutting speed on the chip breakability, the experiments of set V were carried out with a cutting speed of 1.35 m/s and a feed rate of 2.5 μm/rev. The obtained chip morphology is illustrated in Figure 3.14.

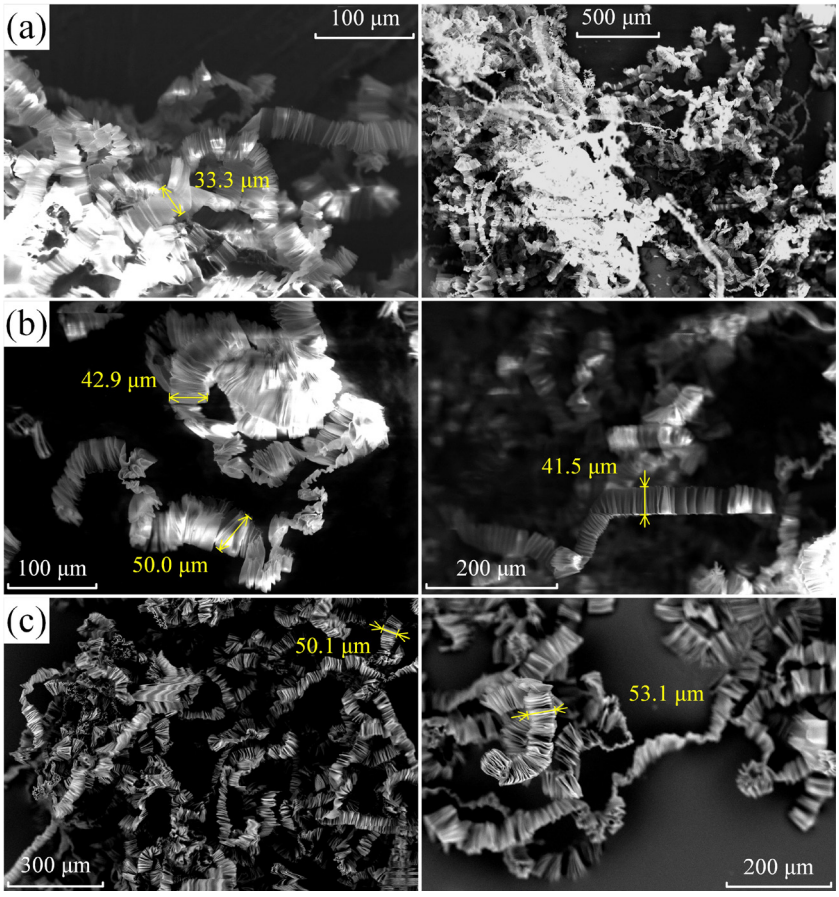

Figure 3.14 Chip morphology in set V with a cutting speed of 1.35 m/s and a feed rate of 2.5 µm/rev: (a) depth of cut d_c = 1 µm; (b) depth of cut d_c = 1.5 µm; (c) depth of cut d_c = 2 µm.

It can be observed from Figure 3.14 that, at a lower cutting speed of 1.35m/s, long folded particles (Type B) instead of short and discontinuous ones (Type A) were manufactured in all machining trials under different depths of cut, despite a feed rate of 2.5 µm/rev. It is determined that low cutting speed creates continuous chips, whereas high cutting speed increases the chip breakability of silk fibroin (see Figure 3.13). This phenomenon is consistent with similar research on steel [37,43].

3.4 Summary

This chapter investigated the machinability of silk fibroin in diamond turning through cutting experiments from the aspects of the specific cutting force and chip morphology. The research results indicated that the ductile mode cutting of silk fibroin was achieved. Long helical, ribbon, folded or even short and discontinuous silk particles were successfully fabricated. The cutting experiments, therefore, verify the feasibility of manufacturing silk particles with different geometries using diamond turning. The conclusions can be drawn as follows:

(1) An increase in the cutting speed can reduce the specific cutting force as a result of material softening. Meanwhile, a reduction in the depth of cut can increase the specific cutting force due to the size effect.

(2) Long helical silk particles with a tunable radius of curvature R were manufactured using a sharp point tool with a feed rate of less than 2.5 μm/rev. A reduced feed rate can decrease the radius of curvature of the helical particles. Long ribbon particles were manufactured using a round nose tool. The folding wavelength λ_f of the ribbon particles can be tailored by tuning the cutting speed and depth of cut. An increase in the cutting speed and a reduction in the depth of cut can decrease the folding wavelength.

(3) A chip chart for diamond turning of silk fibroin was created with three types of particles (e.g. long ribbon, long folded and short folded). The chip chart shows that the breakability of silk chips increases at a reduced feed rate and depth of cut. This tendency is opposite to that commonly observed on metallic materials (e.g. hardened and stainless steels) due to the soft but highly tough property of silk fibroin. Short and discontinuous folded particles were also manufactured. A higher cutting speed (i.e. over 2.7 m/s) is preferred for manufacturing this kind of particle.

However, it is hard to increase the chip-breaking efficiency by simply changing the processing parameters due to the ductile nature of silk fibroin. Therefore, elliptical vibration diamond turning will be studied in the following chapters as an effective chip breaking technique to obtain filamentous silk particles.

Chapter 4

Investigation of chip formation mechanism in diamond turning of silk fibroin

4.1 Introduction

This chapter establishes a hybrid FE-SPH orthogonal cutting model to investigate the chip formation mechanism in diamond turning of silk fibroin. First, the material parameters of silk fibroin in Cowper-Symonds material model are preliminarily determined. Then, the effectiveness of the hybrid FE-SPH cutting model and the determined material parameters of silk fibroin is verified. Finally, the formation mechanism of shear bands and serrated chips in diamond turning of silk fibroin is revealed for the first time. Its link with the hierarchical structure of silk fibroin is also identified.

4.2 Hybrid FE-SPH modelling

4.2.1 Hybrid FE-SPH scheme

SPH method can easily handle the large-deformation processes because the workpiece comprises a group of discrete particles that carry the material properties and state variables. Therefore, the mesh tangling and distortion involving the large strain rate and extreme loading can be avoided. Another advantage of SPH is the natural chip/workpiece separation [73]. There is no need to introduce the chip separation criterion (as required in Lagrangian approach) or a pre-defined cutting path to enable the chip/workpiece separation. Unlike Eulerian approach, the free face generation is

entirely manipulated by SPH technique [153]. Unfortunately, the SPH technique lacks computational efficiency than FEM [158]. Therefore, a hybrid numerical model based on FE and SPH schemes is adopted to simulate diamond turning of silk fibroin. The mesh-free SPH technique is used in the large-deformation zone that is subject to extreme strain and strain rate. The rest of the workpiece is modelled using the mesh-based FEM to reduce the computing cost [94]. However, the default SPH formulation cannot manage the accurate particle distributions on the boundaries for the lack of neighbours [87]. Thus, the renormalized SPH formulation is employed in this model to overcome this problem.

4.2.2 Static material parameters

The elastoplastic material model with isotropic/kinematic hardening plasticity was employed to describe the dynamic behaviour of silk fibroin. The stress-strain curve of this model consists of two linear stages (i.e. elastic stage and plastic stage) [114]. Diamond turning delivers a high strain rate in the order of 10^6 s^{-1} for a cutting speed over 1 m/s [156]. Hence, Cowper-Symonds material model that scales the quasi-static yield stress with a factor related to the effective strain rate was adopted [92,117].

According to the reference [6], Young's modulus of the regenerated silk fibroin ranges from 1 GPa to 6.5 GPa, and its tensile strength varies from 7 MPa to 100 MPa. As a natural protein material produced by silkworms, the actual Young's modulus and tensile strength of silk fibroin differ from batch to batch. Thus, it is not easy to confirm their uniform values that are applicable in all cases. Nevertheless, for ease of manipulation, Young's modulus was preliminarily selected as 5.2 GPa after summarising the available references [159–161]. Likewise, the static yield stress was

set as 70 MPa, which is 70% of the maximum tensile strength. E_{TAN} is the tangent modulus which is the slope of the stress-strain curve at the plastic stage. In general, the tangent modulus equals a few percentages of the material's Young's modulus [115,116]. This ratio was currently chosen to be about 3.3%. In this work, the material parameter β of Cowper-Symonds model was set as 0, considering the large shear deformation in diamond turning [114]. In summary, the static material parameters of silk fibroin are given in Table 4.1.

Table 4.1 Static material parameters of silk fibroin.

Parameters	Values
Density (g/cm^3)	1.4
Young's modulus (GPa)	5.2
Poisson's ratio	0.3
Static yield stress (MPa)	70
Tangent modulus (MPa)	172.4

4.2.3 Orthogonal cutting model for diamond turning

In this work, the non-overlapping diamond turning process of silk fibroin is assumed to be an orthogonal cutting process. Moreover, the cutting experiments were carried out at relatively low cutting speeds to minimize the thermal effects on the work material. Thus, the temperature effects on the material properties were neglected to simplify the theoretical treatment [162].

A 3D workpiece with the size of 30 μm × 20 μm × 1.6 μm was modelled in an orthogonal cutting framework using LS-PrePost which is a superior pre/post processor that is fulfilled by LS-DYNA. Figure 4.1 shows the proposed hybrid FE-SPH numerical model.

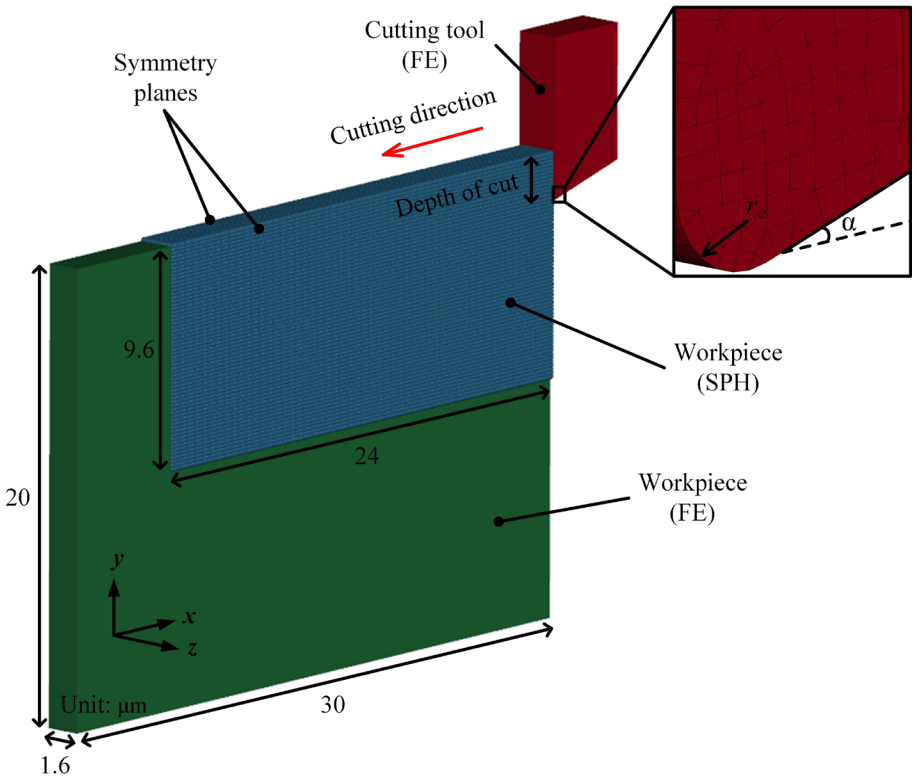

Figure 4.1 Hybrid FE-SPH numerical model for diamond turning.

The workpiece was split into two domains: one representing the SPH (24 μm × 9.6 μm × 1.6 μm) domain and the rest representing the FE domain. The default eight-node Lagrangian solid elements were used for the FE region of the cutting tool and workpiece. Meanwhile, the renormalized formulation was employed for the SPH domain. After the sensitivity analysis on the particle density, the total number of the SPH particles was determined to be 101,321. The minimum mesh size for the continuum FE domain was 0.4 μm. Two symmetry planes were deployed on the front and back faces of the SPH domain to generate ghost particles for maintaining the kernel compactness [163]. In addition, the fixed boundary condition was applied on the left-hand and bottom faces of the workpiece. At the FE-SPH interface, the Lagrangian meshes and SPH particles were coupled by a tied contact formulation. The

good continuity of von Mises stress along paths through the tied interfaces verified the effectiveness of this treatment. The stress changed continuously and smoothly without any large-scale fluctuation.

The tool rake angle was 0˚, and the clearance angle α was 15˚, which were the same as those in the experiments. The tool edge radius r_e was set at 60 nm, and the meshes near which were refined for better computing accuracy. The density of the diamond tool is 3.5 g/cm^3 with a Young's modulus of 1050 GPa. The Poisson's ratio of the diamond tool is 0.1. Considering the limited computational resources, the time scaling technique was applied to reduce the computing time, which has been proved as a reasonable assumption [39]. Thus, the cutting speed was set to be 6.75 m/s, which was five times higher than those in actual experiments. The termination time for all the numerical simulations was 2.2 μs. The Coulomb friction law was introduced to describe the tool/workpiece friction with a coefficient of 0.12 [158].

4.3 Determination of Cowper-Symonds material parameters

The Cowper-Symonds model was employed to describe the damage behaviour of silk fibroin in diamond turning. There are two material parameters in Cowper-Symonds equation, D and p, which artificially increase the yield strength under high strain-rate loading. Therefore, the required cutting energy is increased. Considering that there is no Cowper-Symonds material parameter available for silk fibroin yet, the parameter p is preliminarily set as 5, 7 and 10, based on available settings [164–166]. The parameter D ranges from 0.1 to 6500. In this series of numerical simulations, the depth of cut was 2 μm.

The simulated specific cutting forces with different Cowper-Symonds material parameters are shown in Figure 4.2. It is easy to conclude that a smaller value of the parameters p can drastically increase the specific cutting force. This is because a smaller parameter p will lead to a higher scale factor for the yield limit, increasing the critical stress and required cutting energy. However, it does not mean its value can be decreased unreasonably, as the parameter p also significantly influences the chip morphology.

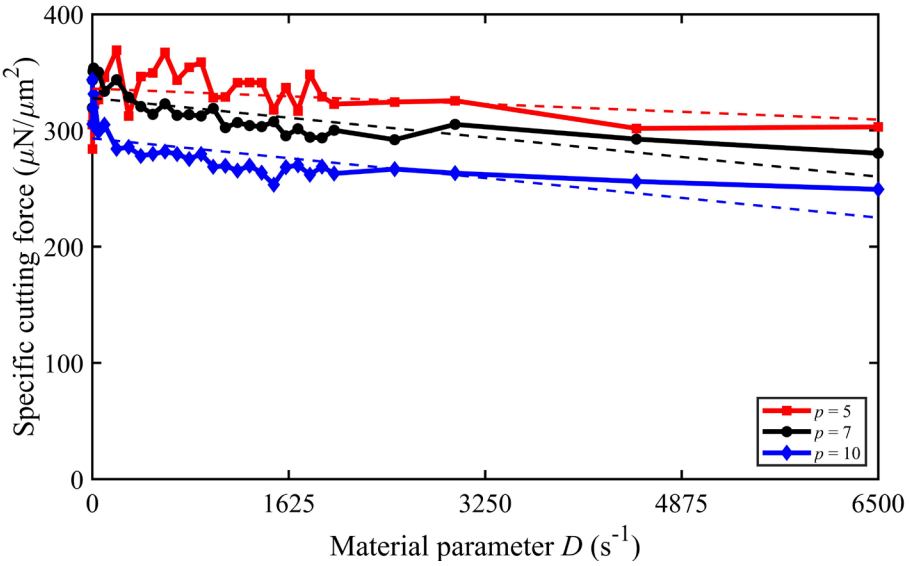

Figure 4.2 Simulated specific cutting forces with different material parameters.

The simulation results on chip morphology for various parameter p with fixed parameter D at 1100 s^{-1} are shown in Figure 4.3.

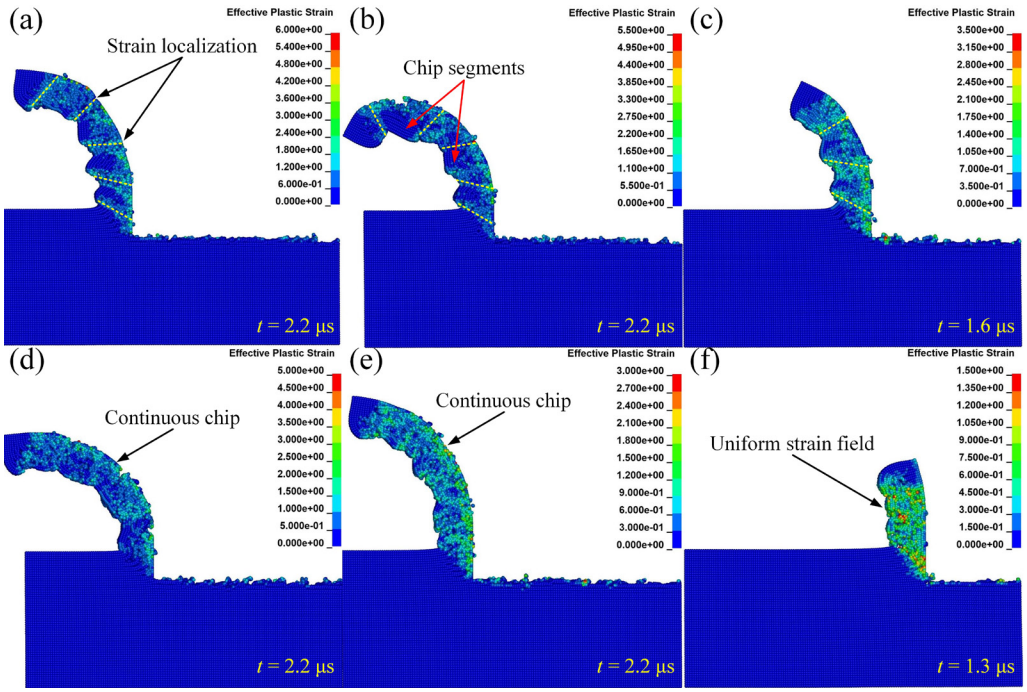

Figure 4.3 Simulated chip morphology: (a) $p = 10$; (b) $p = 7$; (c) $p = 6.5$; (d) $p = 6$; (e) $p = 5.5$ and (f) $p = 5$.

When the parameter p is higher than 6.5, the serrated chips with high shear localization and segments are formed, which agrees well with the experiments. However, as the parameter p decreases, the strain field in the chips evolves from shear-localized to uniform. Moreover, the numerical instability of the simulation increases significantly. For instance, the numerical simulations collapse without reaching the termination when parameter p equals 6.5 and 5. At the same time, this instability manifests as the drastic fluctuation of the specific cutting force. As shown in Figure 4.2, the specific cutting force's fluctuation for the material with $p = 5$ is much larger than those with $p = 7$ and 10. Thus, in this study, parameter p is fixed at 7 to balance the specific cutting force and chip morphology.

The parameter D has a similar impact on the cutting force as parameter p does. Figure 4.2 also illustrates that the specific cutting force decreases with the increase of

parameter D. This reduction is owing to a smaller scale factor for the yield strength, although the decline effect of parameter D is not as significant as that of parameter p. But, on the contrary, parameter D exerts a prominent influence on chip shape and material cracking. The simulated chip morphology for various parameter D with parameter p of 7 is illustrated in Figure 4.4.

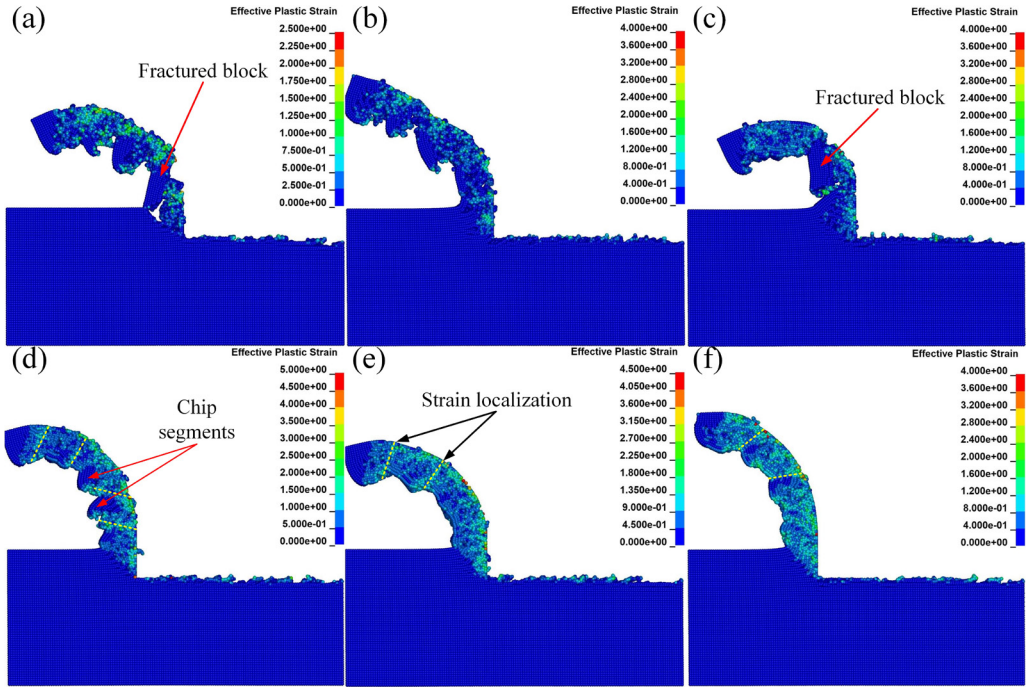

Figure 4.4 Simulated chip morphology: (a) D = 1 s^{-1}; (b) D = 10 s^{-1}; (c) D = 500 s^{-1}; (d) D = 1140 s^{-1}; (e) D = 2000 s^{-1} and (f) D = 4500 s^{-1}.

The fractured block chips are generated when parameter D is relatively low (e.g. less than 500 s^{-1}), which indicates that a decrease in parameter D can increase the brittleness of the material and accelerates its cracking process. This phenomenon is contrary to the experimental results. As illustrated in Figure 4.4, the serrated chips with shear localization were obtained in cutting trials. Furthermore, parameter D also affects the chip morphology and shear band spacing, as the shear localization phenomenon is weakened by increasing parameter D.

In summary, the material with $p = 7$ and $D = 1140$ s^{-1} can obtain a good prediction in terms of shear band spacing and specific cutting force. Therefore, the Cowper-Symonds material parameters for silk fibroin are characterized. The effectiveness of the hybrid FE-SPH model will be discussed in the following section. The accuracy of the determined Cowper-Symonds parameters will be evaluated as well.

4.4 Model evaluation and verification

To evaluate and verify the model established, the simulated chip morphology with and without Cowper-Symonds material model are compared in Figure 4.5.

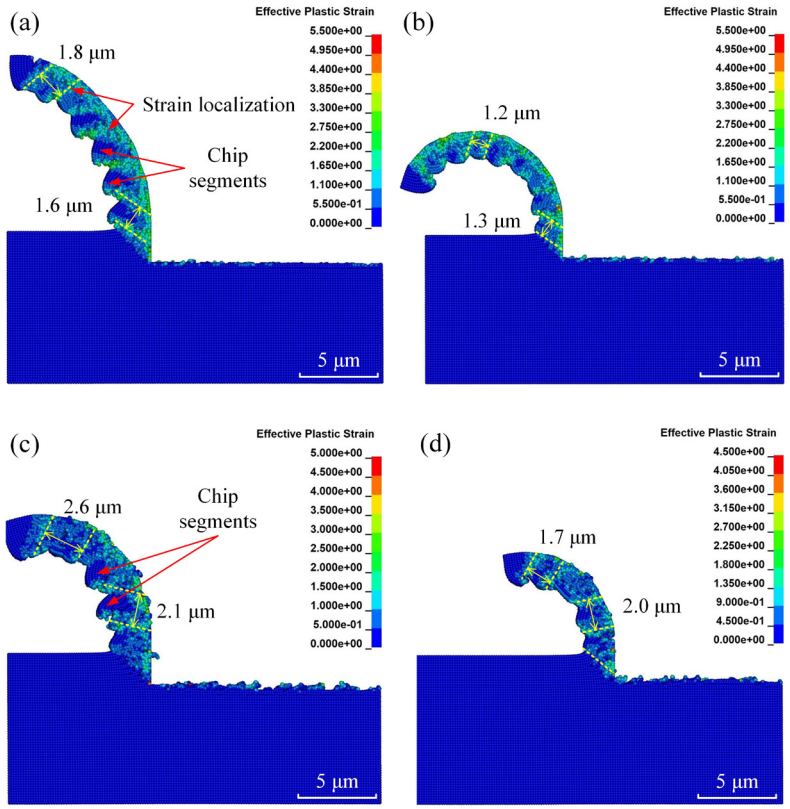

Figure 4.5 Simulated chip morphology: (a) without Cowper-Symonds model (depth of cut $d_c = 2$ µm); (b) without Cowper-Symonds model (depth of cut $d_c = 1.5$ µm); (c) $p = 7$; $D = 1140$ s^{-1} (depth of cut $d_c = 2$ µm); (d) $p = 7$; $D = 1140$ s^{-1} (depth of cut $d_c = 1.5$ µm).

The shear strain localization and chip segmentation on the free surfaces can be identified in all the simulated chips, which is consistent with the experimental results in Figure 3.5. The approximate shear band spacing in experiments with a depth of cut of 2 μm is 2.4 μm. In addition, the measured shear band spacing with a depth of cut of 1.5 μm is about 2.1 μm. However, the simulated shear band spacing without introducing Cowper-Symonds model is much smaller than that in the experiments. In such case, as shown in Figure 4.5 (a) and (b), the shear band spacings for a depth of cut of 2 μm and 1.5 μm are generally less than 1.8 μm and 1.3 μm, respectively. In contrast, with the aid of Cowper-Symonds model (p = 7; D = 1140 s^{-1}), the shear band spacing increases significantly. They approach higher than 2.1 μm and 1.7 μm for a depth of cut of 2 μm and 1.5 μm, respectively, which is in good agreement with the measured results.

After introducing Cowper-Symonds model, a better estimation of the specific cutting force was achieved. Figure 4.6 compares the simulated (i.e. with and without Cowper-Symonds model) and measured specific cutting forces.

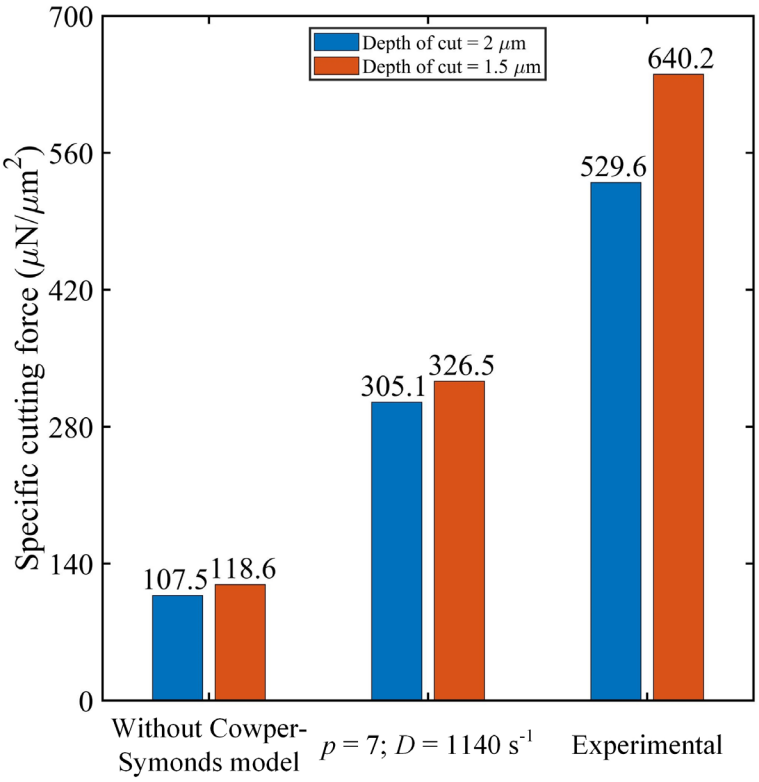

Figure 4.6 Simulated specific cutting forces comparisons.

For instance, when the depth of cut is 2 μm, the specific cutting force obtained from the numerical simulation without considering the strain rate effect is 107.5 μN/μm^2, which is only one-fifth of the experimental result. A similar underestimation can also be observed when the depth of cut is 1.5 μm. However, when the determined Cowper-Symonds parameters are adopted, namely p = 7 and D = 1140 s^{-1}, the specific cutting force with the depth of cut of 2 μm reaches 305.1 μN/μm^2, which is 57.6% of the experimental value. Moreover, when the depth of cut is 1.5 μm, the specific cutting force is 326.5 μN/μm^2, which is 51.0% of the measured result. The estimation difference is because only the strain rate hardening effect is considered in this numerical model, while the strain hardening and thermal effects are ignored. Overall, the effectiveness of the established hybrid FE-SPH model and the accuracy of the

determined Cowper-Symonds material parameters for silk fibroin are verified considering the good prediction regarding the specific cutting force and chip morphology. Therefore, in this chapter, all the simulations will be conducted using the established hybrid FE-SPH model with the determined Cowper-Symonds material parameters.

4.5 Serrated chip formation mechanism

4.5.1 von Mises stress and plastic strain

As an equivalent stress, von Mises stress can be applied to describe the evolution of the inner stress of silk fibroin during the chip formation process. The simulated evolution of von Mises stress and the distribution of effective plastic strain are shown in Figure 4.7 and 4.8, respectively. The cutting speed was 6.75 m/s, and the depth of cut was 2 μm.

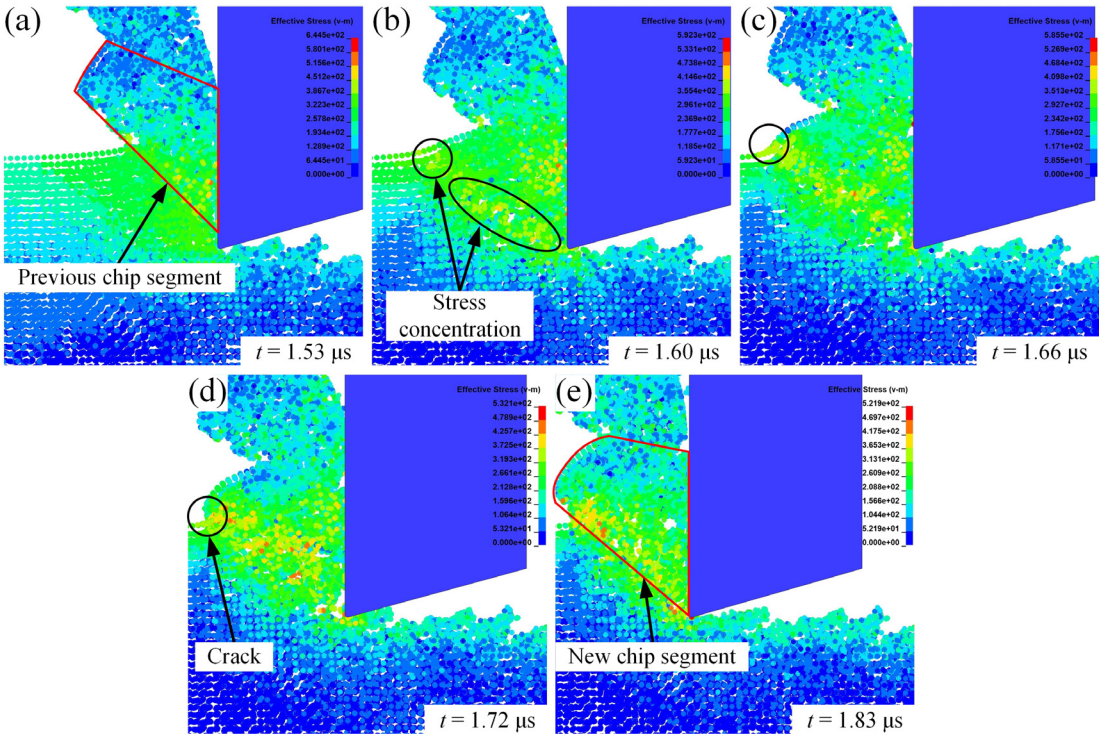

Figure 4.7 Evolution of von Mises stress (unit: MPa): (a) the beginning of a new formation cycle of the chip segment; (b) the von Mises stress concentrates at the tool tip and on the free surface; (c) the crack starts to initiate on the free surface; (d) the crack grows; (e) a new chip segment is formed.

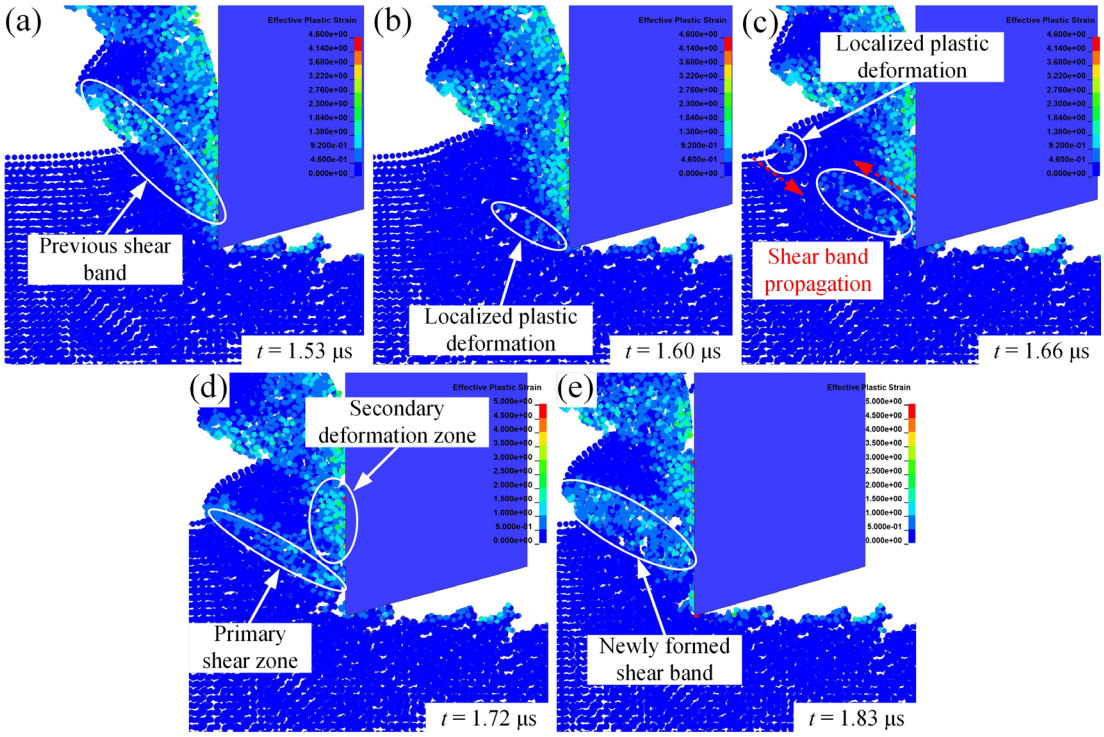

Figure 4.8 Evolution of effective plastic strain: (a) the start of a new cycle of shear band formation; (b) formation of the first part of the shear band; (c) formation of the second part of the shear band and shear band propagation; (d) recognition of the primary and secondary deformation zones; (e) a new shear band is formed.

As shown in Figure 4.7 (a) and 4.8 (a), when the previous shear band is entirely formed, a new shear band is initiated again as the cutting tool advances. Due to the squeezing and shearing action of the cutting tool, von Mises stress concentrates at the tool tip and free surface, as displayed in Figure 4.7 (b). Moreover, the stress contour implies that the concentration of von Mises stress at the tool tip is higher than that on the free surface. When the effective stress exceeds the elastic limit of the silk fibroin, it causes plastic deformation to release the stress. As shown in Figure 4.8 (b), the localized plastic deformation in the form of a shear band initiates in front of the tool tip first and above the cutting edge. At the same time, the maximum effective stress

decreases continuously. Afterwards, another plastic deformation zone forms on the free surface in a relatively small area, as illustrated in Figure 4.8 (c). With the advance of the cutting tool, the first part of the shear band evolves from the cutting edge towards the free surface, whereas the second part propagates from the free surface to the cutting edge. Under the collective efforts of two independent shear bands, an integrated and new shear band is formed by their conjunction.

Moreover, the chip segments are marked in Figure 4.7 (a) and 4.7 (e). A crack on the free surface initiates once the material deformation exceeds the strain limit, and then it propagates towards the tool tip. The chip segment is, therefore, generated. The primary shear zone and secondary deformation zone can also be identified in Figure 4.8 (d) due to the severe material shearing and tool-chip friction.

4.5.2 Underlying mechanism

The formation mechanism of serrated chips in diamond turning of silk fibroin has its roots in the unique hierarchical structure. As illustrated in Figure 4.9, silk fibroin is a protein material that consists of two primary phases: the beta-sheet crystallites and the amorphous matrix. The beta-sheet crystallite is composed of sandwich-structured assemblies connected by interstrand hydrogen bonds (H-bonds) that primarily control the mechanical properties of the silk fibroin [167].

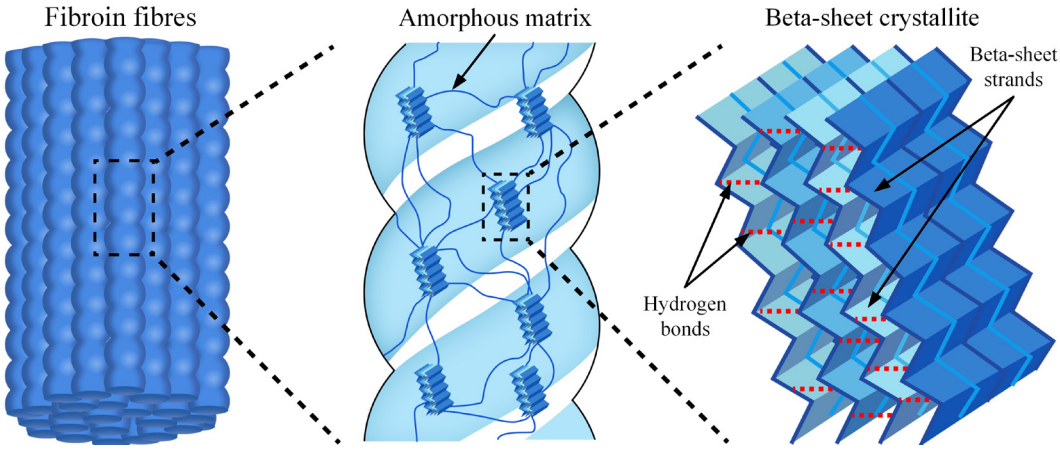

Figure 4.9 The hierarchical structure of silk fibroin.

In analogy to the initiation and propagation of dislocation in ductile metals, the breaking of H-bonds has been recognised as the basic mechanism for failure in silk fibroin [168]. After the initial rupture of H-bonds under high shear deformation, the stick-slip motion occurs as the beta-sheet strand slides [169]. This fracture mechanism has been verified with the aid of experiments and molecular dynamics simulations [27,170]. Therefore, increasing slide motions enable the localized deformation and formation of the shear bands, which results in the serrated chips.

In addition, the simulation results of the oscillation of the specific cutting force and the contour of the effective plastic strain in the cutting process are illustrated in Figure 4.10. The simulation conditions are the same as those in Section 4.5.1.

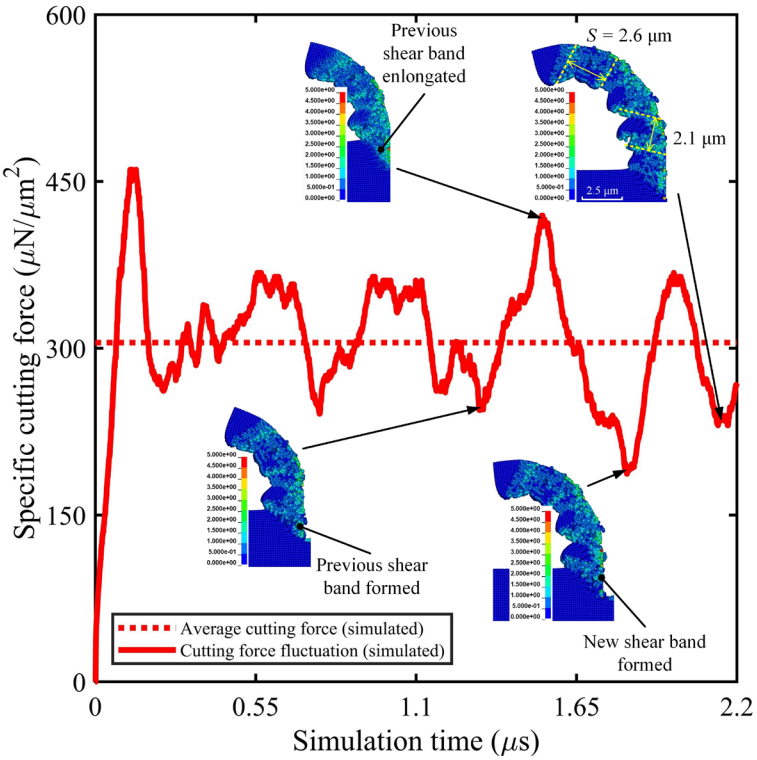

Figure 4.10 Simulated specific cutting force oscillation under a cutting speed of 6.75 m/s and a depth of cut of 2 µm.

The shear deformation is extremely high in diamond turning of silk fibroin. Under the high shear strain in the primary shear zone, a large number of H-bonds are ruptured around the interfaces between beta-strands, thereby forming slip planes and further leading to the interstrand slip motions. Subsequently, accompanying the formation of shear bands, the accumulated slip motions are further developed into shear-governed plastic deformation, which is the principal cause of the formation of serrated chips. After the formation of the previous shear band, the material still undergoes heavy shearing along the narrow primary shear zone, in which the shear band is continuously elongated above the cutting edge. At the same time, the von Mises stress is accumulated around the tool tip, and the elastic energy is stored. Consequently, the cutting force increases and reaches its peak value. Accompanying the emergence and

propagation of a new shear band, the localized plastic deformation releases the accumulated elastic energy. Simultaneously, the cutting force decreases gradually and reaches its lowest value in a single chip formation cycle until the new shear band is completely formed. Afterwards, a new formation cycle for the next shear band and chip segment starts.

In this work, the simulation can only run 2.2 µs due to the limitation of computational power. As the sampling frequency of the data acquisition card for the dynamometer is 250 kHz, it is impossible to compare the oscillation of the measured and simulated specific cutting forces. Nevertheless, the good consistency of the chip morphology obtained in experiments and simulations regarding the shear band spacing *S*, as illustrated in Figure 3.5 and 4.10, can support the proposed serrated chip formation mechanism as mentioned before. Moreover, as shown in Figure 4.11, the lamellar structures on the free surface of the chip generated in the experiments of set I (non-overlapping cutting) provide another evidence of shear localization.

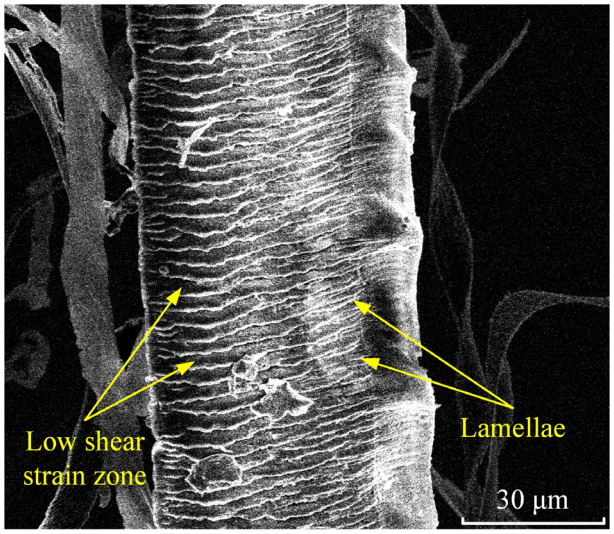

Figure 4.11 Lamellae on the free surface of a silk chip generated with a cutting speed of 1.35 m/s and a depth of cut of 2 µm.

Two areas can be distinguished in SEM images of the chip: a strain localized area and a low deformed area. This plastic field distribution is correctly predicted using the proposed hybrid FE-SPH numerical model.

4.6 Summary

This chapter investigated the serrated chip formation mechanism in diamond turning of silk fibroin through the hybrid FE-SPH numerical simulations. The effectiveness of the established cutting model and the accuracy of the characterized Cowper-Symonds material parameters for silk fibroin are verified in terms of the specific cutting force and chip morphology. The conclusions can be drawn as follows:

(1) The Cowper-Symonds material parameters for silk fibroin were preliminarily determined to be $p = 7$; $D = 1140\ s^{-1}$. The strain rate sensitivity of the silk fibroin was revealed from a diamond turning aspect. A dramatic increase in the predicted specific cutting force can be observed after introducing Cowper-Symonds model. The specific cutting force is three times higher than those without considering the strain rate effect, despite a 49.0% underestimation compared with the experimental value. Nevertheless, compared with the experiments, a good prediction accuracy regarding the chip morphology was also achieved with this set of material parameters.

(2) The proposed hybrid FE-SPH numerical model is able to reveal the formation mechanism of the serrated chip in diamond turning of silk fibroin. The shear band formation is formed through the conjunction of two parts. Specifically, one part propagates from the cutting edge to the free surface, while the other part initiates on the free surface and propagates towards the cutting edge. Furthermore, the chip

segment is formed by the propagation of a microcrack from the free surface to the tool tip.

(3) The serrated chip formation mechanism derives from the hierarchical structure of silk fibroin. Under the high shear strain in diamond turning, the increasing number of ruptured H-bonds enables the interfaces between beta-strands to become slip planes. The accumulated interstrand slip motions further develop into shear bands, which is the dominating cause for the formation of serrated chips.

Chapter 5

Design of a high-frequency non-resonant elliptical vibrator for diamond turning

5.1 Introduction

This chapter concerns designing a non-resonant elliptical vibrator for diamond turning with a high operational frequency for chip breaking.

Firstly, the overall mechanical design of the elliptical vibrator is proposed through mathematical and FE static modelling. A flexure-based design adopting the LSFH and NHPJ is used to combine the reciprocating displacements of the diamond tool into an elliptical trajectory. At the same time, the cross-axis coupling between the tool displacements was mitigated.

Finally, FEA using the mapped meshing method will be performed to determine the key dimensional parameters of the flexure hinges in achieving high operational frequency. In particular, the effect of the neck thickness of NHPJ on the cross-axis coupling and the effect of the thickness of LSFH on the sequence of the vibrational mode shape for the designed elliptical vibrator will be quantitatively analyzed.

5.2 Development of non-resonant elliptical vibrator

5.2.1 Mechanical design

The design goal of this chapter is to design and develop a non-resonant elliptical vibrator that can work at a high frequency of up to 5 kHz with an acceptable cross-axis coupling ratio and thermal power. Figure 5.1 shows the schematic 3D model of the

proposed design, which mainly includes a tool holder and a mounting base. Two high-frequency reciprocating displacements are generated by two piezo actuators after inputting sinusoidal signals with a certain phase angle. The piezo actuators are pre-loaded by two round end screws mounted at the bottom. Moreover, low-capacitance piezo actuators were chosen to get rid of overheating. As mentioned before, the low-stiffness structure of the non-resonant elliptical vibrator limits its operational frequency. In order to improve the structural stiffness of the vibrator and enlarge its operational frequency, two NHPJs and two LSFHs with a cross-layout were adopted in this work, as shown in Figure 5.1.

The NHPJ was designed based on the right circular notch hinges, guiding and transmitting two perpendicular motions to the diamond tool as a high-precision translational pair. More importantly, it can reduce the cross-axis coupling between the two displacements, allowing the diamond tool to move independently in the *y*- and *z*-directions. Figure 5.1 (a) illustrates that the tool cradle works as a holder for the diamond tool and combines two high-frequency reciprocating motions to form an elliptical trajectory. The slide guide on the back of the mounting base can easily adjust the height of the vibrator, so various types of cutting inserts with different tool geometries can be selected and replaced conveniently. The high carbon spring steel 65Mn (equivalent to AISI 1066 and BS 080A67) was chosen as the raw material due to its high yield strength required for long service life under cyclic loading. The mechanical properties of 65Mn are concluded as: density ρ = 7850 kg/m^3, Young's modulus E = 210 GPa, Poisson's ratio v = 0.288. Figure 5.1 (b) shows that this vibrator can be mounted on different diamond turning machines through the tool height

adjustor and connecting base. Considering the space constraints of the diamond turning machine, the overall dimension of this compact design is only 54 mm×46 mm×43 mm.

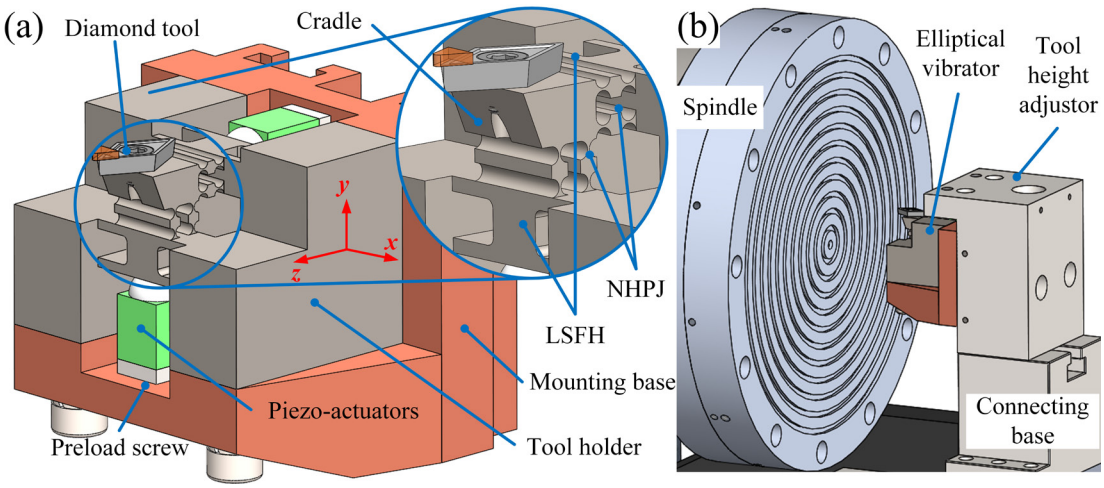

Figure 5.1 (a) Schematic 3D model of the designed non-resonant elliptical vibrator; (b) assembly with a diamond turning machine.

A flowchart is shown in Figure 5.2 to clarify the design process for this non-resonant elliptical vibrator. The whole process mainly consists of static modelling and the determination of key dimensional parameters. After establishing the 3D mechanical structural model of this vibrator, static modelling using the mapped meshing FEA and mathematical method were both adopted. The thickness of LSFH and the neck thickness of NHPJ were determined considering the effects of modal characteristics and cross-axis coupling, respectively.

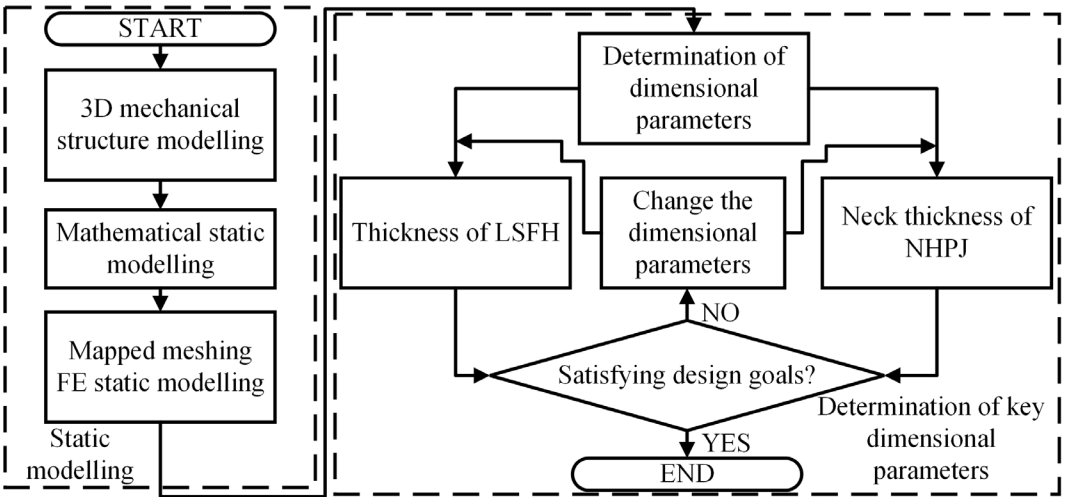

Figure 5.2 Design flowchart for the proposed elliptical vibrator.

5.2.2 Mathematical and FE static modelling

Although the current non-resonant vibrators can control the tool trajectory precisely, the operational frequencies are still significantly lower than their resonant counterparts due to the low structural stiffness. To overcome this shortcoming and mitigate the cross-axis coupling, static modelling using the mathematical method and mapped meshing FEM was performed to guide the determination of key dimensional parameters for the designed vibrator. As shown in Figure 5.3, radius R_n, neck thickness t_n and width b_1 are three critical parameters for NHPJ to determine its structural stiffness.

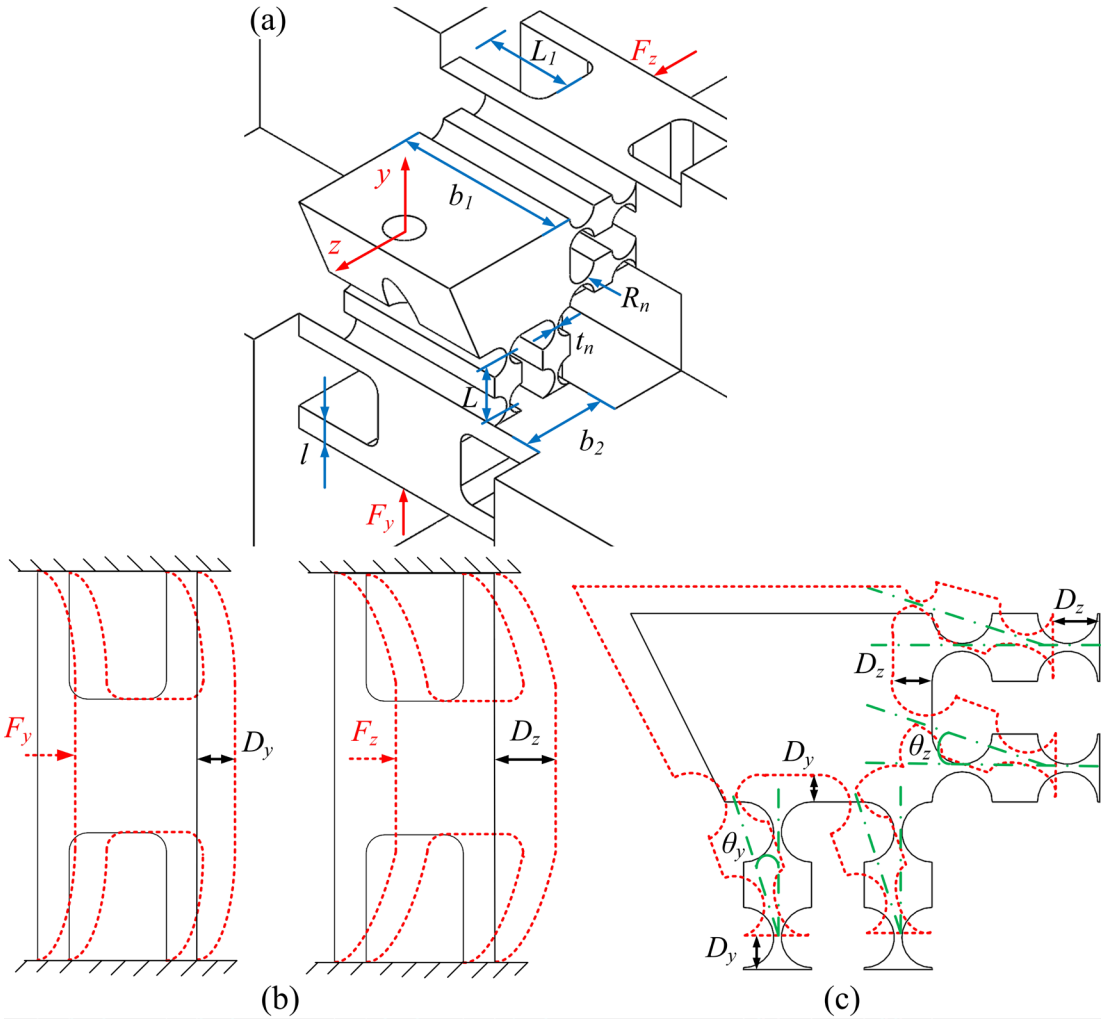

Figure 5.3 Schematic and moving mechanism of the combination of LSFH and NHPJ.

With the consideration of the width of the tool insert, the width b_1 was chosen to be 10 mm to increase the structural stiffness in the direction that is vertical to the tool trajectory plane. The rotary stiffness K_α of the right circular notch hinges of the NHPJ is given by Weisbord and Paros [171]:

$$K_\alpha = \frac{2Eb_1}{9\pi}\sqrt{\frac{{t_n}^5}{R_n}} \tag{5-1}$$

Based on the principle of virtual work, the following equation can be derived:

$$\begin{cases} W_v = \frac{1}{2}F_y D_y + \frac{1}{2}F_z D_z = \frac{1}{2}K_d {D_y}^2 + \frac{1}{2}K_d {D_z}^2 + \Delta U_y + \Delta U_z \\ \Delta U_i = 4\Delta U_f \ (i = y, z) \end{cases} \tag{5-2}$$

where W_v is the virtual work done by actuation forces F_y and F_z. D_y and D_z are linear displacements of the hinges. ΔU_i is the rotational energy of each NHPJ, and ΔU_f is the rotational energy of each notch hinge. K_d is the stiffness of LSFH [172]:

$$K_d = \frac{4E b_2 l^3}{{L_1}^3} \tag{5-3}$$

where b_2, l and L_1 are the width, thickness and length of LSFH, respectively.

The expression for ΔU_f is shown in the following equation:

$$\begin{cases} \Delta U_f = \frac{1}{2}K_\alpha {\theta_i}^2 \\ \theta_i \approx \frac{D_i}{L} \end{cases} (i = y, z) \tag{5-4}$$

where L is the distance between two notch hinges. θ_y and θ_z are angular displacements of the hinges.

The LSFH and NHPJ have identical dimensions in both *y*- and *z*-directions, and the actuation forces F_y and F_z are equal. Thus, the equivalent stiffness of the combination of LSFH and NHPJ in both *y*- and *z*-directions can be derived based on Equation 5-3 and Equation 5-4:

$$K_{eql} = K_d + \frac{4K_\alpha}{L^2} \tag{5-5}$$

Equation 5-5 can be used to estimate the equivalent stiffness of the combination of LSFH and NHPJ.

In addition to the mathematical method, static FE modelling was also conducted using ANSYS 18.0. The bottom surface of the mounting base was set to be fixed support, as shown in Figure 5.4. Since the cutting and thrust forces in elliptical vibration diamond turning are usually in the order of 10^{-1} N [173,174], which are far less than the actuation forces, so they are ignored in the analysis.

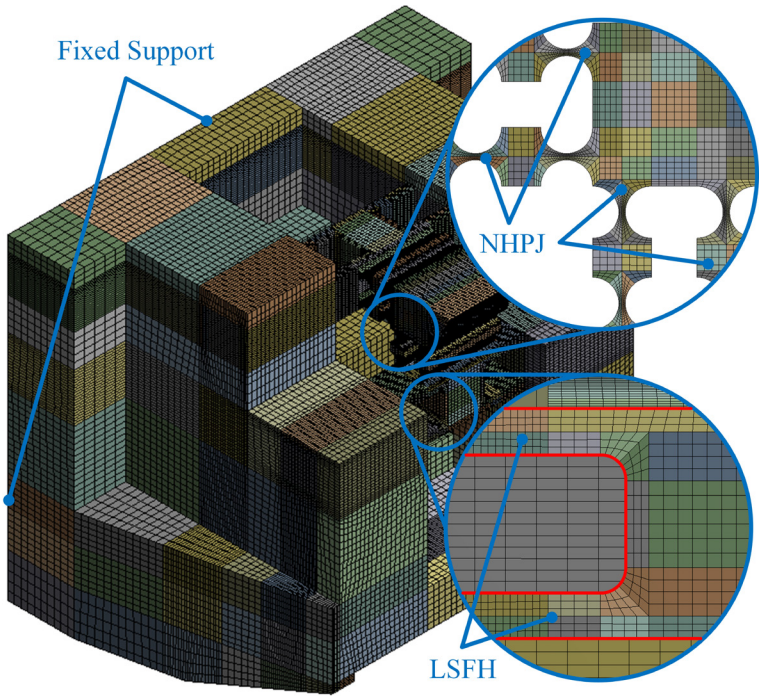

Figure 5.4 FE model of the proposed vibrator using mapped meshing.

Currently, coarse tetrahedral meshes generated by the automatic meshing method are usually used in previous work for modelling the elliptical vibrators [62,175]. Differently, in this work, more regular hexahedron meshes were generated with the aid of the mapped meshing method to increase the modelling accuracy [176–178]. In the following section, the mapped meshing FEA was employed to predict the cross-axis coupling ratio and modal characteristics of the designed vibrator, thereby guiding the determination of the key dimensional parameters.

5.3 Determination of key dimensional parameters

5.3.1 Thickness of LSFH

As a critical dimensional parameter that significantly impacts the equivalent stiffness, the thickness l of LSFH directly determines the modal characteristics of this non-resonant elliptical vibrator, for example, the sequence and vibrational mode shapes of its natural frequencies. In order to finally confirm the dimension of the thickness of LSFH, FE modal analysis was carried out to identify the natural frequency of the designed vibrator. The vibrational mode shapes of the first three natural frequencies are shown in Figure 5.5. In mode shape A, the tool cradle moves along the cutting direction (y-direction). In mode shape B, it moves along the z-direction representing the movement in the depth of cut direction. As for mode shape C, as shown in Figure 5.5 (c), the tool holder undergoes a twisting deformation, which is an undesired mode shape. It is worth pointing out that the sequence of the mode shapes might change with the thicknesses of LSFH.

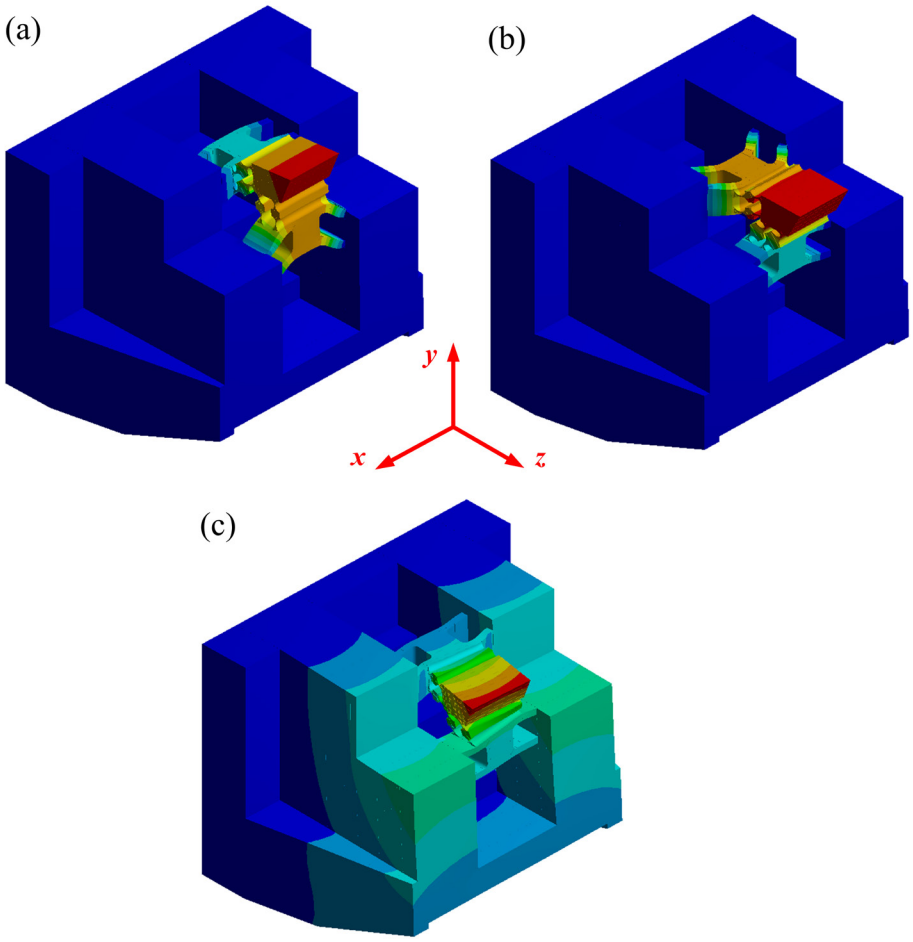

Figure 5.5 The first three vibrational mode shapes of the designed vibrator: (a) mode shape A; (b) mode shape B; (c) mode shape C.

Generally, the first two mode shapes of the vibrator should be coincident with the tool's displacements in the cutting and depth of cut directions. The value of the thickness l should be reasonably selected to make mode shapes A and B be the first two modes of the designed vibrator. Moreover, as the vibration frequencies of the first two modes determine the maximum operational frequency of the vibrator, its natural frequency should be increased to achieve high operational bandwidth. Table 5.1 summarizes the simulation results of the FE modal analysis in terms of sequence and frequencies (Hz) of the first three mode shapes at different thicknesses.

Table 5.1 Simulation results of the FE modal analysis.

Thickness *l* (mm)	Sequence and frequencies (Hz) of the first three mode shapes
1.6	C: 16000; A: 16608; B: 18277
1.5	C: 15947; A: 16103; B: 17382
1.4	A: 15462; C: 15861; B: 16412
1.3	A: 14700; B: 15421; C: 15796
1.2	A: 13846; B: 14379; C: 15715

Mode shape C is the first mode shape when the thickness *l* is 1.6 mm. With the continuous decrease in thickness, mode shapes A and B start to overpass mode shape C gradually, thus becoming the first and the second mode shapes. Nevertheless, the resonant frequency continuously decreases because a smaller thickness would reduce the equivalent stiffness of LSFH, especially in the direction perpendicular to the tool vibration plane. Finally, the thickness of LSFH was confirmed to be 1.3 mm to achieve a higher operational frequency.

5.3.2 Neck thickness of NHPJ

As mentioned before, the cross-axis coupling of two cyclic displacements generated by piezo actuators can have a negative effect on the transmission of the proposed elliptical vibrator and its machining accuracy. Although the neck thickness of NHPJ has less impact on modal characteristics, it has a vital influence on the cross-axis coupling. In this work, the degree of the cross-axis coupling is described using the coupling ratio *C*, whose definition is illustrated in Figure 5.6.

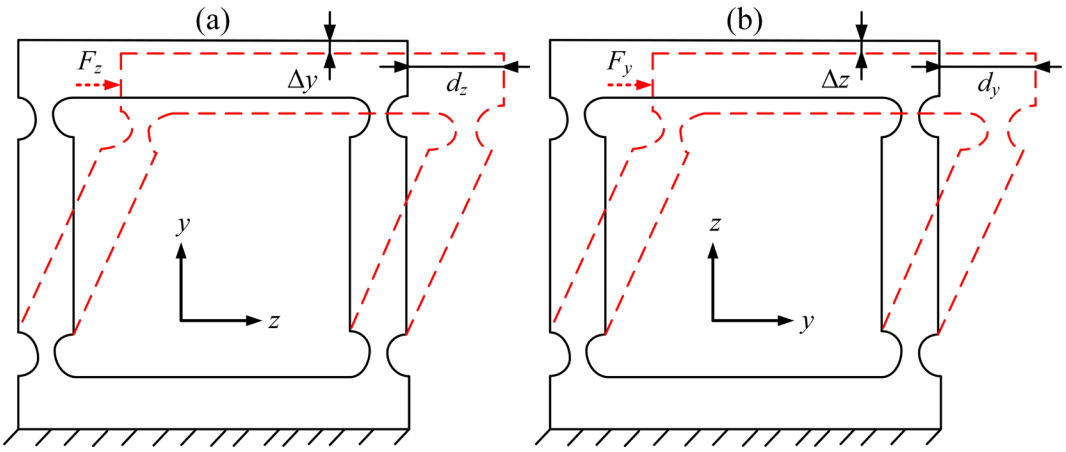

Figure 5.6 Definition of the cross-axis coupling ratio: (a) C_1; (b) C_2.

The cross-axis coupling ratio C_1 and C_2 are defined in the following equations:

$$C_1 = \frac{\Delta y}{d_z} \; and \; C_2 = \frac{\Delta z}{d_y} \tag{5-6}$$

where Δy and Δz are maximum parasitic displacements when the piezo actuator along the z- or y-direction is actuated only. d_y and d_z are maximum output displacements in the y- and z-directions when only one piezo actuator is actuated in the corresponding direction.

The mapped meshing FEA was carried out to determine the neck thickness of NHPJ, which aims to keep the coupling ratio to an acceptable level. In this analysis, the radius of NHPJ was set to be 0.8 mm, considering the attainable machining accuracy when fabricating the prototype. According to the dimensional range in previous research [62,63,175], the value of neck thickness varies from 0.2 mm to 0.35 mm. The results of the calculated cross-axis coupling ratio by the FEA are shown in Figure 5.7.

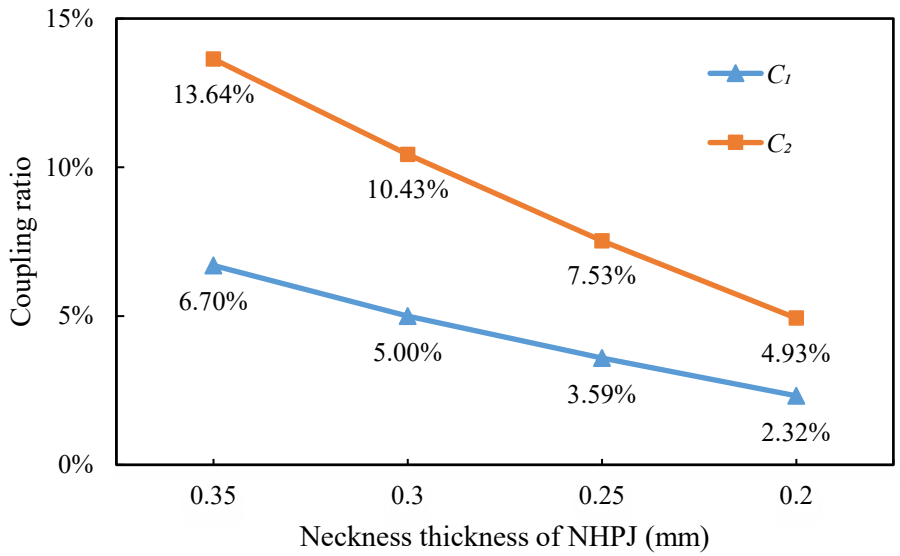

Figure 5.7 Cross-axis coupling ratio under different neck thicknesses.

As the neck thickness of NHPJ continuously decreases, the coupling ratio slumps. The coupling ratio in the cutting direction is two times higher than that in the depth of cut direction. This can be attributed to the beak-shaped tool cradle, which will deteriorate the coupling effect in the cutting direction. When the neck thickness is 0.2 mm, the coupling ratio in the cutting direction decreases to 4.93%. The dimension of the neck thickness t_n is finally confirmed as 0.2 mm, considering the attainable machining accuracy. Several important dimensional parameters of the designed non-resonant elliptical vibrator proposed in this thesis are given in Table 5.2.

Table 5.2 Dimensional parameters of the designed elliptical vibrator.

Parameters	Values (mm)
Radius R_n (NHPJ)	0.8
Neck thickness t_n (NHPJ)	0.2
Width b_1 (NHPJ)	10
Length L (NHPJ)	4.4
Width b_2 (LSFH)	5
Thickness l (LSFH)	1.3
Length L_1 (LSFH)	5.5

The equivalent stiffness of the combination of LSFH and NHPJ in the *z*- and *y*-directions are 52.1 N/μm and 50.9 N/μm, based on the results from the mapped meshing FEA. The small stiffness difference in these two directions can be attributed to the not fully symmetrical configuration of the tool cradle. From Equation 5-5, the equivalent stiffness of the combination of LSFH and NHPJ was calculated as 56.1 N/μm. The relative stiffness differences along the *z*- and *y*-directions are 7.13% and 9.27%, indicating a good consistency between the mathematical and the mapped meshing FE models.

5.4 Fatigue analysis

Fatigue results from the weakening of materials caused by accumulated cracks, especially under cyclic loading. Once a crack has initiated, every loading cycle will grow the crack until a complete failure happens to the mechanical structure. In the practical vibration machining process, the piezo actuators will be subjected to harmonic loading, which easily leads to the failure of the vibrator. In order to ensure a long service life, it is necessary to carry out a fatigue analysis for this vibrator. According to available literature [179], the S-N curve of 65Mn is drawn in Figure 5.8.

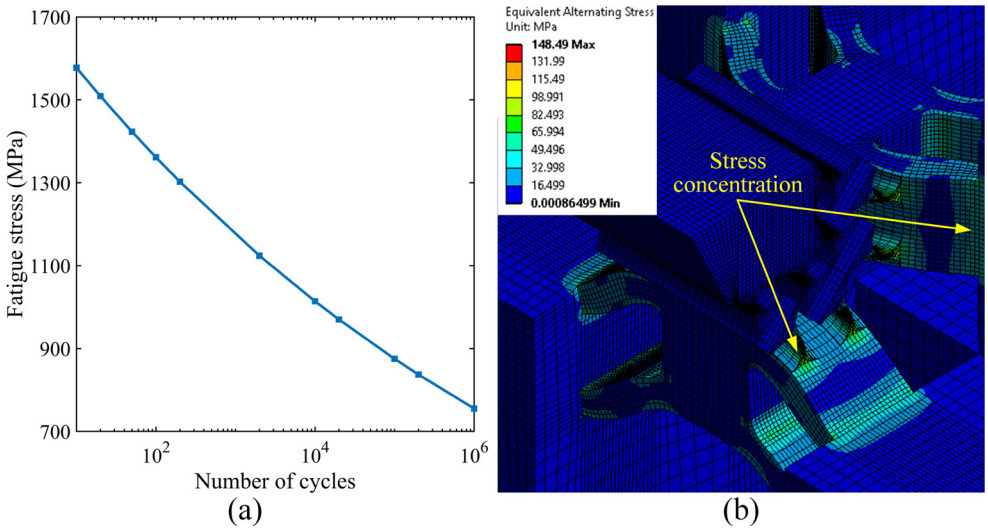

Figure 5.8 (a) S-N curve of 65Mn; (b) simulated distribution of the equivalent alternating stress.

In the life and fatigue analysis, the widely-used Goodman mean stress line [180] is chosen as the conservative model for 65Mn. From the simulation results in Figure 5.8 (b), it can be noted that when the elliptical vibrator is subjected to two cyclic actuation forces of 150 N, the equivalent alternating stress mainly concentrates in the joint between the tool holder and the flexure spring. The maximum value can reach 148.49 MPa, which is still far below the fatigue stress (over 700 MPa, see Figure 5.8) of 65Mn even if the number of cycles is 1 million. Overall, from the above fatigue analysis, it can be concluded that the proposed high-stiffness design can sufficiently ensure a long service life of the proposed elliptical vibrator.

5.5 Simulation of elliptical tool trajectory

The FEA on harmonic response was carried out to predict the tool trajectories of the non-resonant elliptical vibrator. Two external forces with different phase angles were applied to the bottom of LSFH to simulate the actuation forces generated by piezo

actuators in the cutting and depth of cut directions. Figure 5.9 presents the simulation results for the elliptical tool trajectories under different phase angles and operational frequencies. In this case, two fixed actuation forces of 150 N were applied.

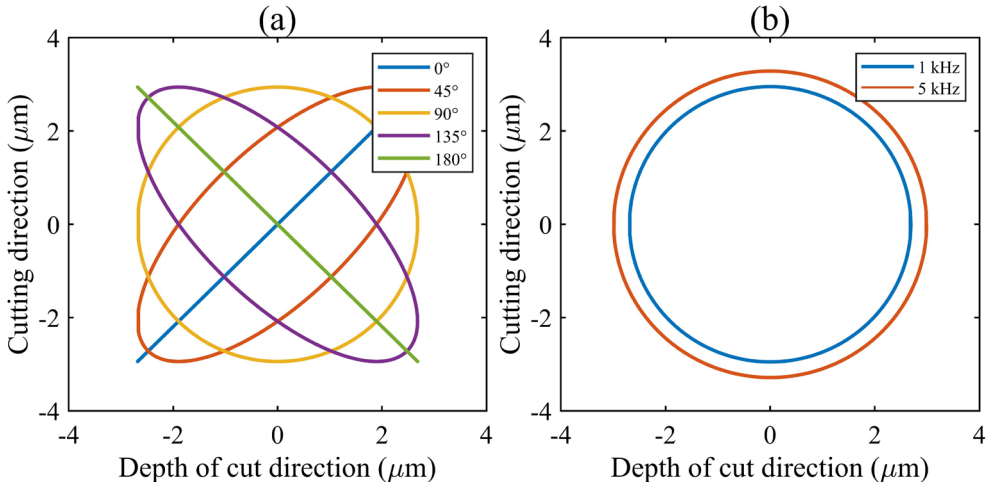

Figure 5.9 Simulated tool trajectories: (a) 500 Hz with various phase angles; (b) 1 kHz and 5 kHz (90° phase angle).

It can be observed that when the phase angle is 90°, the tool trajectory is a regular ellipse. This trajectory tends to undergo an evident change with the phase angle until finally distorting into a straight line with a phase angle of 0° or 180°. Moreover, if the actuation force is kept constant, the amplitude will increase with the operational frequency. The closer to the first natural frequency, the larger amplitude can be obtained, namely the reason for pursuing a higher first natural frequency.

In summary, when two identical actuation forces of 150 N are applied, the theoretical vibration amplitude of this elliptical vibrator can reach over 6 μm under an operational frequency of 500 Hz.

5.6 Summary

A flexure-based high-frequency elliptical vibrator with tunable operational frequency and amplitude was developed in this chapter. The flexure-based design that combines the LSFH and NHPJ can not only transmit and connect the reciprocating displacements of the diamond tool but also offer an improved operational frequency. The results of the FE static modelling indicate that a decrease in the neck thickness t_n of NHPJ can reduce the cross-axis coupling ratio, while a reduction in the thickness l of LSFH can not only reduce the natural frequency of the designed vibrator but also change the sequence of its vibrational mode shapes. Additionally, the simulation results for the tool trajectory also reveal that the proposed vibrator is capable of generating elliptical trajectories with tunable operational frequency and amplitude.

Chapter 6

Performance evaluation test for the high-frequency non-resonant elliptical vibrator

6.1 Introduction

This chapter presents the performance evaluation tests for the elliptical vibrator developed in Chapter 5.

Firstly, the components for the designed elliptical vibrator are manufactured, and its prototype is assembled. Then, a series of experiments are carried out to evaluate the working performance of the designed elliptical vibrator regarding heat generation, modal characteristics, coupling effect and tool trajectory. After that, the cutting accuracy tests through surface texturing are conducted to verify the working stability of the designed vibrator.

Finally, the preliminary machining trials on pure copper are performed to generate discontinuous chips, demonstrating the chip-breaking effectiveness of this elliptical vibrator.

6.2 Prototype assembling

A prototype of the developed elliptical vibrator was manufactured and assembled based on the structural design in Chapter 5. The final assembly of the prototype is shown in Figure 6.1. Two piezo actuators (PSt150, Piezomechanik) are used to generate tool displacements. Before driving the piezo actuators, the high-frequency signals with a certain phase angle are transmitted through the electrodes.

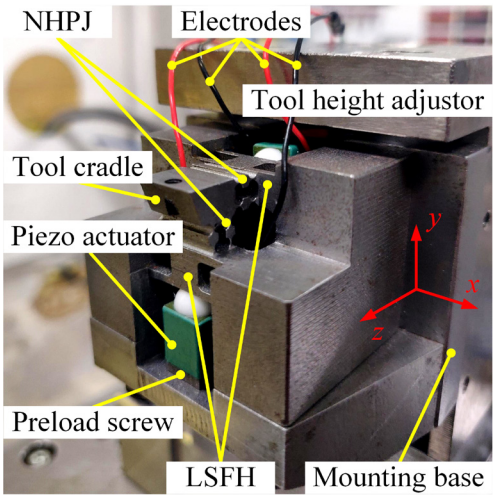

Figure 6.1 Prototype assembly of the designed elliptical vibrator.

6.3 Experimental evaluation on working performance

6.3.1 Experimental setup

The working performance of the proposed elliptical vibrator was evaluated through thermal, dynamic and tool trajectory tests, which will be discussed in the following sections. The experimental setup is shown in Figure 6.2. Two excitation signals were generated by a dual-channel function generator (TGF4042, Aim-TTi). In this process, the low-voltage signals need to be amplified by the power amplifier (E01.A2, Coremorrow) prior to driving the piezo actuators. The displacements of the diamond tool in the cutting and depth of cut directions were captured by two capacitive sensors (Lion Precision CPL190), whose bandwidth is 15 kHz. The measurement results were collected and recorded by a data acquisition card (USB-1608HS, Measurement Computing), and its sampling frequency is 250 kHz.

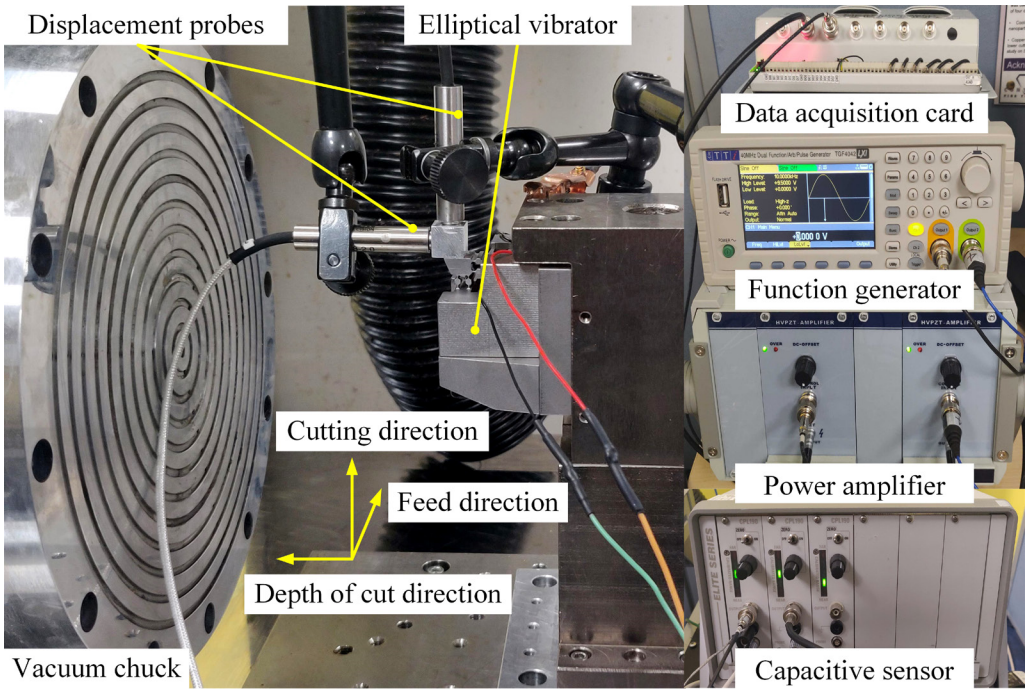

Figure 6.2 Setup for performance evaluation tests.

6.3.2 Analysis of heat generation

Heat and temperature management is a crucial problem and has to be concerned in the first place, as overheating interferes with the performance and reliability of the piezo actuator. A long-term operation under high temperature can even damage the actuator. The heat generation power P_h of each actuator is expressed as follows:

$$P_h = \frac{1}{2} K U^2 C_p f \tag{6-1}$$

where U and f are the peak-to-peak voltage and the frequency of input harmonic signal, respectively. C_p is the capacitance of the piezo actuator, which is 1.8 μF. K is the proportion of the average power consumption converted into heat. Negishi et al. [1, 2] reported that 22% of the electrical power flowing through the actuator was lost

to heat based on the experimental results. In this work, K is chosen as 0.25, considering the extreme condition.

Due to the limited drive capability of the power amplifier, there is a strong negative correlation between the highest operational frequency and the input voltage. Several tests were carried out to investigate the relationships between the highest operational frequency, the heat generation power and the input voltage. The testing results are illustrated in Figure 6.3.

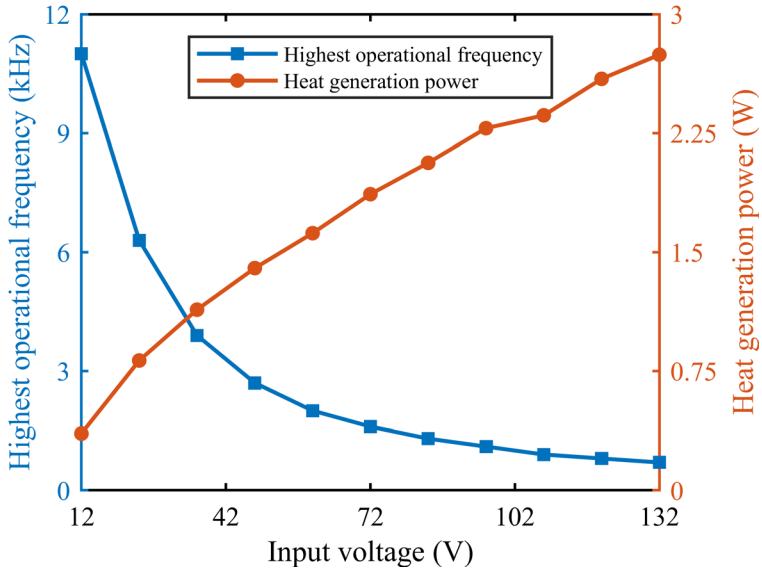

Figure 6.3 Highest operational frequency and heat generation power under different input voltages.

The peak-to-peak voltage of the input signals varies from 12V to 132V instead of 150V to protect the piezo stacks from overstretching. With the increase of input voltage, the heat generation power of the actuators increases and reaches its maximum value when the voltage is 132 V. At this moment, the heat generation power is only 2.74 W, which is competent under an air-cooled working condition.

6.3.3 Experimental modal test

In order to investigate the dynamic response and determine the operational frequency range of the developed vibrator, a series of experimental modal tests were carried out using an impact hammer (PCB Piezotronics 086C03) and several accelerometers (PCB Piezotronics 333B50). The testing results are illustrated in Figure 6.4.

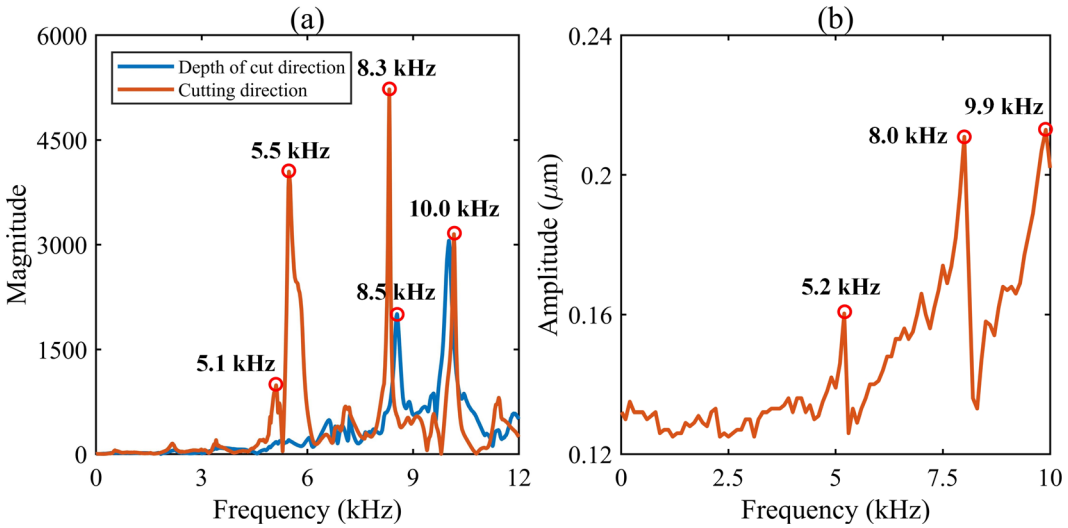

Figure 6.4 (a) Experimental modal tests; (b) frequency response of the designed elliptical vibrator with swept excitation in the cutting direction.

As shown in Figure 6.4 (a), the frequency response of the designed vibrator in the depth of cut and cutting directions are in good agreement in the frequency ranges of below 5 kHz and above 6 kHz, except for two close response peaks at 5.1 kHz and 5.5 kHz. This phenomenon indicates that the first natural frequency of the developed vibrator in the cutting direction is most likely within this frequency range.

To verify this assumption, the frequency sweep tests were conducted. The input voltage for the piezo actuator in the cutting direction was 12 V. The frequency swept from 0 to 10 kHz with an interval of 100 Hz. The amplitude-frequency response is illustrated in Figure 6.4 (b). After comparing Figure 6.4 (a) and (b), it can be found

that the frequency response obtained from the frequency sweep tests is in good agreement with those of the impact hammer modal test. It, therefore, indicates that the first natural frequency of the designed vibrator is 5.2 kHz in the cutting direction. However, its first natural frequency in the depth of cut direction is 8.5 kHz. This difference should be attributed to the imperfect and complicated contact between the actuators, tool holder and mounting base, which seriously decreases the first natural frequency in the cutting direction. It is also worth mentioning that the natural frequency obtained from the FEA is nearly twice higher than those from experiments. In addition to the reason mentioned above, manufacturing errors of the proposed vibrator is another reason for this gap. Nevertheless, the upper limit of the operational frequency for the designed elliptical vibrator was selected as 5 kHz (slightly below its first natural frequency), which is still higher than its non-resonant counterparts in the field of diamond turning.

6.3.4 Evaluation of coupling effect

Two sinusoidal input signals of 500 Hz for both piezo actuators were used to perform the coupling tests at the same voltage of 132 V. Please note that only one actuator was activated in each test, while the other has no input signal. Figure 6.5 compares the displacements of the proposed non-resonant elliptical vibrator in the cutting and depth of cut directions.

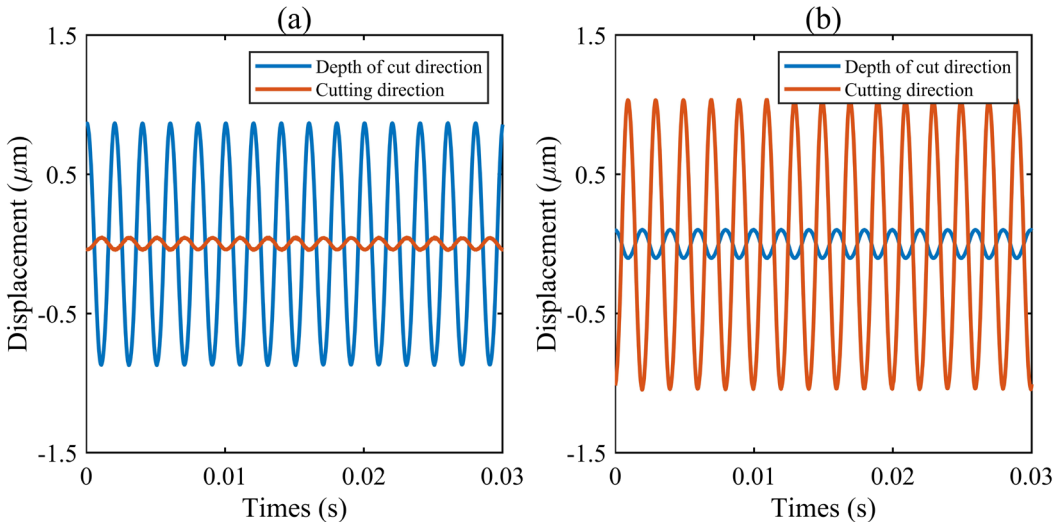

Figure 6.5 Experimental results of the cross-axis coupling: (a) depth of cut direction; (b) cutting direction.

As shown in Figure 6.5 (a), when the actuator along the depth of cut direction was actuated only, the maximum parasitic displacement in the cutting direction was 0.08 μm. In comparison, the maximum displacement in the depth of cut direction was 1.70 μm. Likewise, the results in Figure 6.5 (b) illustrate that when the piezo actuator along the cutting direction was solely driven, the maximum parasitic displacement in the depth of cut direction was 0.20 μm, while the maximum displacement in the cutting direction was 2.05 μm. According to Equation 5-6, it can be calculated that the cross-axis coupling ratios C_1 and C_2 are 4.71% and 9.76%, respectively. The actual cross-axis coupling ratio is twice the results obtained from FEA, but it is very close to the simulation results with a neck thickness of 0.3 mm (see Figure 5.7). The manufacturing error of the developed vibrator should be the major source of the difference. Nevertheless, the cross-axis coupling ratio of the developed vibrator is still at an acceptable level.

6.3.5 Tests on elliptical tool trajectory

Two sinusoidal excitation signals with different phase angles were applied to the piezo actuators. The voltage varied from 24 V to 132 V. Based on the operational frequency range, the tests were carried out with the frequency ranging from 500 Hz to 5 kHz. Notably, due to the limited drive capability of the power amplifier, the voltage of the input signal needs to be tuned according to its input frequency. The displacements of the designed elliptical vibrator in the cutting and depth of cut directions under different input signals were collected and combined. The elliptical tool trajectories of the vibrator under different operational conditions were obtained and shown in Figure 6.6.

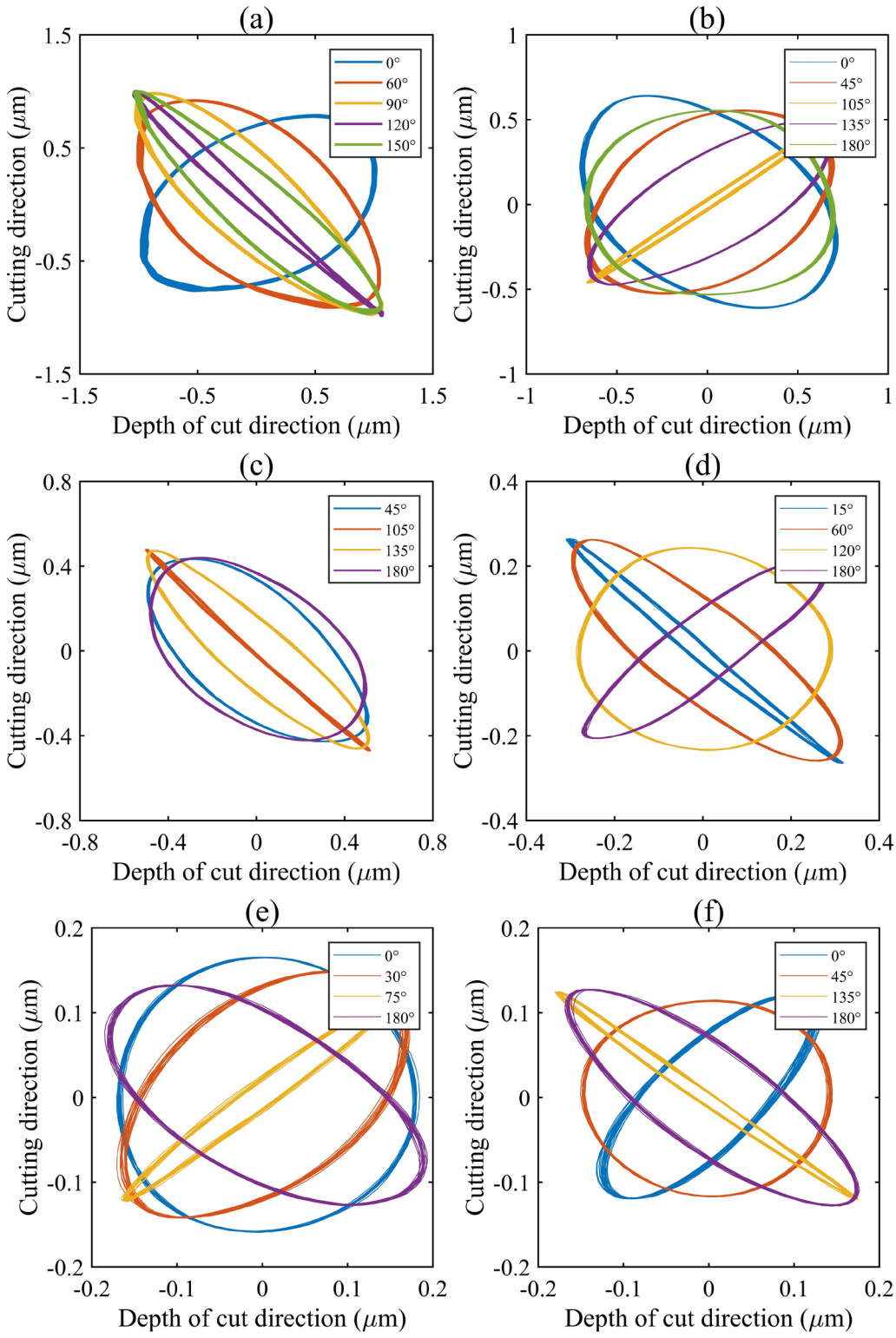

Figure 6.6 Elliptical tool trajectories under different operational conditions: (a) 500 Hz at 132 V; (b) 1 kHz at 96 V; (c) 1.5 kHz at 72 V; (d) 2.5 kHz at 48 V; (e) 4 kHz at 30 V; (f) 5 kHz at 24 V.

Figure 6.6 shows that with the decrease of the input voltage, the tool path dimension b reduced from 1.05 μm to 200 nm. The tool trajectory evolved from a straight line to a regular ellipse with the changing of phase angle. A similar trend appeared under all operational frequencies. Moreover, it can be observed in Figure 6.7 that the relationships between the input voltage and tool path dimensions a and b approximately satisfy two linear functions.

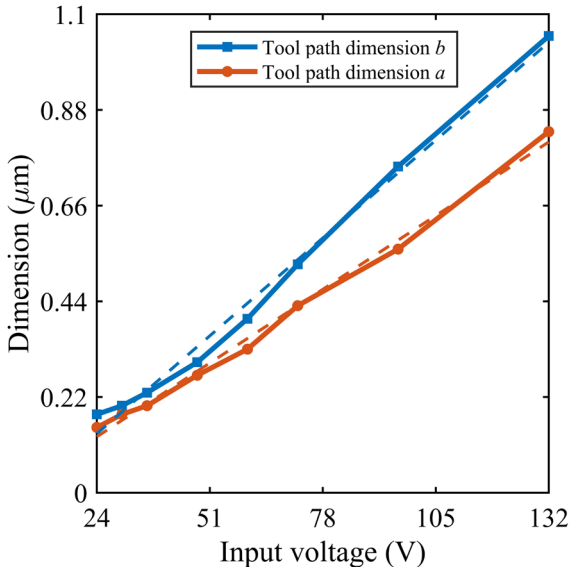

Figure 6.7 Relationship between the input voltage and tool path dimension.

The fitting equations are shown below:

$$a = 0.0063U - 0.0218 \tag{6-2}$$

$$b = 0.0083U - 0.0641 \tag{6-3}$$

where U is the peak-to-peak input voltage (unit: V). a and b are the tool path dimensions (unit: μm) in the cutting and depth of cut direction, respectively. Equation 6-2 and 6-3 can be used to estimate the tool path dimensions according to the input voltages.

Overall, the experimental results approve that a regular elliptical trajectory of the designed vibrator can always be generated under a high frequency of up to 5 kHz.

6.4 Cutting accuracy tests through surface texturing

6.4.1 Principle of surface texturing

The cutting accuracy of the developed elliptical vibrator was evaluated through surface texturing tests. The textured surface can be generated with the aid of tool vibrations. For example, as shown in Figure 6.8, the micro-dimple structures will be obtained when the nominal depth of cut d_n is greater than the tool path dimension b and the HSR is higher than 1. The height h_d of the dimple arrays is equal to the vibration amplitude of the diamond tool in the depth of cut direction, while the wavelength λ_d is equivalent to the upfeed per cycle u.

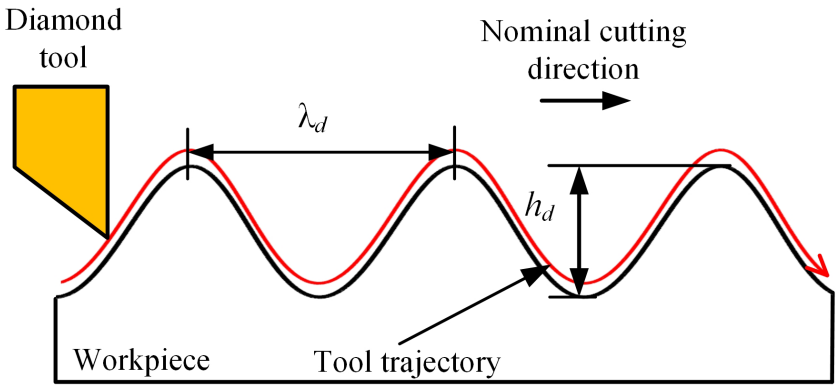

Figure 6.8 Formation principle of the micro-dimple structures.

6.4.2 Cutting conditions

Different operational conditions were employed in the tests, and the detailed parameters are listed in Table 6.1. The nose radius of the diamond tool is 0.5 mm. The tool feed per revolution and spindle speed were set to be 5 mm/min and 30 rev/min,

respectively. The depth of cut was chosen to be 3 μm, thereby ensuring that the nominal depth of cut d_n is larger than the tool path dimension b. After the calculation, the HSR is also greater than 1 in this case. Therefore, as described above, the micro-dimple structures will be manufactured.

Table 6.1 Operational conditions in the machining trials.

Experiment No.	Operational frequency (Hz); input voltage (V)	Cutting diameter (mm)
1	500; 132	20-26
2	1000; 96	13-19

As shown in Figure 6.9, two concentric annuli on the workpiece represent these two machining areas.

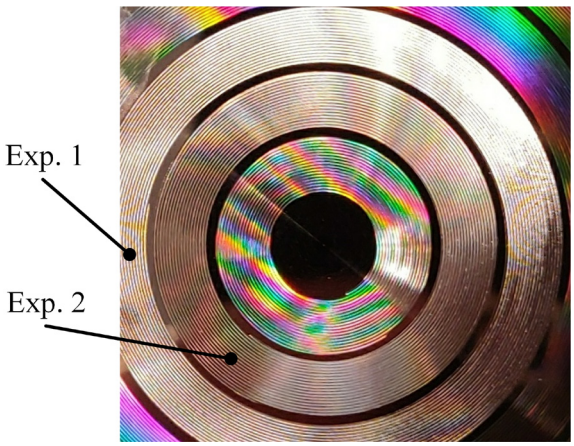

Figure 6.9 Textured surfaces on the copper workpiece.

Two small square areas on the machined surface were selected for measurement by a white light interferometer (Zygo CP300). The distances between the centres of the measurement areas and the workpiece's centre of rotation are 11.1 mm and 7.6 mm, respectively. These two distances are used to estimate the designed values of the wavelength of the machined microstructures in measurement areas.

6.4.3 Results and discussion

Figure 6.10 shows the machined micro-dimple arrays generated under the operational frequencies of 500 Hz (Exp. 1) and 1000 Hz (Exp. 2).

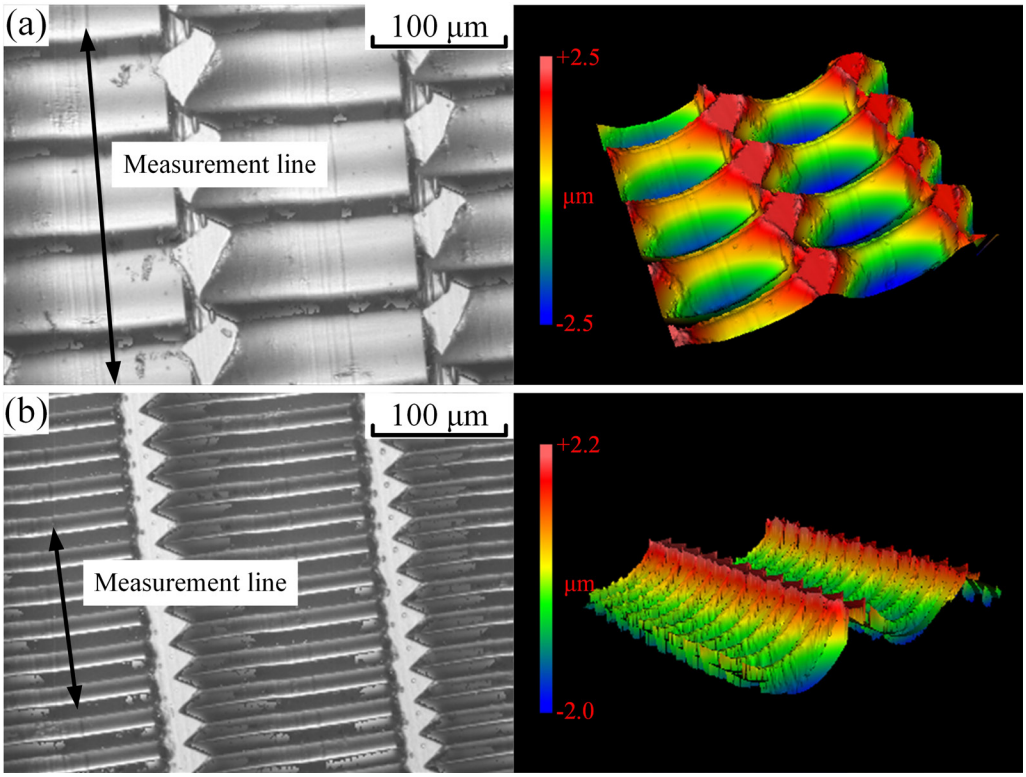

Figure 6.10 Microphotographs and 3D surface topographies of the machined structures: (a) Exp. 1; (b) Exp. 2.

The roughness of the machined surfaces is measured after applying a high-pass filter with a cut-off frequency of 177 Hz to eliminate waviness and form components. The surface roughness *Ra* is 46 nm and 66 nm in Exp. 1 and Exp. 2, respectively. The sectional profiles of the machined structures are illustrated in Figure 6.11. The comparison of the wavelengths and heights between the designed and machined microstructures along measurement lines is shown in Table 6.2.

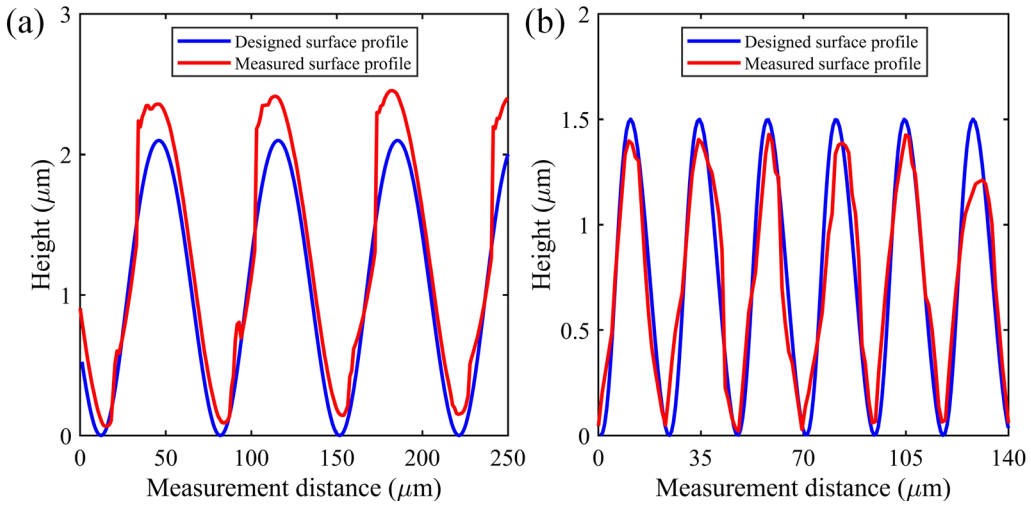

Figure 6.11 Sectional profiles of the machined structures: (a) Exp. 1; (b) Exp. 2.

The measured wavelengths of the machined microstructures agree well with the designed values in both machining trials with errors of -0.86% and -1.26%, demonstrating the excellent frequency stability of the designed vibrator. The measured heights of the machined microstructures are 2.27 μm and 1.34 μm with errors of 0.17 μm and -0.16 μm. The difference is less than 10.67%, showing a good cutting accuracy of the designed elliptical vibrator.

Table 6.2 Dimensional errors of the machined microstructures.

Experiment No.	Dimensions	Designed values (μm)	Measured values (μm)	Errors (%)
1	Wavelength	69.7	69.1	-0.86%
	Height	2.1	2.27	8.10%
2	Wavelength	23.9	23.6	-1.26%
	Height	1.5	1.34	-10.67%

6.5 Preliminary chip-breaking tests

6.5.1 Experimental setup and cutting conditions

The on-machine effectiveness of the proposed non-resonant elliptical vibrator regarding chip breaking was evaluated through elliptical vibration diamond turning experiments. The machining trials were conducted on pure copper. The experimental setup is shown in Figure 6.12. The nose radius of the diamond tool is 0.5 mm. The operational frequency was 500 Hz, and the input voltage was set to be 132 V with a phase angle of 100 degrees. The machining process was captured by a digital microscope (AM4113T, Dino-Lite).

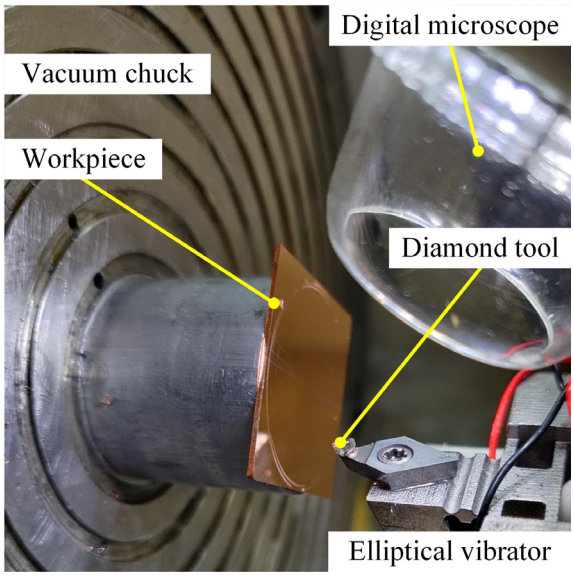

Figure 6.12 Setup for chip-breaking tests on the copper workpiece.

Different cutting conditions were employed, and the detailed parameters are listed in Table 6.3.

Table 6.3 Operational conditions in chip-breaking tests on copper.

Experiment No.	Nominal depth of cut (μm)	Cutting diameter (mm)	HSR
3	1.5	24	0.05; 0.1; 0.5
4	0.5	20	0.05; 0.1; 0.5

6.5.2 Results and discussion

Figure 6.13 illustrates the in-situ chip morphology in Exp. 3 captured by the USB digital microscope. As the nominal depth of cut d_n (1.5 μm) is greater than the tool path dimension b (about 1 μm), the continuous chips were formed in all three tests despite the values of HSR. Differently, with the increase of HSR, the chip morphology evolves from ribbon chip to snarled chip.

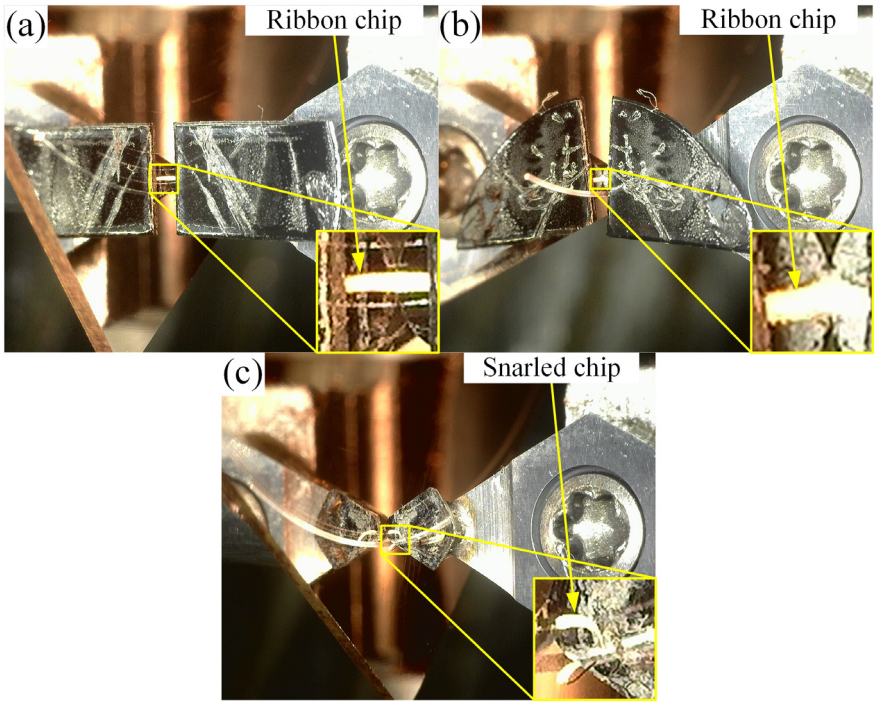

Figure 6.13 Chip morphology in Exp. 3: (a) HSR = 0.05; (b) HSR = 0.1; (c) HSR = 0.5.

The images of the generated continuous chips were captured by an SEM (S3700-N, Hitachi), as illustrated in Figure 6.14.

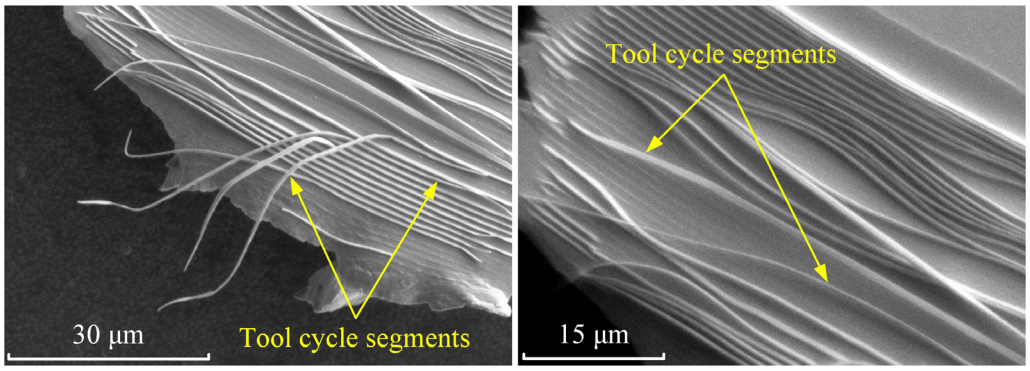

Figure 6.14 SEM images of the continuous chips formed in Exp. 3 (HSR = 0.05).

It can be observed that regularly distributed thin tool cycle segments were formed on the continuous chip, which derives from the intermittent tool/workpiece contact in elliptical vibration diamond turning. This kind of continuous chip is separated on the segments but remains connected at the centre where the maximum chip thickness is reached. The formation principle of the tool cycle segments is shown in Figure 6.15.

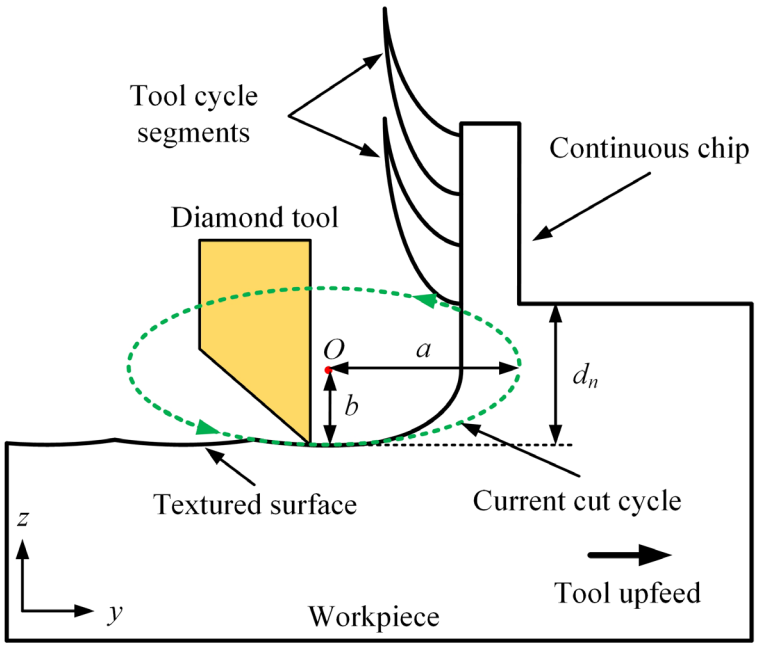

Figure 6.15 Formation principle of tool cycle segments in elliptical vibration diamond turning.

In elliptical vibration diamond turning, due to the periodic vibration of the diamond tool, both the depth of cut and chip thickness are reduced, leading to the intermittent tool/workpiece contact. As a result, discontinuous characteristics are generated on the back surface of the continuous chip with the formation of tool cycle segments.

When the nominal depth of cut d_n is reduced to 0.5 μm (i.e. smaller than b), as shown in Figure 6.16, no ribbon or snarled chips were generated in Exp. 4. Instead, discontinuous chips piled up in front of the tool tip, whose SEM images are illustrated in Figure 6.17. The evident transformation of chip geometry from continuous chips to discontinuous chips verified the effectiveness of this vibrator in enhancing chip-breaking efficiency.

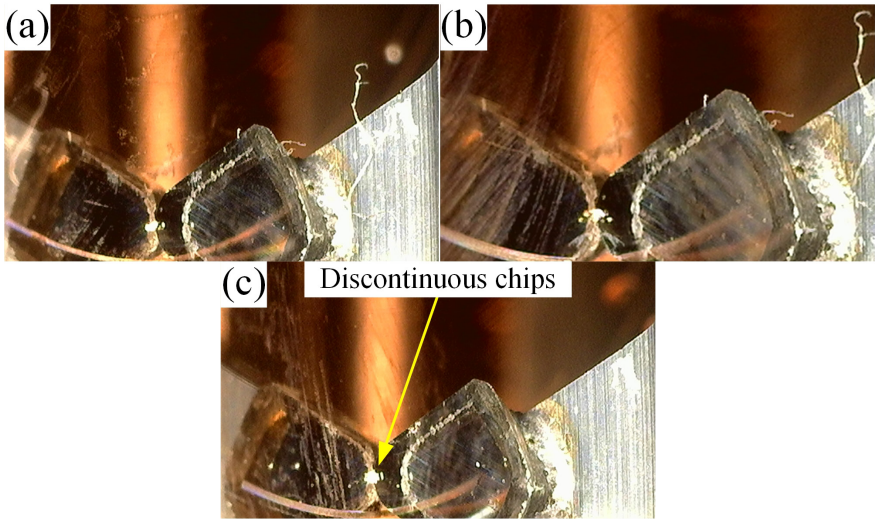

Figure 6.16 Chip morphology in Exp. 4: (a) HSR = 0.05; (b) HSR = 0.1; (c) HSR = 0.5.

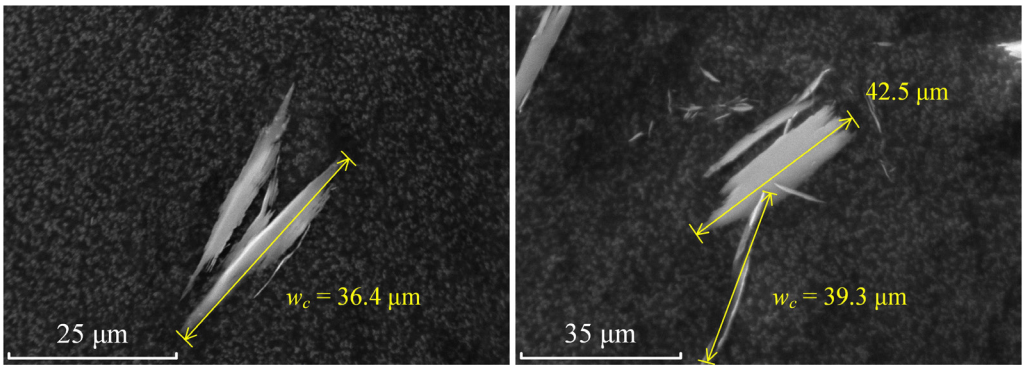

Figure 6.17 SEM images of the discontinuous chips formed in Exp. 4 with an HSR of 0.5.

6.6 Benchmarking with other work

The comparison of the key performance indicators of the proposed vibrator with other published work is shown in Table 6.4.

Table 6.4 Comparison of the key performance indicators with other published work.

Features	This work	Li et al. [181]	Han et al. [62]	Wang et al. [63]
Operational frequency (kHz)	5	2.5	1.8	6
Vibration amplitude (µm)	2	2.5	24	16
Equivalent stiffness (N/µm)	50.9; 52.1	N/A	25	0.4; 1.5
Machined materials	Pure copper	N/A	6061Al	Aluminium alloy
If applicable to diamond turning	Yes	Yes	Yes	No

In summary, the prototype of the elliptical vibrator can work at a high operational frequency of up to 5 kHz. Although higher operational frequency has been achieved by Wang et al. [63], it is not applicable to diamond turning. The equivalent stiffness at the tool tip reaches 50.9 N/µm in the cutting direction and 52.1 N/µm in the depth of

cut direction. The vibration amplitudes can only reach over 2 μm, which is relatively lower than existing designs. The reason for this shortcoming is complicated. First, compared with existing configurations, the high-stiffness property of this vibrator increases its operational frequency but inevitably sacrifices the amplitude outputs. In addition, as mentioned in Section 6.3.4, the dimensional error within the manufacturing process can increase the actual structural stiffness of the designed vibrator. This can severely reduce the effective displacements of piezo actuators. High-performance piezo actuators with high stiffness and high free stroke can be applied in the future to improve this situation.

6.7 Summary

After prototyping the proposed non-resonant elliptical vibrator, a series of experiments, including on-machine elliptical vibration diamond turning trials, were conducted to evaluate its working performance. The conclusions can be drawn as follows:

(1) The systematic experimental evaluation of the proposed vibrator demonstrated that it could achieve a high-frequency and non-resonant working mode with an acceptable cross-axis coupling ratio and thermal generation. Moreover, the elliptical tool trajectory with different amplitudes can be conveniently generated by tuning the operational frequency, input voltage and phase angle.

(2) The prototype of the designed elliptical vibrator can work at an operational frequency of up to 5 kHz, which is higher than its non-resonant counterparts in the field of diamond turning. Its vibration amplitude can reach over 2 μm, although the high-frequency and high-amplitude working modes cannot be achieved

simultaneously due to the limitation of the drive capability of the current power amplifier.

(3) The cutting accuracy of the designed elliptical vibrator was verified by generating complex micro-dimple structures with tunable wavelength and height on pure copper, a common ductile material. Furthermore, the wavelength and height errors of less than 1.26% and 10.67% were demonstrated in the machining trials, showing an excellent frequency and amplitude stability of this vibrator.

(4) Discontinuous copper chips were manufactured with the aid of this vibrator, thereby verifying its chip-breaking effectiveness on ductile material.

Chapter 7

Manufacturing of filamentous silk particles using elliptical vibration diamond turning

7.1 Introduction

This chapter will thoroughly study the machining mechanism and performance of using elliptical vibration diamond turning to manufacture filamentous silk particles.

A hybrid FE-SPH numerical model for elliptical vibration diamond turning of silk fibroin is developed. The model is evaluated and validated by experimental results from the aspects of specific cutting force and chip morphology (i.e. shear band spacing). After that, conventional diamond turning (i.e. without tool vibration) and elliptical vibration diamond turning are compared using this numerical model to study the effects of frequency and amplitude of the tool vibration on cutting force, chip formation and residual stress in the machined surface.

Moreover, the effect of processing parameters such as depth ratio and HSR on chip breakability in elliptical vibration diamond turning of silk fibroin is investigated. They both affect the chip breakability through changing the average tool velocity angle θ_a. Based on the simulation and experimental results, the critical average tool velocity angle θ_c for manufacturing filamentous silk particles is confirmed. The mechanism of how the average tool velocity angle will influence the chip breakability is also revealed in this chapter.

7.2 Hybrid FE-SPH modelling

7.2.1 Orthogonal cutting model for elliptical vibration diamond turning

In this chapter, elliptical vibration diamond turning is assumed to be an orthogonal cutting process. The simplicity and theoretical treatment of the model are the same as those in Chapter 4.

A 3D workpiece with the size of 15 μm × 15 μm × 0.5 μm was modelled in an orthogonal cutting framework using LS-PrePost. Figure 7.1 shows the hybrid FE-SPH numerical model established in this chapter.

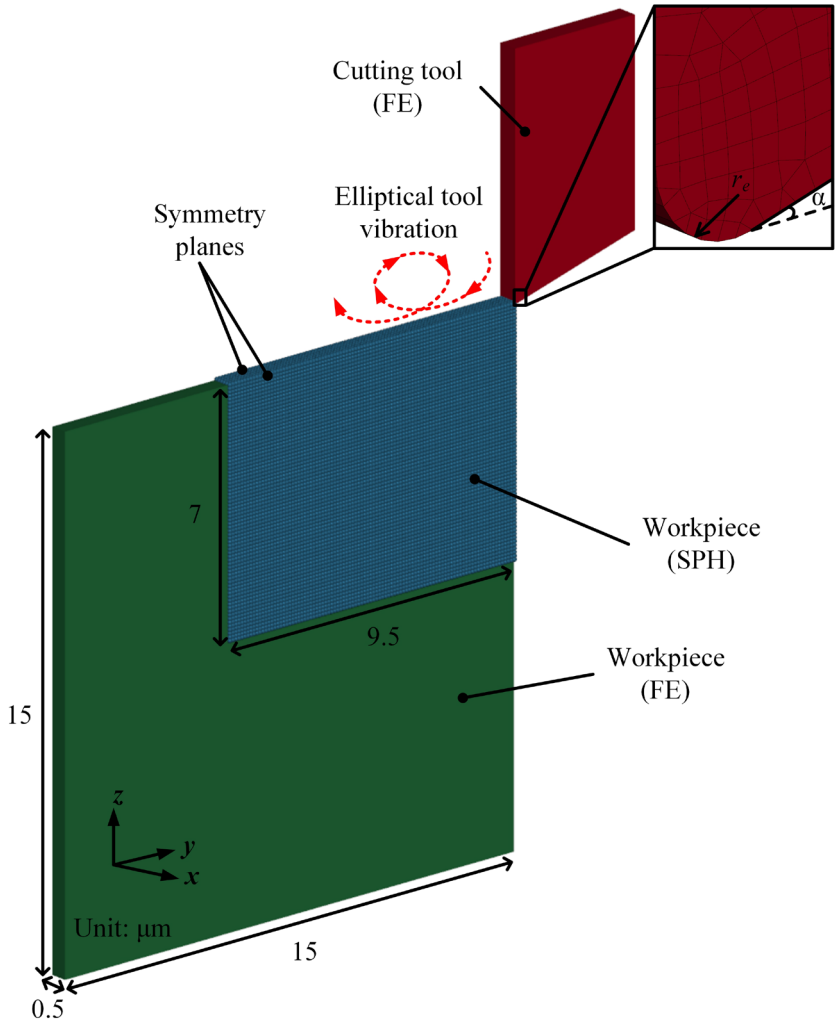

Figure 7.1 Hybrid FE-SPH numerical model for elliptical vibration diamond turning.

The workpiece was divided into two domains: one representing the SPH domain (9.5 μm × 7 μm × 0.5 μm) using the renormalized formulation and the rest representing the FE domain. The FE region was discretized using eight-node Lagrangian solid elements. The particle density of the SPH domain was decreased to be 0.1 μm. Thus, the number of SPH particles over the chip thickness was increased. The total number of SPH particles approached 40,896. The mesh size for the continuum FE domain was 0.25 μm. Besides, two symmetry planes were imposed on the front and back faces of the SPH domain, which was the same as those in Chapter 4.

Furthermore, the fixed boundary conditions were applied on the bottom and left-hand faces of the workpiece. At the FE-SPH interface, the Lagrangian meshes and SPH particles were coupled by a tied contact formulation whose effectiveness has been verified in previous research [125]. The tool rake angle was 0°, while the clearance angle α was 15°. The tool edge radius r_e was 60 nm. At the same time, the mesh around the tool tip was sufficiently refined to increase the model accuracy. The coefficient of Coulomb friction between the tool and workpiece was 0.12 [158]. The time scaling technique was not adopted in this chapter. The material parameters for the diamond tool and the silk fibroin workpiece are listed in Table 7.1.

Table 7.1 Material parameters in the orthogonal cutting model.

Material parameters	Silk fibroin	Diamond tool
Density (g/cm^3)	1.4	3.5
Young's modulus (GPa)	5.2	1050
Poisson's ratio	0.3	0.1
Static yield stress (MPa)	70	N/A
Tangent modulus (MPa)	172.4	N/A
Cowper-Symonds parameter p	7	N/A
Cowper-Symonds parameter D (s^{-1})	1140	N/A

7.2.2 Simulation conditions

The diamond tool in the numerical model oscillates periodically in the cutting and depth of cut directions to reproduce the elliptical tool trajectories in elliptical vibration diamond turning. The phase angle between the two directions was 90°. The tool displacements in the *y*- (cutting) and *z*- (depth of cut) directions are given in the following equations:

$$\begin{cases} y(t) = a\cos(2\pi ft) - V_w t - a \\ z(t) = -b\sin(2\pi ft) \end{cases} \quad (7\text{-}1)$$

where a and b are the tool path dimensions in corresponding directions. f is the vibration frequency. V_w is the nominal cutting speed of the workpiece. Typical variations of the velocity and displacement of the cutting tool in conventional diamond turning and elliptical vibration diamond turning are illustrated in Figure 7.2. The identical nominal cutting speed of 0.2 m/s was employed in both models to make them comparable. In such cases, the vibration amplitude of the tool in the cutting and depth of cut directions was 2 μm, while the frequency was 40 kHz. The linear and elliptical motions of the cutting tool were implemented as a boundary condition of the orthogonal model. The biggest difference between the conventional and elliptical vibration diamond turning processes is that the tool permanently contacts the workpiece in the conventional process, while the tool/workpiece contact becomes intermitted after employing the elliptical vibration.

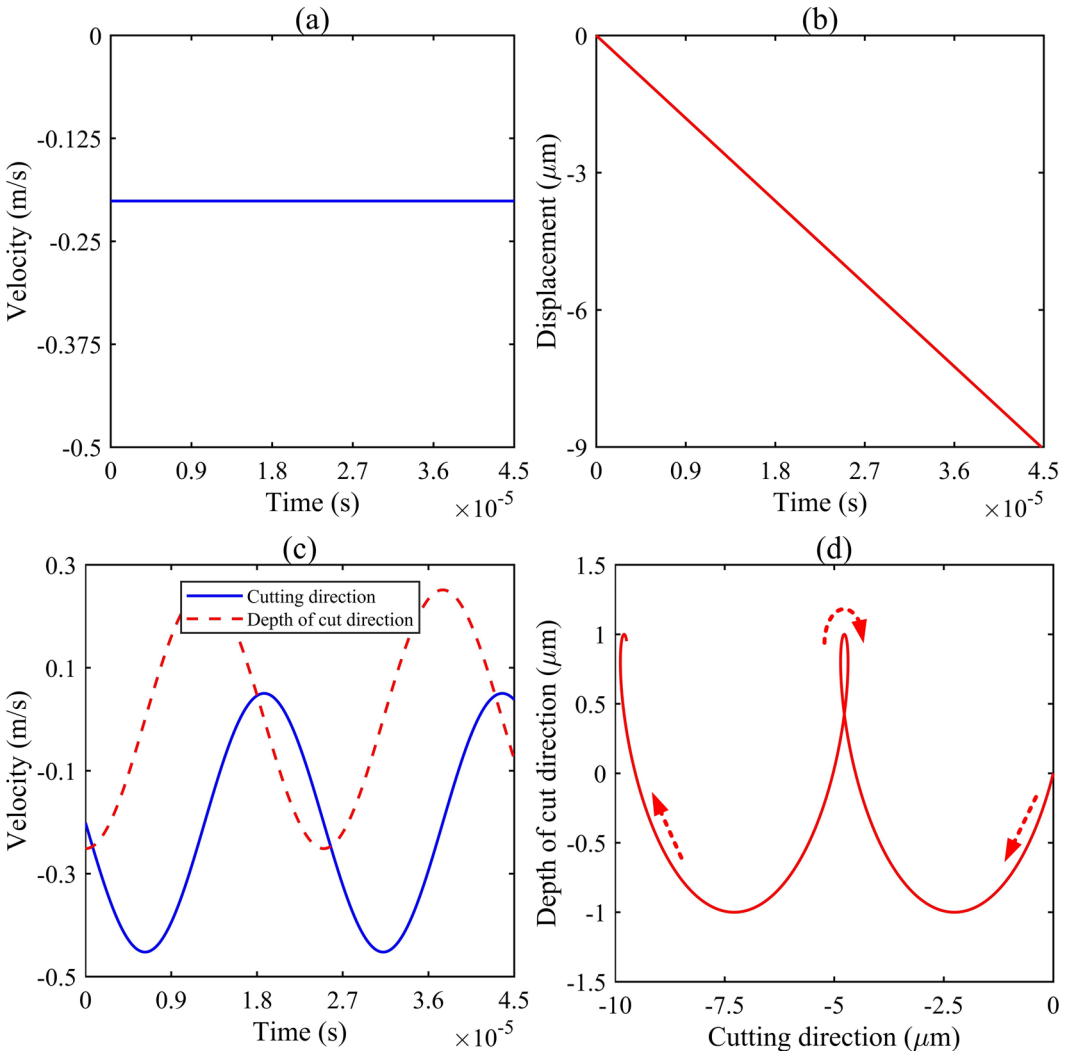

Figure 7.2 Typical variations of tool velocity and displacement: (a) velocity in conventional diamond turning; (b) displacement in conventional diamond turning; (c) velocity in elliptical vibration diamond turning; (d) displacement in elliptical vibration diamond turning.

7.2.3 Model evaluation and verification

In order to evaluate and verify the orthogonal cutting model established in this chapter, a series of simulations were conducted for conventional diamond turning of

silk fibroin with a cutting speed of 1.35 m/s and different depths of cut. The simulated chip morphology is illustrated in Figure 7.3.

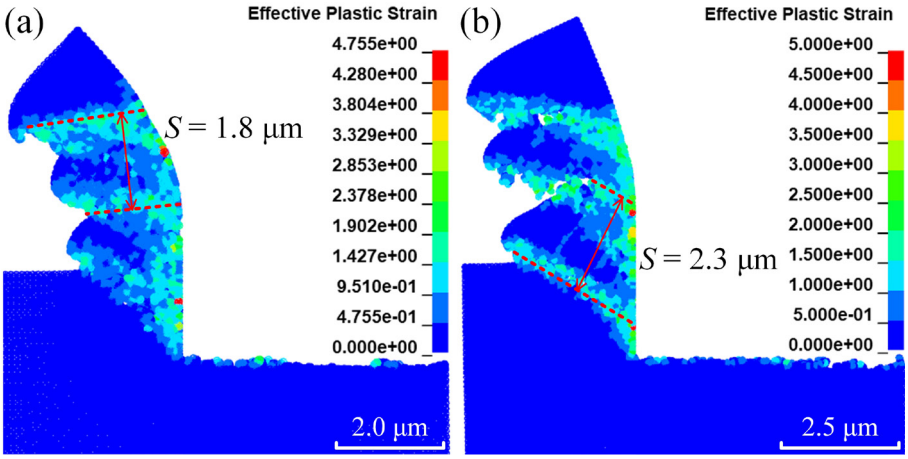

Figure 7.3 Simulated chip morphology: (a) depth of cut d_c = 1.5 µm; (b) depth of cut d_c = 2 µm.

The chip segmentation and shear localization on the free surface can be observed in both simulated chips, engaging with the measured results shown in Figure 3.5. The approximate shear band spacing S in experiments with a depth of cut of 2 µm is 2.4 µm. In addition, for a depth of cut of 1.5 µm, the measured shear band spacing S is about 2.1 µm. As shown in Figure 7.3, the shear band spacing reaches 1.8 µm and 2.3 µm for a depth of cut of 1.5 µm and 2 µm, respectively, which agrees well with the measured values.

In addition, a good estimation of the specific cutting force was also achieved with the aid of this model. Figure 7.4 compares the simulated and measured specific cutting forces.

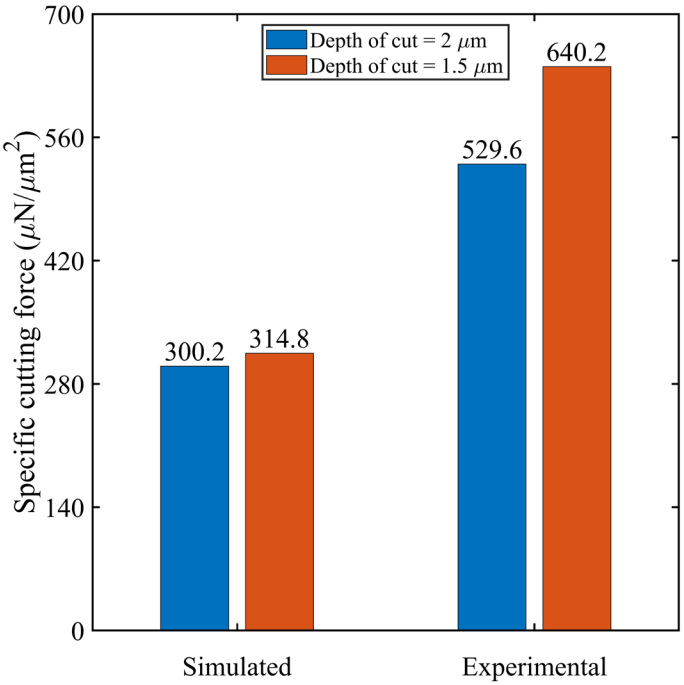

Figure 7.4 Simulated and experimental specific cutting forces comparisons.

The specific cutting force with a depth of cut of 2 μm reaches 300.2 μN/μm^2, which is 56.7% of the experimental value. Moreover, when the depth of cut is 1.5 μm, the specific cutting force obtained from the numerical simulation is 314.8 μN/μm^2, which is 49.2% of the measured result. Thus, the effectiveness of the numerical model established in this chapter is verified considering the good prediction regarding the specific cutting force and chip morphology.

7.3 Comparison between conventional and elliptical vibration diamond turning

7.3.1 Effect of vibration frequency

In order to investigate the effect of vibration frequency on elliptical vibration diamond turning of silk fibroin, three levels of magnitudes (i.e. 20 kHz, 30 kHz and 40 kHz) were adopted in the simulation studies considering the constriction of

available computational power. The tool path dimensions a and b were set to 1 μm and remained unchanged. The cutting simulations were conducted under the same nominal cutting speed for both conventional and elliptical vibration diamond turning processes. The nominal depth of cut employed in these two processes was identical and equal to the tool path dimension b (depth ratio r_d = 1). Therefore, the simulation data of conventional diamond turning can be used as a benchmark for the elliptical vibration process. It is worth mentioning that although different frequencies were used in the cases, all the simulations ran in the same time length. Moreover, the simulated cutting forces were normalized in the x-direction for ease of comparison. Figure 7.5 illustrates the signatures of the unit cutting force, while the average values of the signatures are shown in Figure 7.6.

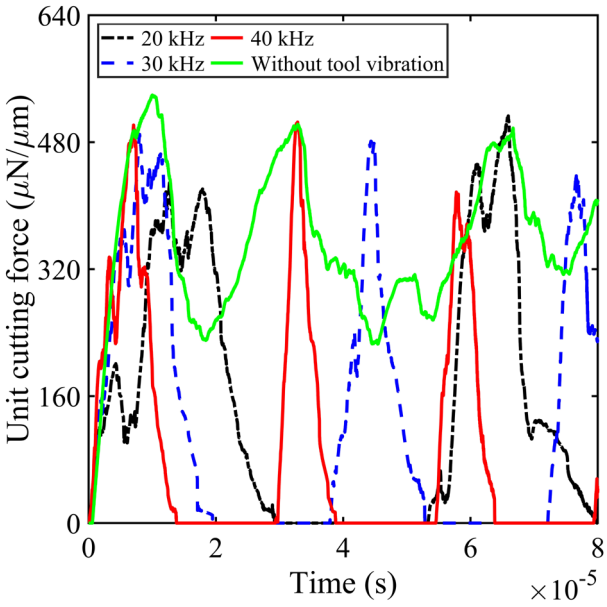

Figure 7.5 The signatures of the unit cutting force for conventional diamond turning and elliptical vibration diamond turning under various vibration frequencies.

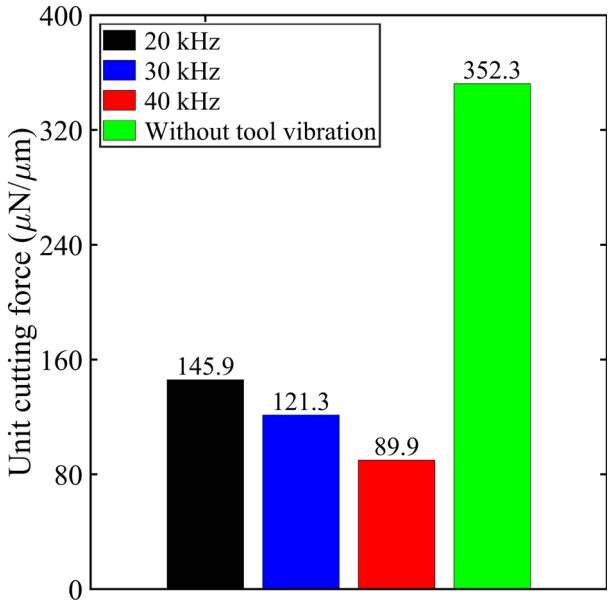

Figure 7.6 The average values of the unit cutting force for conventional diamond turning and elliptical vibration diamond turning under various vibration frequencies.

As shown in Figure 7.5, the peak values of the unit cutting force are almost at the same level in all simulation cases, while the average values reduce continuously when the frequency is increased from 20 kHz to 40 kHz. A reduction of 58.6% in unit cutting force compared to conventional diamond turning can be observed for 20 kHz. A further increase of vibration frequency to 30 kHz and 40 kHz results in an average reduction of 65.6% and 74.5%, respectively, which is due to the extension of tool/workpiece separation.

Figure 7.7 presents the distribution of von Mises stress, effective plastic strain and hydrostatic pressure for conventional diamond turning. Figure 7.8 illustrates the distribution of von Mises stress for elliptical vibration diamond turning with various frequencies.

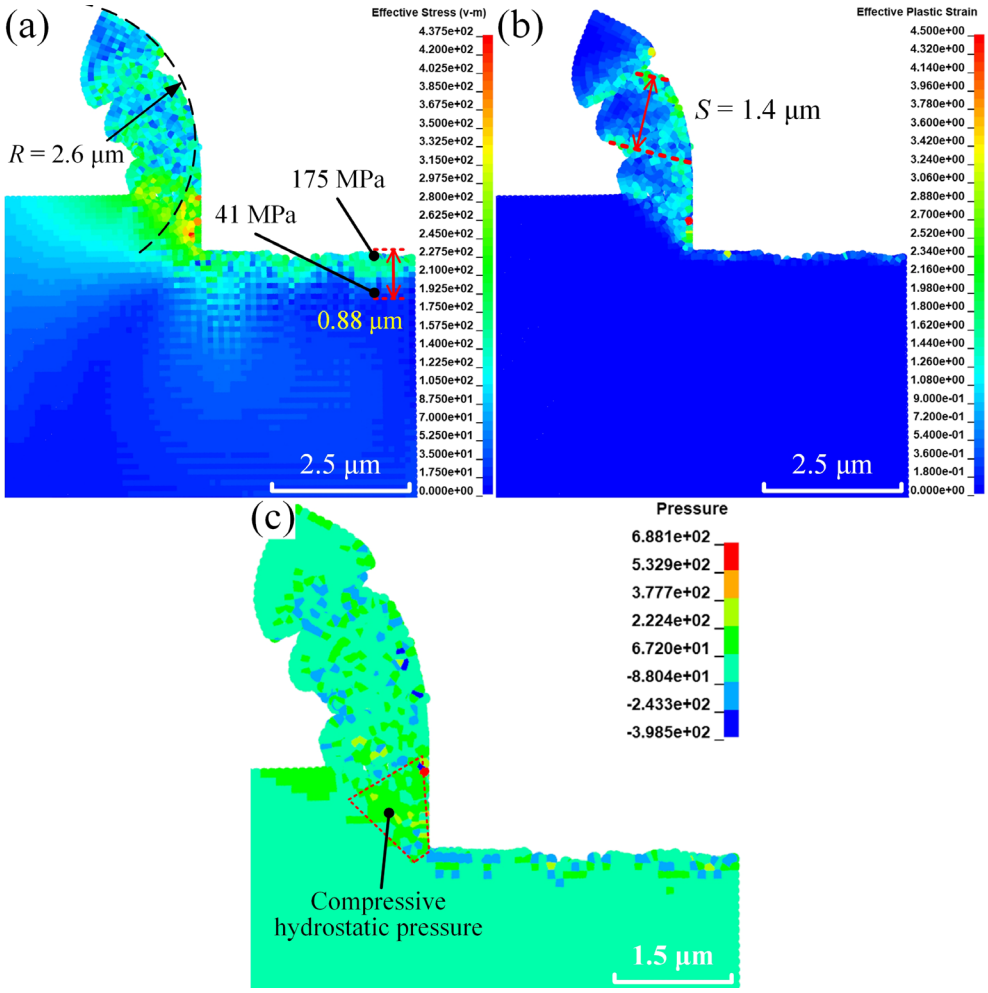

Figure 7.7 The distribution of: (a) von Mises stress (unit: MPa); (b) effective plastic strain; (c) hydrostatic pressure (unit: MPa) in conventional diamond turning.

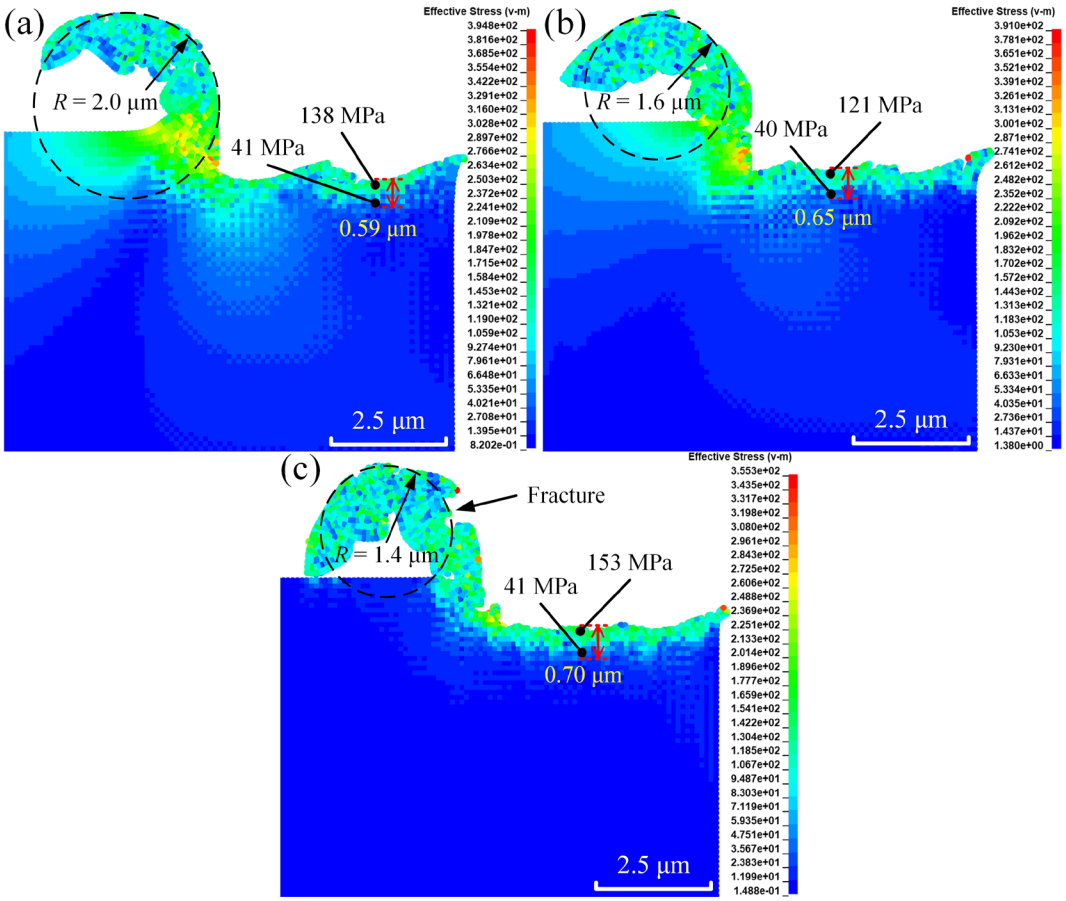

Figure 7.8 The distribution of von Mises stress in elliptical vibration diamond turning with a fixed vibration amplitude of 2 µm and different frequencies: (a) 20 kHz; (b) 30 kHz; (c) 40 kHz.

The reduction in unit cutting force for elliptical vibration diamond turning also leads to a decrease in residual stress of the machined surface compared to conventional diamond turning. The maximum value of the residual stress and the depth of the residual stress field for conventional diamond turning are greater than those with the elliptical vibration. Not only that, as shown in Figure 7.8, an increase in the magnitude of vibration frequency brings about a higher maximum residual stress and a deeper residual stress field due to the larger number of tool impacts onto the workpiece per second. Figure 7.7 (b) shows that the predicted shear band spacing S for conventional

diamond turning with a depth of cut of 1 μm is only 1.4 μm. The spacing *S* is smaller than those with a depth of cut of 1.5 μm and 2 μm, as displayed in Figure 4.5, which agrees well with expectations, as the band spacing is positively correlated with the depth of cut [182]. Besides, a large area of compressive hydrostatic pressure in the cutting chip and in front of the tool rake face can be spotted in Figure 7.7 (c). It is considered that the ductility of a damaging material is strongly influenced by external pressures [183]. In more detail, a tensile hydrostatic pressure will decrease the ductility, making the chips break in an easy fashion. In contrast, the compressive hydrostatic pressure can increase the ductility of the work material and therefore postpone its fracture and failure, which decreases the chip breaking tendency. This is an important reason why the chip-breaking efficiency in conventional diamond turning is relatively low.

Moreover, the chip morphologies regarding chip radius of curvature *R* are significantly different for diamond turning with and without the elliptical vibration. As illustrated in Figure 7.7 (a), the simulated radius of curvature for conventional diamond turning is 2.6 μm, which is higher than those after applying the elliptical vibration. At the same time, Figure 7.7 shows that a further increase in the frequency reduces the radius of curvature. The elliptical vibro-impact of the tool is one possible reason for this change, which results in the energy concentration at the cutting zone. Thus the curling degree of the chip is increased. As noted in previous research [37], a decrease in the radius of curvature helps break the chip. Moreover, as shown in Figure 7.8 (c), a fracture in the cutting chip was formed in the simulation case with a frequency of 40 kHz, showing that the chip breaking might occur more efficiently under a high frequency. This assumption will be verified later through experimental investigations.

7.3.2 Effect of vibration amplitude

Four levels of tool path dimension *b* (i.e. 0.5 μm, 0.75 μm, 1 μm and 1.5 μm) were chosen for analysis to study the effect of vibration amplitude on elliptical vibration diamond turning. Thus, the vibration amplitudes were equal to 1 μm, 1.5 μm, 2 μm and 3 μm, respectively. Note that the nominal depth of cut was set identically to the tool path dimension *b* in all simulation cases; thus the depth ratio remained fixed at 1. The simulations were conducted with the same vibration frequency of 20 kHz. The same nominal cutting speed of 0.05 m/s was employed in all cases for comparison.

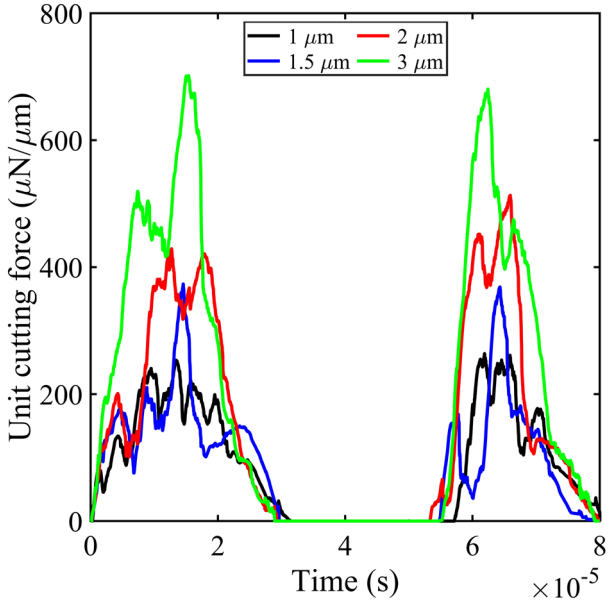

Figure 7.9 The signatures of the unit cutting force for elliptical vibration diamond turning with various vibration amplitudes.

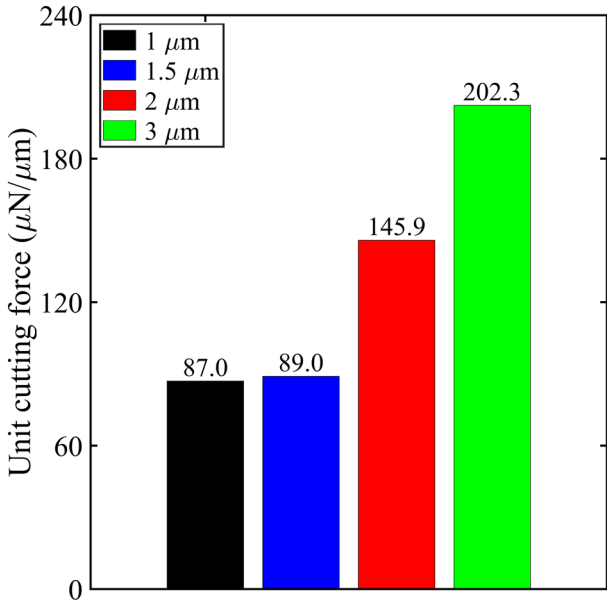

Figure 7.10 The average values of the unit cutting force for elliptical vibration diamond turning with various vibration amplitudes.

The growth in the vibration amplitude increases the unit cutting force. This increase is attributed to the growth in nominal depth of cut, and thus larger volume of the silk fibroin is removed. At the same time, the deformation rate is increased with increasing amplitude, which results in the strain rate hardening of the material. Therefore, the unit cutting force is increased according to Equation 2-39.

Figure 7.11 illustrates the chip morphology for elliptical vibration diamond turning with a fixed vibration frequency of 20 kHz and different vibration amplitudes.

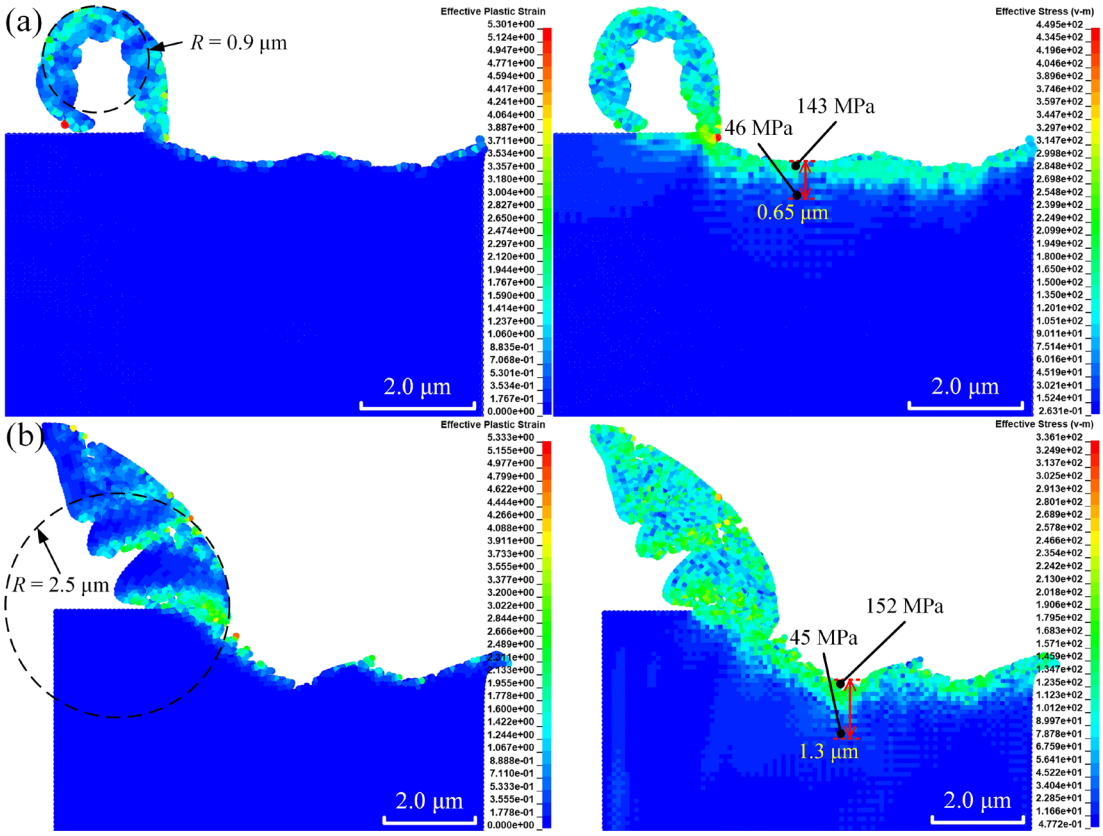

Figure 7.11 The distribution of effective plastic strain and von Mises stress (unit: MPa) in elliptical vibration diamond turning with a fixed vibration frequency of 20 kHz and different amplitudes: (a) 1 μm; (b) 3 μm.

The results show that the vibration amplitude significantly influences the chip morphology in elliptical vibration diamond turning. An increase in the amplitude increases the chip radius of curvature R as the result of the growth in chip thickness and thus the chip stiffness. On the other hand, a higher residual stress and a larger depth of residual stress field can be identified in the machined surface with a greater vibration amplitude. This is because the diamond tool wedged deeper into the silk fibroin, leading to a higher deformation rate, strain rate and effective stress. The residual stress in the machined surface is thus increased.

7.4 Parametric study on chip breaking in elliptical vibration diamond turning

7.4.1 Unique characteristics in elliptical vibration diamond turning

The tool velocity angle is fixed in the conventional process, while it varies with time along the tool's trajectory in elliptical vibration diamond turning. Figure 7.12 is a schematic to illustrate the tool velocity angle θ in elliptical vibration diamond turning. It has been given that tool velocity angle can significantly affect the ductile-brittle transition of the work material [184]. It can, therefore, be expected that the chip-breaking behaviour will be simultaneously influenced.

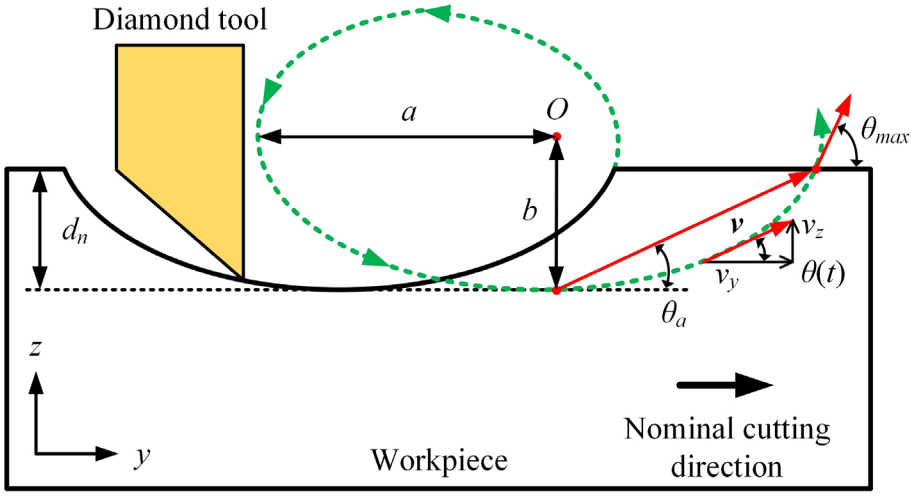

Figure 7.12 Schematic illustration of the tool velocity angle in elliptical vibration diamond turning.

The transient tool velocity angle $\theta(t)$ is defined as the angle of the transient tool velocity vector $\boldsymbol{v}$ relative to the y-axis:

$$\theta(t) = \tan^{-1}\left|\frac{v_z(t)}{v_y(t)}\right| \tag{7-2}$$

where $v_y(t)$ and $v_z(t)$ are the components of the tool velocity vector on the y- and z-axis, respectively. Note that only the processing condition nominal depth of cut d_n less than tool path dimension b (i.e. depth ratio $r_d < 1$) is of interest in this chapter for effective chip breaking. A neutral rake angle tool is adopted for simplification.

As shown in Figure 7.12, θ_{max} is the maximum tool velocity angle which is the velocity angle when the tool/workpiece engagement is ended. θ_a is the average tool velocity angle, which can be derived as:

$$\theta_a = \tan^{-1}\left(\frac{d_n}{a} \cdot \frac{1}{\sqrt{1-(1-r_d)^2}}\right) \tag{7-3}$$

In the actual elliptical vibration diamond turning, an increase in the HSR will increase the actual tool path dimension a, as the tool trajectory will be stretched out horizontally. Thus, based on Equation 7-3, the average tool velocity angle is significantly impacted by the depth ratio r_d and HSR.

Therefore, to study the effect of tool velocity angle on chip-breaking behaviour in elliptical vibration diamond turning of silk fibroin, three levels of HSR (0.1, 0.3 and 0.9) and three levels of depth ratio (0.4, 0.5 and 0.7) were analysed with the aid of the FE-SPH numerical model. A vibration frequency of 20 kHz was chosen for all simulation cases. The tool path dimensions a and b were set to 1 μm.

7.4.2 Effect of HSR

Some researchers have pointed out that, in elliptical vibration diamond turning, tool velocity angle can significantly affect the hydrostatic pressure and shear stress on work materials and chips [184,185]. Thus, to study the effect of HSR, the hydrostatic pressure distribution under different values of HSR at the moment that the

tool/workpiece engagement is ended and the moment that the tool withdraws from the chip is shown in Figure 7.13. In addition, the distribution of von Mises stress with the change of HSR when the tool stops engaging with the workpiece is illustrated in Figure 7.14.

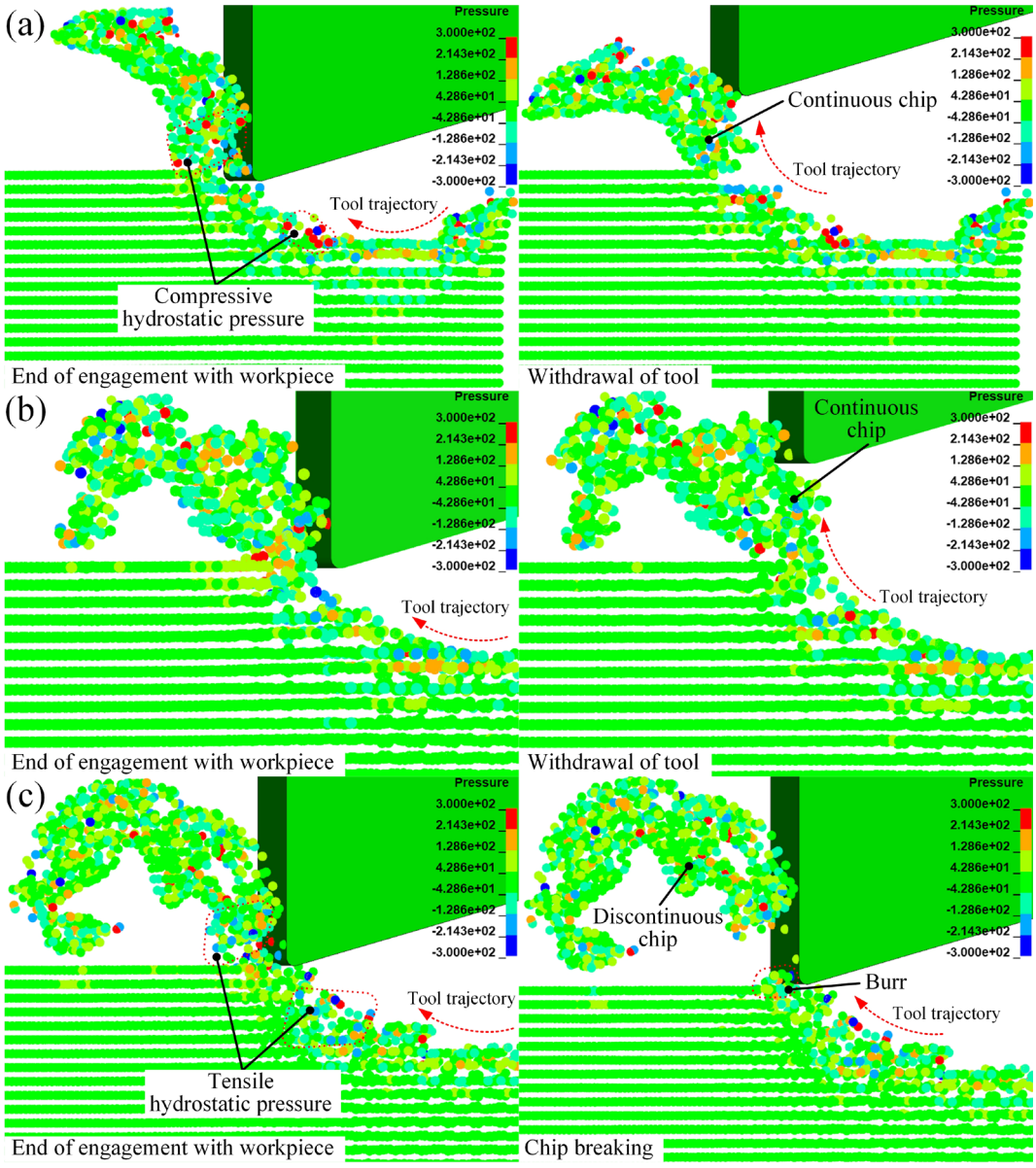

Figure 7.13 Distribution of hydrostatic pressure (unit: MPa) in elliptical vibration diamond turning with different values of HSR: (a) HSR = 0.1 (θ_a = 27.3°); (b) HSR = 0.3 (θ_a = 23.0°); (c) HSR = 0.9 (θ_a = 15.5°).

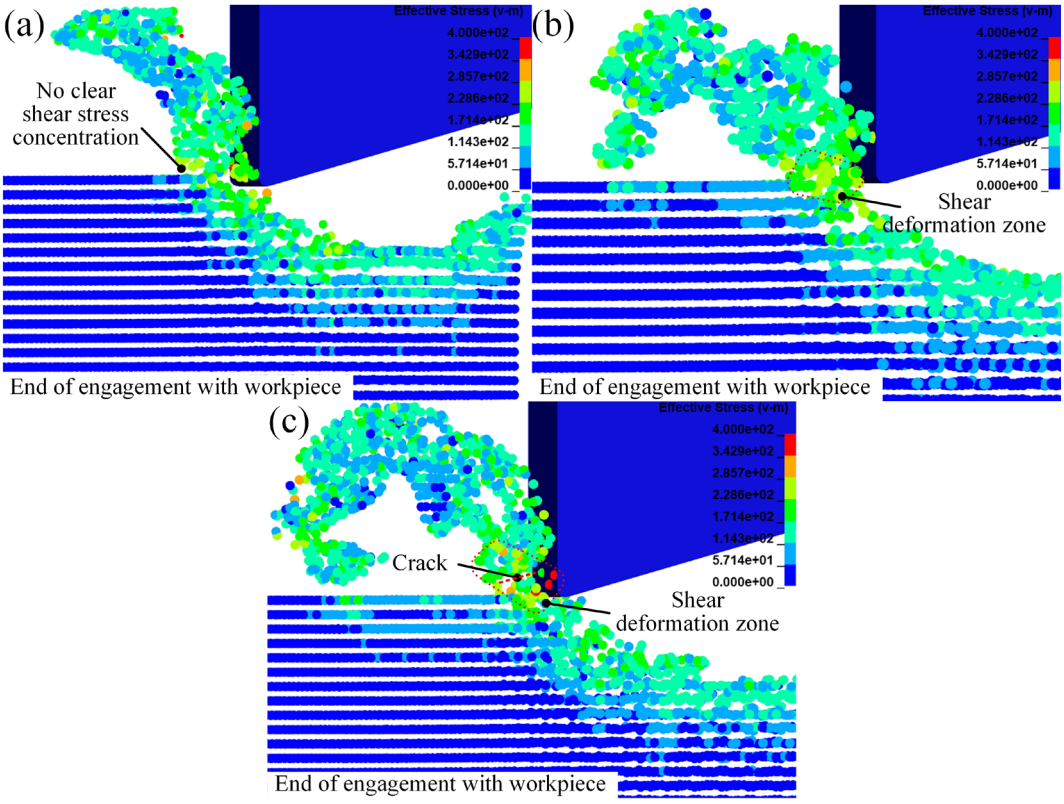

Figure 7.14 Distribution of von Mises stress (unit: MPa) in elliptical vibration diamond turning with different values of HSR: (a) HSR = 0.1 (θ_a = 27.3°); (b) HSR = 0.3 (θ_a = 23.0°); (c) HSR = 0.9 (θ_a = 15.5°).

The depth ratio was fixed at 0.5, which means the nominal depth of cut was 0.5 μm in all cases. The same scale of the colour legend is used in each figure to monitor the pressure and stress changes. Figure 7.13 shows that when the HSR is increased from 0.1 to 0.9, the average tool velocity angle is therefore decreased from 27.3° to 15.5°. During this process, high (compressive) hydrostatic pressure was first generated in front of the tool rake face and below the tool edge when the HSR was 0.1. With a further increase in HSR, the value of hydrostatic pressure drops and evolves into tensile hydrostatic pressure. The ductility of the silk fibroin is decreased as a consequence, contributing to crack initiating and thus chip breaking. The

discontinuous chip was generated when the HSR reached 0.9, as shown in Figure 7.13 (c). The generated chip is thin at the front and thick at the back, following the expected geometry of discontinuous chips in elliptical vibration diamond turning. The excellent prediction of the chip geometry is attributed to the natural material flow reproduced by SPH technique.

As for von Mises stress, Figure 7.14 (a) shows that there is no clear shear stress concentration in front of the tool rake face with an HSR of 0.1. The shear stress is continuously concentrated and thus forming a shear deformation zone in the chip with the increase of HSR. This is because greater HSR results in smaller tool velocity angle, so the extrusion and shearing action of the diamond tool is enhanced. As shown in Figure 7.14 (c), with the advance of the diamond tool and shear strain accumulation, a crack in the chip is initiated and propagates along the narrow shear deformation zone. After that, effective chip breaking is achieved.

7.4.3 Effect of depth ratio

The distribution of hydrostatic pressure under different values of depth ratio is shown in Figure 7.15. Likewise, two moments are of interest: the moment the tool ends the engagement with the workpiece and the moment the tool withdraws from the chip. Figure 7.16 illustrates the distribution of von Mises stress when the tool/workpiece engagement is ended. The HSR was fixed at 0.4. The colour legend with the same scale is adopted in each figure for observation of pressure and stress changes.

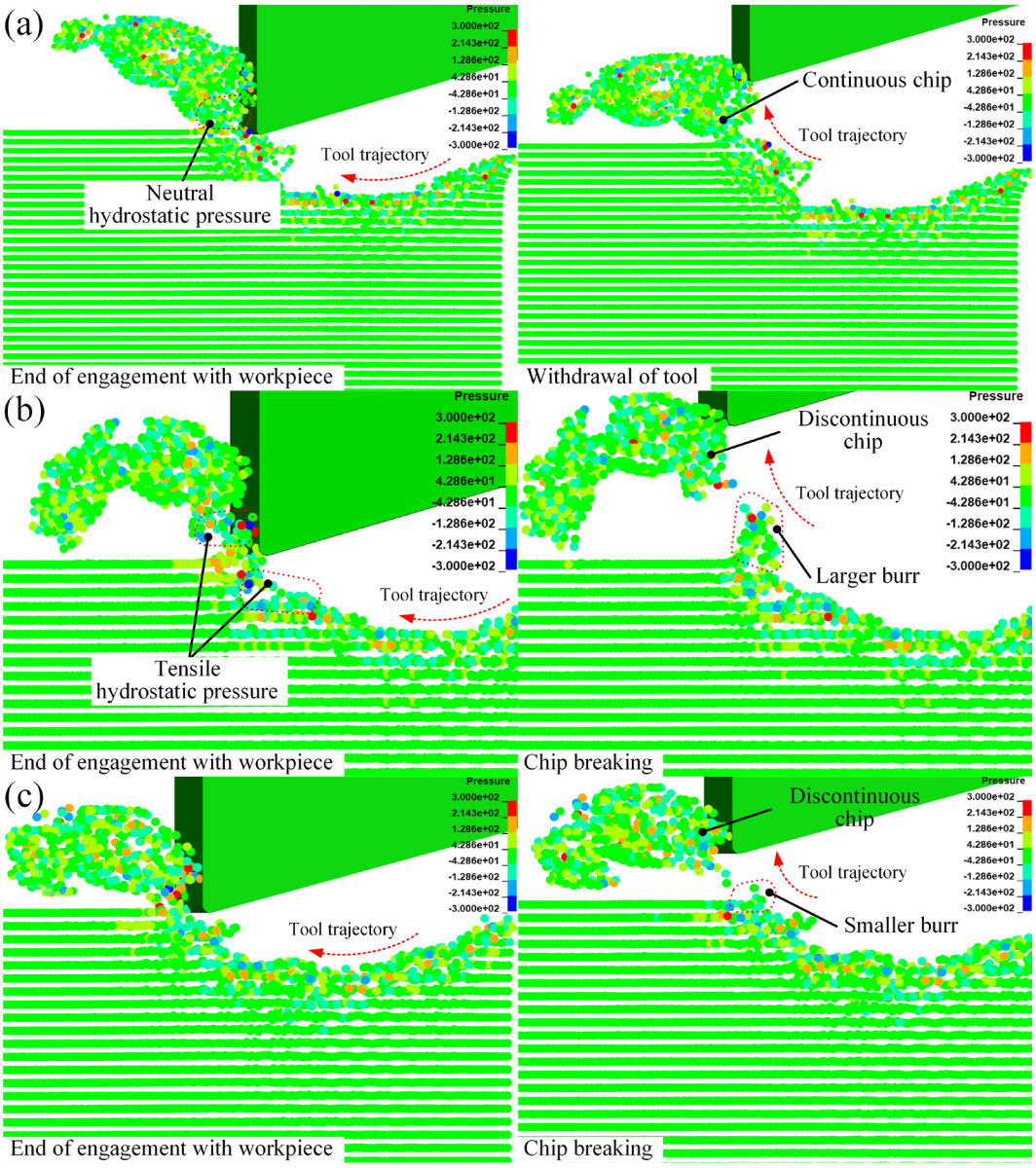

Figure 7.15 Distribution of hydrostatic pressure (unit: MPa) in elliptical vibration diamond turning with different values of depth ratio: (a) $r_d = 0.7$ ($\theta_a = 25.6°$); (b) $r_d = 0.5$ ($\theta_a = 21.3°$); (c) $r_d = 0.4$ ($\theta_a = 18.9°$).

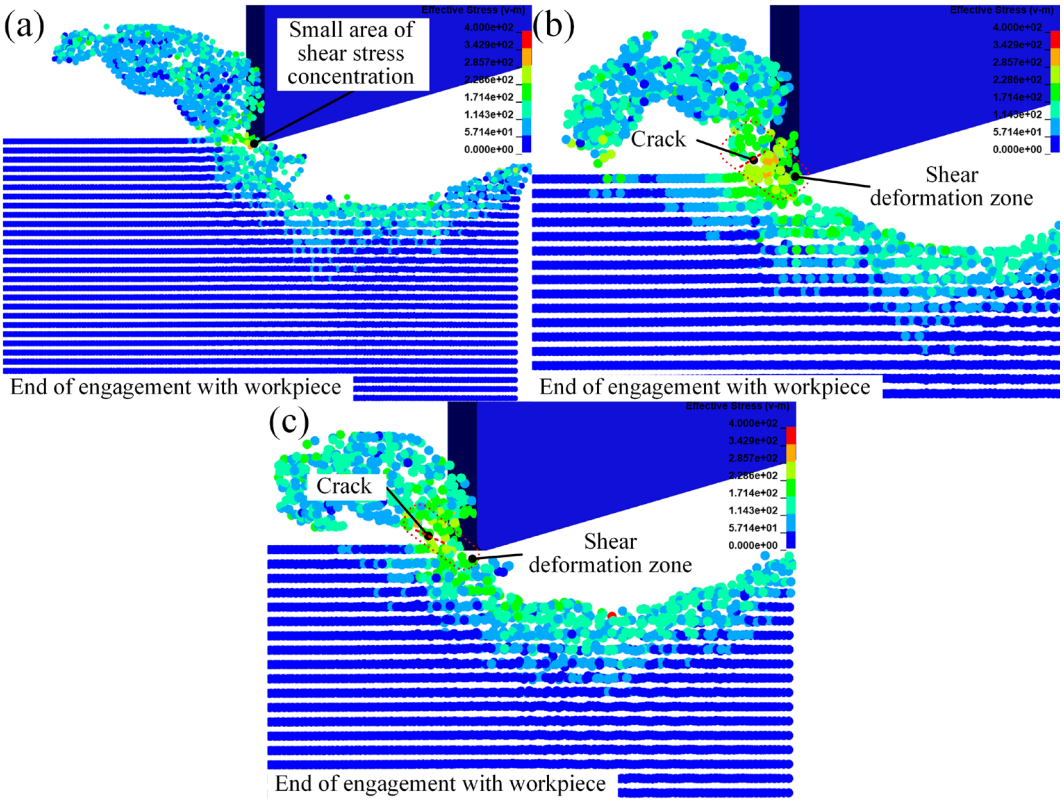

Figure 7.16 Distribution of von Mises stress (unit: MPa) in elliptical vibration diamond turning with different values of depth ratio: $r_d = 0.7$ ($\theta_a = 25.6°$); (b) $r_d = 0.5$ ($\theta_a = 21.3°$); (c) $r_d = 0.4$ ($\theta_a = 18.9°$).

As displayed in Figure 7.15, when the depth ratio is decreased from 0.7 to 0.4, the average tool velocity angle is decreased from 25.6° to 18.9° correspondingly. At the same time, the value of the hydrostatic pressure in front of the tool rake face changes from nearly neutral to negative (compressive), as illustrated in Figure 7.15 (a) and (b), which can decrease the ductility of silk fibroin. According to previous studies [186,187], the work materials with higher ductility tend to generate larger burrs. As a result, a larger burr is formed with a depth ratio of 0.5 compared to those with a depth of 0.4.

Figure 7.16 (a) shows that a small shear stress area is formed in front of the tool rake face with a depth ratio of 0.7. The shear stress and strain are further accumulated with the decrease of depth ratio, forming a shear deformation zone in the chip. Moreover, the enhanced shearing action of the diamond tool in elliptical vibration diamond turning with a smaller average tool velocity angle also helps suppress the burr formation. Figure 7.16 (b) displays that the silk chip starts to break, and thus discontinuous chip is generated when the depth ratio approaches 0.5 or less after the crack initiation and propagation.

Therefore, it can be concluded that, with a decrease in the average tool velocity angle θ_a, effective chip breaking in elliptical vibration diamond turning of silk fibroin is achieved through the joint efforts between the ductility weakening of silk fibroin and the strengthened shearing action of the diamond tool. Based on the simulation results, the critical tool velocity angle θ_c for chip breaking lies between 21.3° and 23.0°, whose specific value needs to be confirmed with the aid of experimental investigation in the following section.

7.5 Manufacturing of filamentous silk particles

7.5.1 Manufacturing setup and manufacturing conditions

A couple of manufacturing trials were conducted on a diamond turning machine using the proposed elliptical vibrator in order to obtain filamentous silk particles. Figure 7.17 shows the manufacturing setup.

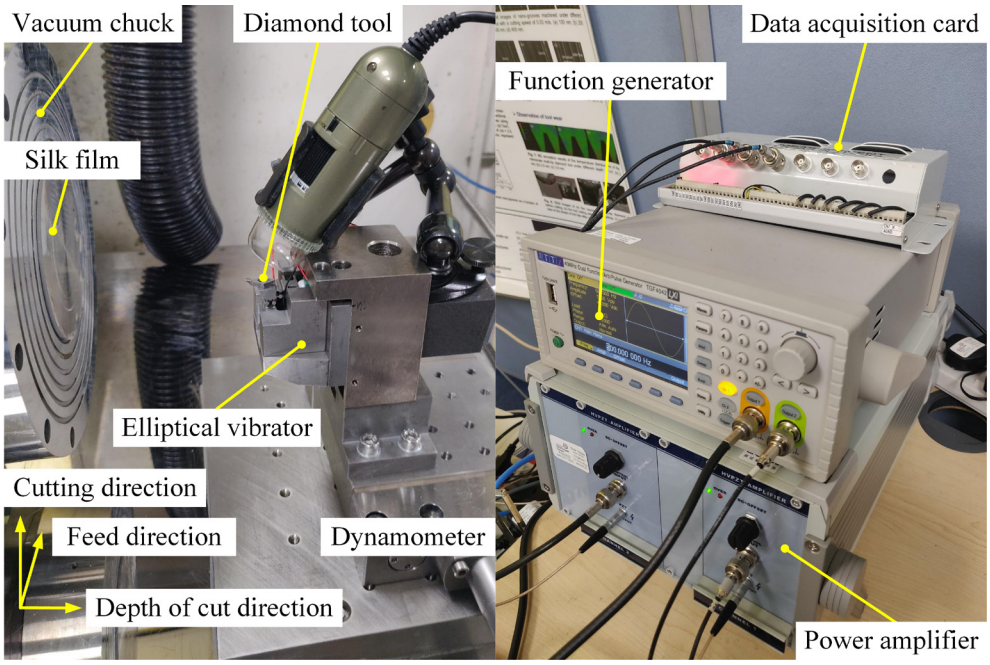

Figure 7.17 Setup for manufacturing filamentous silk particles.

A silk film workpiece was mounted on a vacuum chuck of the air spindle. A round nose tool with a nose radius of 0.2 mm, a rake angle of 0° and a clearance angle of 15° was adopted. The cutting force measurement was accomplished using a three-component dynamometer (9129AA, Kistler) mounted underneath the tool holder. A data acquisition card (USB-1608HS, Measurement Computing) was used for force data collection. Furthermore, the observation of silk chips was taken on an SEM (S3700-N, Hitachi).

The processing parameters for four sets of machining trials designated in A, B, C and D are shown in Table 7.2. In this experiment, two vibration frequencies of 100 Hz and 500 Hz were employed. The tool path dimensions *a* and *b* were approximately 0.75 μm and 1 μm, respectively. Thus, the depth ratio was 0.5 in the experiments of sets A and B, whereas it was chosen as 0.7 in set C. The feed rate was set to be 150 μm/rev in all experiments for non-overlapping cutting.

Table 7.2 Processing parameters for conventional and elliptical vibration diamond turning experiments.

Set	Cutting mode	Vibration frequency (Hz)	HSR	Nominal depth of cut (μm)
A	Elliptical vibration	100	0.1; 0.3; 0.5; 0.7; 0.9	0.5
B	Conventional	N/A	N/A	0.5
C	Elliptical vibration	100	0.3; 0.9	0.7
D	Elliptical vibration	500	0.9	0.5

7.5.2 Experimental results and discussions

Conventional diamond turning experiments (set B) were conducted under the same nominal cutting speed (i.e. 424.1 μm/s) as those in set A under an HSR of 0.9. The measured cutting forces in these two experiments are compared in Figure 7.18.

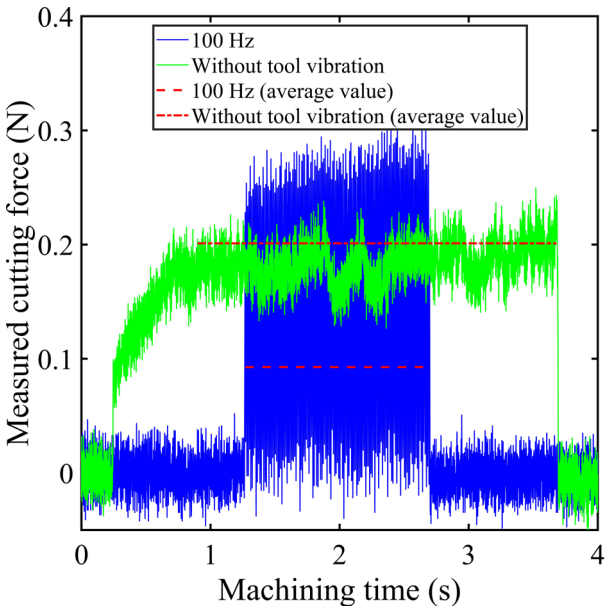

Figure 7.18 Comparison of conventional diamond turning (d_c = 0.5 μm) and elliptical vibration diamond turning (f = 100 Hz; HSR = 0.9; d_n = 0.5 μm) on cutting force variations.

The peak cutting force for elliptical vibration diamond turning was slightly higher than that in conventional diamond turning due to the vibration of the diamond tool. However, the average cutting force was reduced by 53.9% in comparison with conventional diamond turning because of the intermittent tool/workpiece contact after applying the elliptical vibration. This phenomenon is consistent with the simulation results.

Figure 7.19, 7.20 and 7.21 illustrate the chip morphologies obtained in the experiments of sets A, C and D, respectively. The corresponding figure title gives the average tool velocity angles under specific processing parameters.

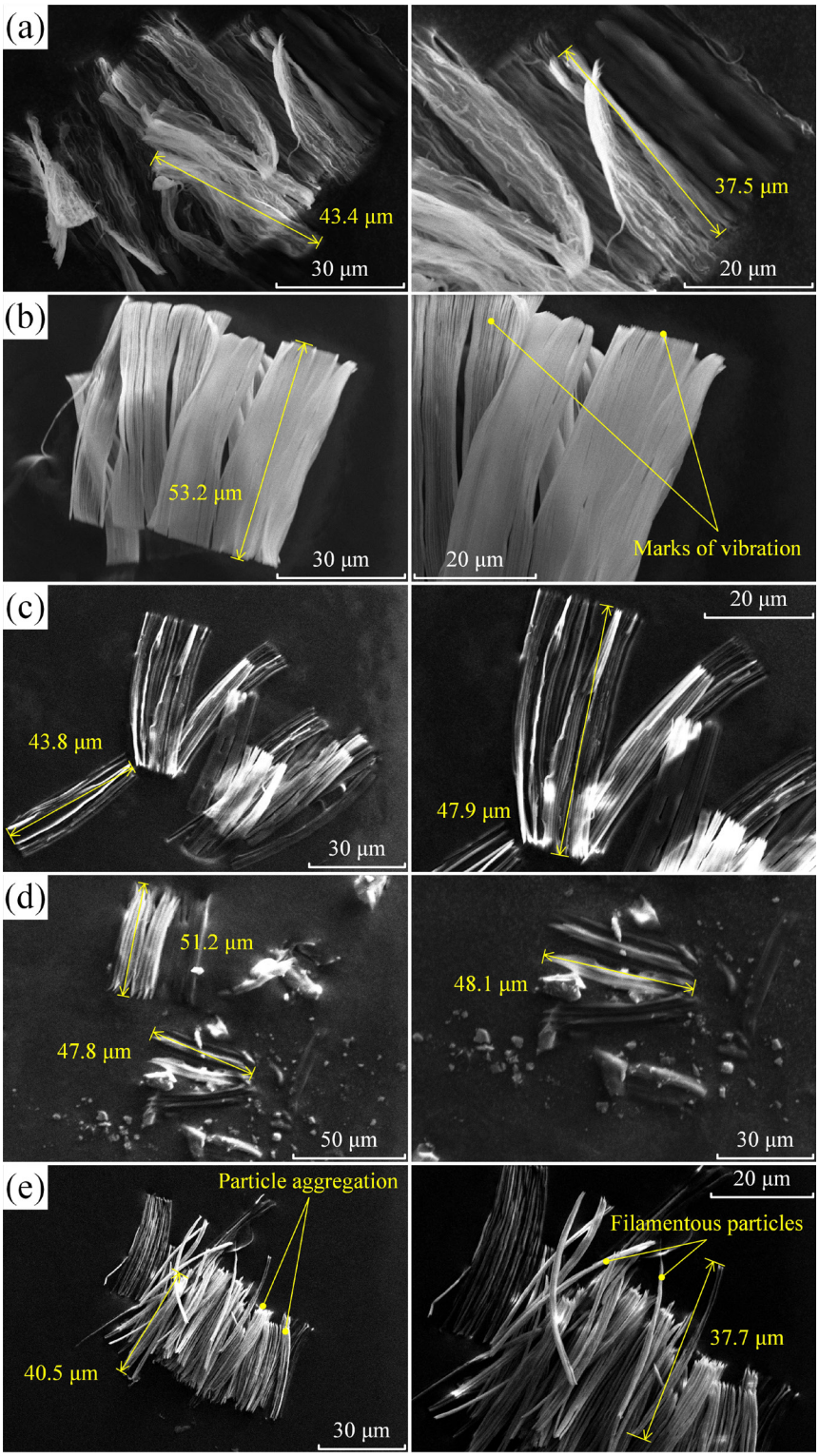

Figure 7.19 Chip morphology obtained in the experiments of set A: (a) HSR = 0.1 (θ_a = 34.5°); (b) HSR = 0.3 (θ_a = 29.5°); (c) HSR = 0.5 (θ_a = 25.6°); (d) HSR = 0.7 (θ_a = 22.6°); (e) HSR = 0.9 (θ_a = 20.3°).

As shown in Figure 7.19, the marks of vibration can be identified on the back surface of the silk chips. In the experiments of set A, the average tool velocity angle dropped gradually from 29.5° to 20.3°, as an increase in the HSR will decrease the average tool velocity angle. At the same time, the chip geometry changed from continuous to semi-continuous with the reduction of the average tool velocity angle. It became discontinuous when the average tool velocity angle approached 22.6°. In other words, the chip breakability was increased, which agrees well with the simulated trends in Section 7.4.

Thus, according to the chip morphology displayed in Figure 7.19, it can be inferred that the critical average tool velocity angle θ_c ranges from 22.6° to 25.6°. Considering both simulation and experimental results, the critical average tool velocity angle θ_c is finally determined as 22.6°. The average tool velocity angle should always be kept less than the critical value in order to achieve effective chip breaking in elliptical vibration diamond turning of silk fibroin. Moreover, despite slight particle aggregation, the filamentous silk particles were manufactured with an HSR of 0.9 (θ_a = 20.3°).

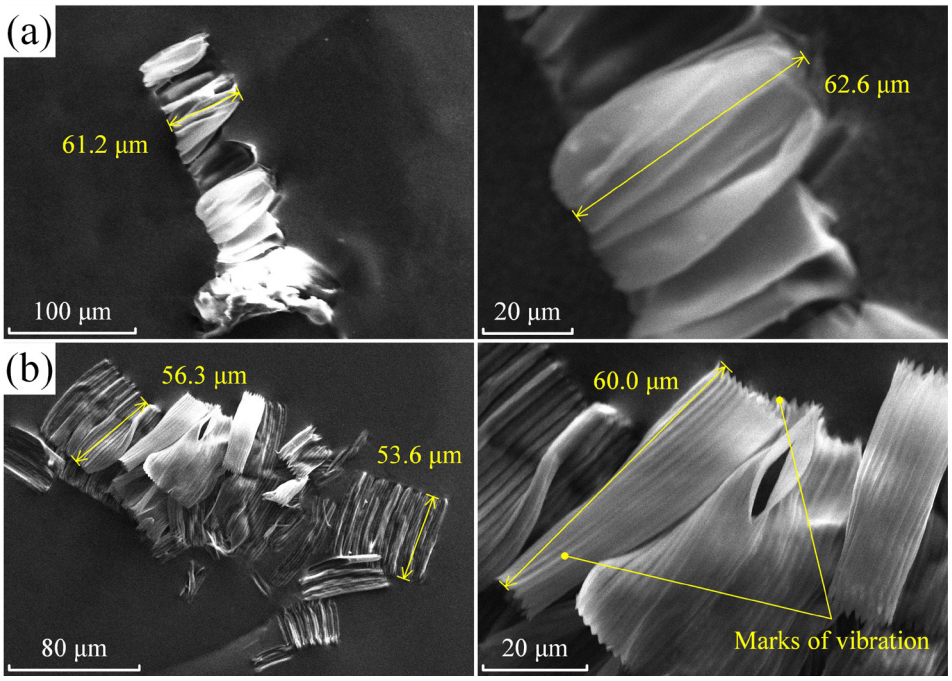

Figure 7.20 Chip morphology obtained in the experiments of set C: (a) HSR = 0.3 (θ_a = 35.0°); (b) HSR = 0.9 (θ_a = 24.0°).

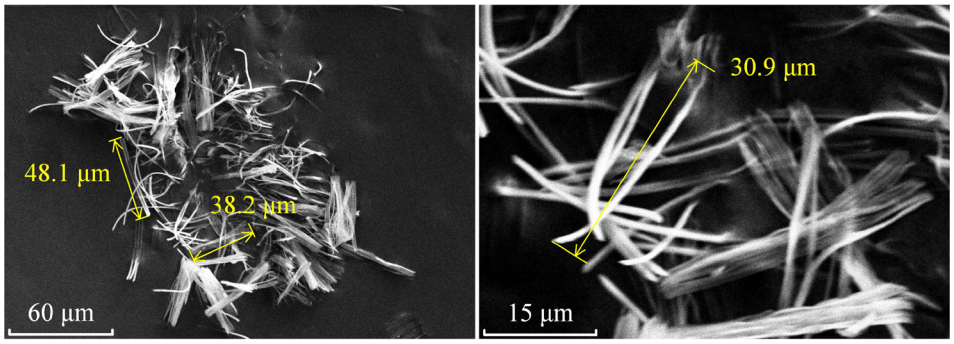

Figure 7.21 Chip morphology obtained in the experiments of set D: HSR = 0.9 (θ_a = 20.3°).

Figure 7.20 shows the chip morphology obtained with a nominal depth of cut of 0.7 µm (r_d = 0.7). In these cases, the average tool velocity angle reaches 35.0° when the HSR is 0.3. When HSR approaches 0.9, continuous chips are still generated with the

marks of vibration on the back surfaces, as the average tool velocity angle (θ_a = 24.0°) is still larger than the critical value for effective chip breaking (θ_c = 22.6°).

Compared with the obtained silk particles shown in Figure 7.19 (e), although under the same average tool velocity angle θ_a, more loose and separate filamentous silk particles were manufactured in Figure 7.21, showing that the silk chip breaks in an easier way. This can be attributed to the fact that high-frequency vibrations help the dispersion of silk particles, thus diminishing particle aggregation.

7.6 Summary

This chapter investigated the chip-breaking mechanism in elliptical vibration diamond turning of silk fibroin through machining experiments and hybrid FE-SPH numerical simulations. The filamentous silk particles were manufactured with effective chip breaking. The conclusions can be drawn as follows:

(1) The simulation results show that the cutting chip morphology is significantly influenced by the vibration frequency and amplitude in elliptical vibration diamond turning. The radius of curvature of the cutting chip decreases with the increase of vibration frequency and decrease of vibration amplitude.

(2) The chip breakage can be controlled by processing parameters such as HSR and depth ratio. Effective chip breaking can be accomplished under a large HSR and a small depth ratio due to the reduced average tool velocity angle θ_a. A decrease in the average tool velocity angle will decrease the ductility of silk fibroin due to the reduced hydrostatic pressure and the enhanced shearing action of the diamond tool. Chip breakability in elliptical vibration diamond turning of silk fibroin is increased under the combined effects of hydrostatic pressure and shearing action. The critical

average tool velocity angle θ_c for effective chip breaking is confirmed to be 22.6°, based on the experimental and simulation results. In order to obtain filamentous silk particles, the average tool velocity angle should always be kept below this critical value.

(3) A high-frequency tool vibration can suppress particle aggregation, which can be used to disperse agglomerated silk particles.

Chapter 8

Conclusions and future work

8.1 Conclusions

Silk fibroin is a sustainable and eco-friendly biomaterial with remarkable mechanical properties and biocompatibility that can meet the requirements of drug delivery and tissue regeneration. This thesis aimed to develop a manufacturing approach to obtain silk particles in the form of cutting chips with different geometries by using diamond turning. A high-frequency non-resonant elliptical vibrator was developed to achieve effective chip breaking for manufacturing filamentous silk particles. A hybrid FE-SPH numerical model was established to study the serrated chip formation mechanism in diamond turning and the chip-breaking mechanism in elliptical vibration diamond turning. Additionally, the Cowper-Symonds material parameters of silk fibroin were determined. Long helical, long ribbon and short folded silk particles were obtained, while filamentous silk particles were successfully manufactured with the aid of the developed elliptical vibrator.

The conclusions of this thesis are as follows:

(1) It is feasible to manufacture silk particles in the form of cutting chips with different geometries using diamond turning, in which the ductile mode cutting of silk fibroin can be achieved. Long helical particles were manufactured using a sharp point tool with a feed rate of less than 2.5 μm/rev. The radius of curvature of the helical silk particles can be tailored by tuning the feed rate. Long ribbon particles were generated using a round nose tool with a customised folding wavelength that could

be tailored by changing the cutting speed and depth of cut. Short and discontinuous folded particles can also be manufactured despite low dimensional consistency and particle aggregation.

(2) Chip morphology, especially shear band spacing *S*, in diamond turning of silk fibroin can be predicted with reasonable accuracy using the hybrid FE-SPH model established in this thesis. The shear band is formed through the conjunction of two parts: one part propagates from the cutting edge to the free surface, and the other part initiates on the free surface and propagates towards the cutting edge. Moreover, the chip segment is formed by the propagation of a microcrack from the free surface to the tool tip. The serrated chip formation mechanism derives from the hierarchical structure of silk fibroin. Under the high shear strain in diamond turning, the increasing number of ruptured H-bonds enables the interfaces between beta-strands to become slip planes. The accumulated interstrand slip motions further develop into shear bands, which is the dominant cause of the formation of serrated chips.

(3) The high-stiffness LSFH and NHPJ structures will allow the designed elliptical vibrator to work at an operational frequency of up to 5 kHz for diamond turning, which is higher than its non-resonant counterparts. Its vibration amplitude can reach over 2 μm, although the high-frequency and high-amplitude working modes cannot be achieved simultaneously due to the limitations of the drive capability of the current power amplifier. The developed elliptical vibrator can be used to machine structured surfaces and break cutting chips. The wavelength and height of the surface structures can be changed by adjusting the vibration frequency and amplitude of the vibrator with errors of less than 1.26% and 10.67%, respectively.

More importantly, discontinuous copper chips can be manufactured using this elliptical vibrator, thus verifying its chip-breaking effectiveness on ductile material.

(4) Elliptical vibration diamond turning can effectively break silk chips and obtain filamentous silk particles. Effective chip breaking can be accomplished under a large HSR and a small depth ratio due to the reduced average tool velocity angle θ_a. A reduction in the average tool velocity angle will decrease the ductility of silk fibroin because of the reduced hydrostatic pressure and the enhanced shearing action of the diamond tool, making the chip easy to break. The critical average tool velocity angle θ_c for chip breaking is confirmed to be 22.6°. The average tool velocity angle should always be kept below this critical value to manufacture filamentous silk particles. In addition, high-frequency tool vibration can suppress the aggregation of silk cutting chips, which can be used to disperse agglomerated silk particles.

8.2 Contributions to knowledge

The contributions to knowledge in this thesis lie in the following:

(1) Simply adjusting the processing parameters in diamond turning is ineffective for manufacturing discontinuous silk particles. Unlike common ductile materials such as aluminium and steel, the breakability of silk fibroin increases at a reduced feed rate and depth of cut due to its soft but highly tough nature. Although short and discontinuous folded silk particles were generated, the chip-breaking efficiency was extremely low. Particle aggregation with low dimensional consistency can be observed due to the ductility of silk fibroin.

(2) A new hybrid FE-SPH numerical model was proposed, and the Cowper-Symonds material parameters of silk fibroin were preliminarily determined. It has been approved that this model can reproduce the formation of serrated chips.

(3) The formation mechanism of the serrated chip in diamond turning of silk fibroin was identified. The serrated chip formation mechanism derives from the hierarchical structure of silk fibroin. The detailed chip formation mechanism has been described in Conclusion 2.

(4) HSR and depth ratio will significantly affect chip breakability in elliptical vibration diamond turning of silk fibroin by changing the average tool velocity angle. The chip-breaking mechanism for this process was also revealed (see Conclusion 4).

8.3 Limitations and future work

This thesis provides a solid foundation for manufacturing silk particles with different geometries using diamond turning. More ideas for future work to further improve the current research are as follows:

(1) Although the prototype of the elliptical vibrator can work at a frequency of 5 kHz and its vibration amplitude can reach 2 μm, the high-frequency and high-amplitude working modes cannot be reached simultaneously. A power amplifier with a higher drive capability and piezo actuators with larger stokes can be employed in the future to increase its vibration amplitude, enlarging the attainable geometries of silk particles.

(2) Currently, open-loop control is used to drive the designed elliptical vibrator. Closed-loop control should be developed to further improve tool positioning

accuracy. Thus, silk nanoparticles with high dimensional consistency can be manufactured using this chemical-free manufacturing approach.

(3) The temperature effects and strain hardening were neglected in material modelling for silk fibroin, which is one of the reasons for the underestimation of cutting force in the simulation. In addition, high viscoelasticity is another excellent mechanical property of silk fibroin, but it is also ignored in the current model. Future work could focus on the development of a material model that takes temperature, strain hardening and viscoelasticity effects into account to further improve the accuracy of the hybrid FE-SPH model.

(4) Residual stress in silk cutting chips might deteriorate the mechanical properties of silk particles. However, the measurement of residual stress has not yet been conducted due to the availability of measuring equipment. Further work is needed to develop an effective approach for measuring residual stress in silk particles.

(5) The collection of particles is another crucial issue that needs to be addressed in the future for the practical application of manufactured silk particles. One potential solution is to use the electrostatic adsorption approach, as silk particles are negatively charged. In addition, *in vitro* and *in vivo* testing of the drug delivery performance of these silk particles can be performed in the future.

References

[1] Sung H, Ferlay J, Siegel RL, Laversanne M, Soerjomataram I, Jemal A, et al. Global Cancer Statistics 2020: GLOBOCAN Estimates of Incidence and Mortality Worldwide for 36 Cancers in 185 Countries. CA Cancer J Clin 2021;71:209–49.

[2] Sun T, Zhang YS, Pang B, Hyun DC, Yang M, Xia Y. Engineered nanoparticles for drug delivery in cancer therapy. Angew Chemie - Int Ed 2014;53:12320–64.

[3] Philipp Seib F. Silk nanoparticles—an emerging anticancer nanomedicine. AIMS Bioeng 2017;4:239–58.

[4] Cao Y, Wang B. Biodegradation of silk biomaterials. Int J Mol Sci 2009;10:1514–24.

[5] Koh LD, Cheng Y, Teng CP, Khin YW, Loh XJ, Tee SY, et al. Structures, mechanical properties and applications of silk fibroin materials. Prog Polym Sci 2015;46:86–110.

[6] Colomban P, Jauzein V. Silk: Fibers, films, and composites—types, processing, structure, and mechanics. Handb. Prop. Text. Tech. Fibres, Elsevier; 2018, p. 137–83.

[7] Bessa PC, Balmayor ER, Azevedo HS, Nürnberger S, Casal M, van Griensven M, et al. Silk fibroin microparticles as carriers for delivery of human recombinant BMPs. Physical characterization and drug release. J Tissue Eng Regen Med 2010;4:349–55.

[8] Tian Y, Jiang X, Chen X, Shao Z, Yang W. Doxorubicin-loaded magnetic silk fibroin nanoparticles for targeted therapy of multidrug-resistant cancer. Adv Mater 2014;26:7393–8.

[9] Nguyen TP, Nguyen QV, Nguyen VH, Le TH, Huynh VQN, Vo DVN, et al. Silk fibroin-based biomaterials for biomedical applications: A review. Polymers (Basel) 2019;11:1–25.

[10] Reddy N, Aramwit P. Sustainable Uses of Byproducts from Silk Processing. John Wiley & Sons; 2021.

[11] Pham DT, Saelim N, Tiyaboonchai W. Alpha mangostin loaded crosslinked silk fibroin-based nanoparticles for cancer chemotherapy. Colloids Surfaces B Biointerfaces 2019;181:705–13.

[12] Lammel AS, Hu X, Park S-H, Kaplan DL, Scheibel TR. Controlling silk fibroin particle features for drug delivery. Biomaterials 2010;31:4583–91.

[13] Qu J, Liu Y, Yu Y, Li J, Luo J, Li M. Silk fibroin nanoparticles prepared by electrospray as controlled release carriers of cisplatin. Mater Sci Eng C Mater Biol Appl 2014;44:166–74.

[14] Wenk E, Wandrey AJ, Merkle HP, Meinel L. Silk fibroin spheres as a platform for controlled drug delivery. J Control Release 2008;132:26–34.

[15] Pham DT, Tiyaboonchai W. Fibroin nanoparticles: a promising drug delivery system. Drug Deliv 2020;27:431–48.

[16] Rajkhowa R, Wang L, Wang X. Ultra-fine silk powder preparation through rotary and ball milling. Powder Technol 2008;185:87–95.

[17] Kazemimostaghim M, Rajkhowa R, Tsuzuki T, Wang X. Production of submicron silk particles by milling. Powder Technol 2013;241:230–5.

[18] Zhong S, Cui H, Chen Z, Wooley KL, Pochan DJ. Helix self-assembly through the coiling of cylindrical micelles. Soft Matter 2007;4:90–3.

[19] Petros RA, Desimone JM. Strategies in the design of nanoparticles for therapeutic applications. Nat Rev Drug Discov 2010;9:615–27.

[20] Decuzzi P, Godin B, Tanaka T, Lee SY, Chiappini C, Liu X, et al. Size and shape effects in the biodistribution of intravascularly injected particles. J Control Release 2010;141:320–7.

[21] Truong NP, Whittaker MR, Mak CW, Davis TP. The importance of nanoparticle shape in cancer drug delivery. Expert Opin Drug Deliv 2015;12:129–42.

[22] Imsombut T, Srisuwan Y, Srihanam P, Baimark Y. Genipin-cross-linked silk fibroin microspheres prepared by the simple water-in-oil emulsion solvent diffusion method. Powder Technol 2010;203:603–8.

[23] Baimark Y, Srisa-ard M, Srihanam P. Morphology and thermal stability of silk fibroin/starch blended microparticles. Express Polym Lett 2010;4:781–9.

[24] YAN J, SYOJI K, KURIYAGAWA T. Chip Morphology of Ultra-Precision Diamond Turning of Single Crystal Slicon. J Japan Soc Precis Eng 1999;65:1008–12.

[25] Huang W, Yan J. Surface formation mechanism in ultraprecision diamond turning of coarse-grained polycrystalline ZnSe. Int J Mach Tools Manuf 2020;153:103554.

[26] Mukaida M, Yan J. Ductile machining of single-crystal silicon for microlens arrays by ultraprecision diamond turning using a slow tool servo. Int J Mach Tools Manuf 2017;115:2–14.

[27] Cheng Y, Koh LD, Li D, Ji B, Han MY, Zhang YW. On the strength of β-sheet crystallites of Bombyx mori silk fibroin. J R Soc Interface 2014;11.

[28] Duncan R, Richardson SCW. Endocytosis and intracellular trafficking as gateways for nanomedicine delivery: opportunities and challenges. Mol Pharm 2012;9:2380–402.

[29] Narayanan KB, Han SS. Helical plant viral nanoparticles—bioinspired synthesis of nanomaterials and nanostructures. Bioinspir Biomim 2017;12:031001.

[30] Geng Y, Dalhaimer P, Cai S, Tsai R, Tewari M, Minko T, et al. Shape effects of filaments versus spherical particles in flow and drug delivery. Nat Nanotechnol 2007;2:249–55.

[31] Petros RA, DeSimone JM. Strategies in the design of nanoparticles for therapeutic applications. Nat Rev Drug Discov 2010;9:615–27.

[32] Mwangi TK, Bowles RD, Tainter DM, Bell RD, Kaplan DL, Setton LA. Synthesis and characterization of silk fibroin microparticles for intra-articular drug delivery. Int J Pharm 2015;485:7–14.

[33] Kohane DS. Microparticles and nanoparticles for drug delivery. Biotechnol Bioeng 2007;96:203–9.

[34] Kohane DS, Langer R, Kinney RC, Lipp M, Lotan N, Louis DN. Biocompatibility of lipid-protein-sugar particles containing bupivacaine in the epineurium. J Biomed Mater Res 2002;59:450–9.

[35] Jared BH, Dow TA. Investigation of the direction of chip motion in diamond turning. Precis Eng 2001;25:155–64.

[36] Jared BH, Dow TA. Investigation and prediction of chip geometry in diamond turning. Precis Eng 2000;24:88–96.

[37] Yılmaz B, Karabulut Ş, Güllü A. A review of the chip breaking methods for continuous chips in turning. J Manuf Process 2020;49:50–69.

[38] Jawahir IS. Chip-Forms, Chip Breakability, and Chip Control. CIRP Encycl. Prod. Eng., vol. 113, Berlin, Heidelberg: Springer Berlin Heidelberg; 2018, p. 1–16.

[39] Jawahir IS, van Luttervelt CA. Recent Developments in Chip Control Research and Applications. CIRP Ann - Manuf Technol 1993;42:659–93.

[40] Guo YB, Yen DW. A FEM study on mechanisms of discontinuous chip formation in hard machining. J Mater Process Technol 2004;155–156:1350–6.

[41] NAKAYAMA K. A Study on Chip-breaker. Bull JSME 1962;5:142–50.

[42] Li Z, Rong Y. A STUDY ON CHIP BREAKING LIMITS IN MACHINING. Mach Sci Technol 1999;3:25–48.

[43] Zhou L. Machining Chip-Breaking Prediction with Grooved Inserts in Steel Turning. PhD Thesis,Worcester Polytech Inst 2001.

[44] Wu M, Yu A, Chen Q, Wang Y, Yuan J, Sun L, et al. Design of adjustable chip breaker for PCD turning tools. Int J Mech Sci 2020;172.

[45] Brehl DE, Dow TA. Review of vibration-assisted machining. Precis Eng 2008;32:153–72.

[46] Negishi N. Elliptical Vibration Assisted Machining with Single Crystal Diamond Tools. MS Diss North Carolina State Univ 2003.

[47] Kim J Du, Choi IH. Characteristics of chip generation by ultrasonic vibration cutting with extremely low cutting velocity. Int J Adv Manuf Technol 1998;14:2–6.

[48] Ezugwu EO, Bonney J. Effect of high-pressure coolant supply when machining nickel-base, Inconel 718, alloy with coated carbide tools. J Mater Process Technol 2004;153–154:1045–50.

[49] Guo P, Ehmann KF. Development of a tertiary motion generator for elliptical vibration texturing. Precis Eng 2013;37:364–71.

[50] Wang J, Liao WH, Guo P. Modulated ultrasonic elliptical vibration cutting for ductile-regime texturing of brittle materials with 2-D combined resonant and non-resonant vibrations. Int J Mech Sci 2020;170:105347.

[51] Zhang J, Cui T, Ge C, Sui Y, Yang H. Review of micro/nano machining by utilizing elliptical vibration cutting. Int J Mach Tools Manuf 2016;106:109–26.

[52] Moriwaki T, Shamoto E. Ultrasonic Elliptical Vibration Cutting. CIRP Ann 1995;44:31–4.

[53] Suzuki N, Haritani M, Yang J, Hino R, Shamoto E. Elliptical vibration cutting of tungsten alloy molds for optical glass parts. CIRP Ann - Manuf Technol 2007;56:127–30.

[54] Yang Z, Zhu L, Zhang G, Ni C, Lin B. Review of ultrasonic vibration-assisted machining in advanced materials. Int J Mach Tools Manuf 2020;156:103594.

[55] Zheng L, Chen W, Huo D. Review of vibration devices for vibration-assisted machining. Int J Adv Manuf Technol 2020;108:1631–51.

[56] Loh BG, Kim GD. Correcting distortion and rotation direction of an elliptical trajectory in elliptical vibration cutting by modulating phase and relative magnitude of the sinusoidal excitation voltages. Proc Inst Mech Eng Part B J Eng Manuf 2012;226:813–23.

[57] Hong MS, Ehmann KF. Generation of engineered surfaces by the surface-shaping system. Int J Mach Tools Manuf 1995;35:1269–90.

[58] Heamawatanachai S, Bamberg E. Design and characterization of a PZT driven micromachining tool based on single-point tool tip geometry. Precis Eng 2009;33:387–94.

[59] Zhu W Le, Zhu Z, He Y, Ehmann KF, Ju BF, Li S. Development of a Novel 2-D Vibration-Assisted Compliant Cutting System for Surface Texturing. IEEE/ASME Trans Mechatronics 2017;22:1796–806.

[60] Yuan Y, Zhang D, Jing X, Zhu H, Zhu W Le, Cao J, et al. Fabrication of hierarchical freeform surfaces by 2D compliant vibration-assisted cutting. Int J Mech Sci 2019;152:454–64.

[61] Ahn J-H, Lim H-S, Son S-M. Improvement of micro-machining accuracy by 2-dimensional vibration cutting. Proc ASPE, vol. 20, 1999, p. 150–3.

[62] Han J, Lin J, Li Z, Lu M, Zhang J. Design and Computational Optimization of Elliptical Vibration-Assisted Cutting System With a Novel Flexure Structure. IEEE Trans Ind Electron 2019;66:1151–61.

[63] Wang J, Du H, Gao S, Yang Y, Zhu Z, Guo P. An ultrafast 2-D non-resonant cutting tool for texturing micro-structured surfaces. J Manuf Process 2019;48:86–97.

[64] Cerniway M. Elliptical diamond milling: kinematics, force and tool wear. MS Diss North Carolina State Univ 2001.

[65] Buchkremer S, Klocke F, Veselovac D. 3D FEM simulation of chip breakage in metal cutting. Int J Adv Manuf Technol 2016;82:645–61.

[66] Silberschmidt V V. Mechanics of Materials in Modern Manufacturing Methods and Processing Techniques. Elsevier; 2020.

[67] Strand RK. Smoothed Particle Hydrodynamics Modelling for Failure in Metals. PhD Thesis,Cranf Univ 2010.

[68] Liu MB, Liu GR. Smoothed particle hydrodynamics (SPH): An overview and recent developments. vol. 17. 2010.

[69] Monaghan JJ, Lattanzio JC. A refined particle method for astrophysical problems. Astron Astrophys 1985;149:135–43.

[70] Liu G-R, Liu MB. Smoothed particle hydrodynamics: a meshfree particle method. World scientific; 2003.

[71] Monaghan JJ. Smoothed particle hydrodynamics. Annu Rev Astron Astrophys 1992;30:543–74.

[72] Danilewicz A, Sikora Z. Numerical simulation of crater creating process in dynamic replacement method by smooth particle hydrodynamics. Stud Geotech Mech 2015;36:3–8.

[73] Limido J, Espinosa C, Salaun M, Mabru C, Chieragatti R, Lacome JL. Metal cutting modelling SPH approach. Int J Mach Mach Mater 2011;9:177.

[74] RUTTIMANN N, BUHL S, WEGENER K. Simulation of Single Grain Cutting Using Sph Method. J Mach Eng 2010;10:17–29.

[75] Rüttimann N, Roethlin M, Buhl S, Wegener K. Simulation of hexa-octahedral diamond grain cutting tests using the SPH method. Procedia CIRP 2013;8:322–7.

[76] Umer U, Mohammed MK, Qudeiri JA, Al-Ahmari A. Assessment of finite element and smoothed particles hydrodynamics methods for modeling serrated chip formation in hardened steel. Adv Mech Eng 2016;8:168781401665237.

[77] Shao JR, Li HQ, Liu GR, Liu MB. An improved SPH method for modeling liquid sloshing dynamics. Comput Struct 2012;100–101:18–26.

[78] Johnson GR, Beissel SR. Normalized smoothing functions for sph impact computations. Int J Numer Methods Eng 1996;39:2725–41.

[79] Zhang GM, Batra RC. Modified smoothed particle hydrodynamics method and its application to transient problems. Comput Mech 2004;34:137–46.

[80] Liu MB, Xie WP, Liu GR. Modeling incompressible flows using a finite particle method. Appl Math Model 2005;29:1252–70.

[81] Dilts GA. Moving-Least-Squares-particle hydrodynamics - I. Consistency and stability. Int J Numer Methods Eng 1999;44:1115–55.

[82] Chen JK, Beraun JE, Carney TC. A corrective smoothed particle method for boundary value problems in heat conduction. Int J Numer Methods Eng 1999;46:231–52.

[83] Wing Kam L, Sukky J, Yi Fei Z. Reproducing kernel particle methods. Int J Numer Methods Fluids 1995;20:1081–106.

[84] Randles PW, Libersky LD. Smoothed particle hydrodynamics: some recent improvements and applications. Comput Methods Appl Mech Eng 1996;139:375–408.

[85] Vila JP. SPH renormalized hybrid methods for conservation laws: applications to free surface flows. Meshfree methods Partial Differ. equations II, Springer; 2005, p. 207–29.

[86] Espinosa C, Lacome J-L, Limido J, Salaün M, Mabru C, Chieragatti R. Modelling High Speed Machining with the SPH Method 2008.

[87] Umer U, Qudeiri JA, Ashfaq M, AL-Ahmari A. Chip morphology predictions while machining hardened tool steel using finite element and smoothed particles hydrodynamics methods. J Zhejiang Univ A 2016;17:873–85.

[88] Colagrossi A, Landrini M. Numerical simulation of interfacial flows by smoothed particle hydrodynamics. J Comput Phys 2003;191:448–75.

[89] Dong XW, Liu GR, Li Z, Zeng W. A smoothed particle hydrodynamics (SPH) model for simulating surface erosion by impacts of foreign particles. Tribol Int 2016;95:267–78.

[90] Feng Y, Jianming W, Feihong L. Numerical simulation of single particle acceleration process by SPH coupled FEM for abrasive waterjet cutting. Int J Adv Manuf Technol 2012;59:193–200.

[91] Wang J, Liu F, Yu F, Zhang G. Shot peening simulation based on SPH method. Int J Adv Manuf Technol 2011;56:571–8.

[92] Takaffoli M, Papini M. Material deformation and removal due to single particle impacts on ductile materials using smoothed particle hydrodynamics. Wear 2012;274–275:50–9.

[93] Xi Y, Bermingham M, Wang G, Dargusch M. SPH/FE modeling of cutting force and chip formation during thermally assisted machining of Ti6Al4V alloy. Comput Mater Sci 2014;84:188–97.

[94] Abolfazl Zahedi S, Demiral M, Roy A, Silberschmidt V V. FE/SPH modelling of orthogonal micro-machining of f.c.c. single crystal. Comput Mater Sci 2013;78:104–9.

[95] Attaway SW, Heinstein MW, Swegle JW. Coupling of smooth particle hydrodynamics with the finite element method. Nucl Eng Des 1994;150:199–205.

[96] Campbell J, Vignjevic R, Libersky L. A contact algorithm for smoothed particle hydrodynamics. Comput Methods Appl Mech Eng 2000;184:49–65.

[97] Johnson GR. Linking of Lagrangian particle methods to standard finite element methods for high velocity impact computations. Nucl Eng Des 1994;150:265–74.

[98] Belytschko T, Liu WK, Moran B, Elkhodary K. Nonlinear finite elements for continua and structures. John wiley & sons; 2013.

[99] Limido J, Espinosa C, Salaun M, Lacome J-L. A new approach of high speed cutting modelling: SPH method. J. Phys. IV, vol. 134, EDP sciences; 2006, p. 1195–200.

[100] Geng X, Dou W, Deng J, Ji F, Yue Z. Simulation of the orthogonal cutting of OFHC copper based on the smoothed particle hydrodynamics method. Int J Adv Manuf Technol 2017;91:265–72.

[101] Clausen AH, Børvik T, Hopperstad OS, Benallal A. Flow and fracture characteristics of aluminium alloy AA5083–H116 as function of strain rate, temperature and triaxiality. Mater Sci Eng A 2004;364:260–72.

[102] Johnson GR. A constitutive model and data for materials subjected to large strains, high strain rates, and high temperatures. Proc 7th Inf Sympo Ballist 1983:541–7.

[103] Olleak AA, Nasr MNA, El-hofy HA. The Influence of Johnson-Cook Parameters on SPH Modeling of Orthogonal Cutting of AISI 316L. 10th Eur LS-DYNA Conf 2015.

[104] Chandrasekaran H, M'saoubi R, Chazal H. Modelling of material flow stress in chip formation process from orthogonal milling and split Hopkinson bar tests. Mach Sci Technol 2005;9:131–45.

[105] Tounsi N, Vincenti J, Otho A, Elbestawi MA. From the basic mechanics of orthogonal metal cutting toward the identification of the constitutive equation. Int J Mach Tools Manuf 2002;42:1373–83.

[106] Changeux B, Touratier M, Lebrun J-L, Thomas T, Clisson J. High-speed shear tests for the identification of the Johnson-Cook law. 4 th Int. ESAFORM Conf. Mater. Form., 2001, p. 603–6.

[107] Calamaz M, Limido J, Nouari M, Espinosa C, Coupard D, Salaün M, et al. Toward a better understanding of tool wear effect through a comparison between experiments and SPH numerical modelling of machining hard materials. Int J Refract Met Hard Mater 2009;27:595–604.

[108] Lesuer DR, Kay GJ, LeBlanc MM. Modeling large-strain, high-rate deformation in metals. Lawrence Livermore National Lab., CA (US); 2001.

[109] Lee W-S, Lin C-F. High-temperature deformation behaviour of Ti6Al4V alloy evaluated by high strain-rate compression tests. J Mater Process Technol 1998;75:127–36.

[110] Özel T, Zeren E. Determination of work material flow stress and friction for FEA of machining using orthogonal cutting tests. J Mater Process Technol 2004;153:1019–25.

[111] Meyer Jr HW, Kleponis DS. Modeling the high strain rate behavior of titanium undergoing ballistic impact and penetration. Int J Impact Eng 2001;26:509–21.

[112] Liang, Mi, Wang, Zhou, Wu, Zhao. Numerical investigations on the grinding forces in ultrasonic assisted grinding of SiC ceramics by using SPH method. Adv Mater Res 2014;1017:735–40.

[113] Lv D, Zhang Y. Numerical simulation of chipping formation process with smooth particle hydrodynamic (SPH) method for diamond drilling AIN ceramics. Int J Adv Manuf Technol 2018;96:2257–69.

[114] Tang Z, Liu FJ, Guo SH, Chang J, Zhang JJ. Evaluation of coupled finite element/meshfree method for a robust full-scale crashworthiness simulation of railway vehicles. Adv Mech Eng 2016;8:1–13.

[115] Zhu BL, Guo YL, Zhou P, Bradford MA, Pi YL. Numerical and experimental studies of corrugated-web-connected buckling-restrained braces. Eng Struct 2017;134:107–24.

[116] Abdalla HF, Megahed MM, Younan MYA. Shakedown Limit Loads for 90 Degree Scheduled Pipe Bends Subjected to Steady Internal Pressure and Cyclic Bending Moments. J Press Vessel Technol 2011;133.

[117] Fernandes MG, Fonseca EM, Jorge RN. Thermo-mechanical stresses distribution on bone drilling: Numerical and experimental procedures. Proc Inst Mech Eng Part L J Mater Des Appl 2019;233:637–46.

[118] Cowper GR, Symonds PS. Strain-hardening and strain-rate effects in the impact loading of cantilever beams. Brown Univ Providence Ri; 1957.

[119] Calamaz M, Coupard D, Girot F. A new material model for 2D numerical simulation of serrated chip formation when machining titanium alloy Ti-6Al-4V. Int J Mach Tools Manuf 2008;48:275–88.

[120] Niu W, Mo R, Chang Z, Wan N. Investigating the effect of cutting parameters of Ti-6Al-4V on surface roughness based on a SPH cutting model. Appl Sci 2019;9.

[121] Shchurov IA, Nikonov AV, Boldyrev IS. SPH-Simulation of the Fiber-reinforced Composite Workpiece Cutting for the Surface Quality Improvement. Procedia Eng 2016;150:860–5.

[122] Islam S, Ibrahim R, Das R, Fagan T. Novel approach for modelling of nanomachining using a mesh-less method. Appl Math Model 2012;36:5589–602.

[123] Wilkins ML. Calculation of elastic-plastic flow. California Univ Livermore Radiation Lab; 1963.

[124] Li S, Zahedi A, Silberschmidt V. Numerical Simulation of Bone Cutting: Hybrid SPH–FE Approach. Numer. Methods Adv. Simul. Biomech. Biol. Process., Elsevier; 2018, p. 187–201.

[125] Abolfazl Zahedi S, Demiral M, Roy A, Silberschmidt V V. FE/SPH modelling of orthogonal micro-machining of f.c.c. single crystal. Comput Mater Sci 2013;78:104–9.

[126] Inglis HM, Geubelle PH, Matouš K, Tan H, Huang Y. Cohesive modeling of dewetting in particulate composites: micromechanics vs. multiscale finite element analysis. Mech Mater 2007;39:580–95.

[127] Heisel U, Zaloga W, Krivoruchko D, Storchak M, Goloborodko L. Modelling of orthogonal cutting processes with the method of smoothed particle hydrodynamics. Prod Eng 2013;7:639–45.

[128] Schwer LE, Hacker K, Poe K. Perforation of Metal Plates: Laboratory Experiments and Numerical Simulations. 9th Int LS-DYNA Users Conf 2006:1–12.

[129] Kaselouris E, Papadoulis T, Variantza E, Baroutsos A, Dimitriou V. A study of explicit numerical simulations in orthogonal metal cutting. Solid State Phenom 2017;261 SSP:339–46.

[130] Takabi B, Tajdari M, Tai BL. Numerical study of smoothed particle hydrodynamics method in orthogonal cutting simulations – Effects of damage criteria and particle density. J Manuf Process 2017;30:523–31.

[131] Rosswog S, Villumsen MF, Fauerholdt TG. Simulation of Metal Cutting using Smooth Particle Hydrodynamics. Analysis 2008;53:17–36.

[132] Zienkiewicz OC, Godbole PN. Flow of plastic and visco-plastic solids with special reference to extrusion and forming processes. Int J Numer Methods Eng 1974;8:1–16.

[133] Movahhedy M, Gadala MS, Altintas Y. Simulation of the orthogonal metal cutting process using an arbitrary Lagrangian–Eulerian finite-element method. J Mater Process Technol 2000;103:267–75.

[134] Nasr MNA, Ng E-G, Elbestawi MA. Modelling the effects of tool-edge radius on residual stresses when orthogonal cutting AISI 316L. Int J Mach Tools Manuf 2007;47:401–11.

[135] Islam A. Determination of the Deformation State of a Ti-6Al-4V Alloy Subjected to Orthogonal Cutting Using Experimental and Numerical Methods 2012.

[136] Akarca S, Altenhof W, Alpas A. A Smoothed-Particle Hydrodynamics (SPH) Model for Machining of 1100 Aluminum. DynalookCom 2008:1–8.

[137] Akarca SS, Song X, Altenhof WJ, Alpas AT. Deformation behaviour of aluminium during machining: Modelling by Eulerian and smoothed-particle hydrodynamics methods. Proc Inst Mech Eng Part L J Mater Des Appl 2008;222:209–21.

[138] Zhao H, Liu C, Cui T, Tian Y, Shi C, Li J, et al. Influences of sequential cuts on micro-cutting process studied by smooth particle hydrodynamic (SPH). Appl Surf Sci 2013;284:366–71.

[139] Balbaa MA, Nasr MNA. Prediction of Residual Stresses after Laser-assisted Machining of Inconel 718 Using SPH. Procedia CIRP 2015;31:19–23.

[140] Liu Y, Li B, Wu C, Zheng Y. Simulation-based evaluation of surface micro-cracks and fracture toughness in high-speed grinding of silicon carbide ceramics. Int J Adv Manuf Technol 2016;86:799–808.

[141] Zhu D, Yan S, Li B. Single-grit modeling and simulation of crack initiation and propagation in SiC grinding using maximum undeformed chip thickness. Comput Mater Sci 2014;92:13–21.

[142] Holmquist TJ, Johnson GR. Response of silicon carbide to high velocity impact. J Appl Phys 2002;91:5858–66.

[143] Holmquist TJ, Johnson GR. Characterization and evaluation of silicon carbide for high-velocity impact. J Appl Phys 2005;97:93502.

[144] Limido J, Espinosa C, Salaün M, Lacome JL. SPH method applied to high speed cutting modelling. Int J Mech Sci 2007;49:898–908.

[145] Guo X, Wei Y, Jin Z, Guo D. Simulation research on diamond cutting of mold steel using SPH method. 2011 Int Conf Opt Instruments Technol Solid State Light Disp Technol Hologr Speckle Pattern Interferom Micro/Nano Manuf Metrol 2011;8202:82020O.

[146] Shen, Wang, Yang. Coupled FE-SPH simulation of a high-speed grinding process using a multiple-grain model. Adv Mater Res 2014;989–994:3248–51.

[147] Demiral M. SPH modeling of vibro-assisted turning of Ti alloy: Influence of vibration parameters. J Vibroengineering 2014;16:2685–94.

[148] Duan N, Yu Y, Wang W, Xu X. SPH and FE coupled 3D simulation of monocrystal SiC scratching by single diamond grit. Int J Refract Met Hard Mater 2017;64:279–93.

[149] Liu Y, Li B, Wu C, Kong L, Zheng Y. Smoothed particle hydrodynamics simulation and experimental analysis of SiC ceramic grinding mechanism. Ceram Int 2018;44:12194–203.

[150] Nam J, Kim T, Cho SW. A numerical cutting model for brittle materials using smooth particle hydrodynamics. Int J Adv Manuf Technol 2016;82:133–41.

[151] Guo X, Wei Y, Jin Z, Guo D, Maosen W. A numerical model for optical glass cutting based on SPH method. Int J Adv Manuf Technol 2013;68:1277–83.

[152] Zahedi SA, Roy A, Silberschmidt V V. Modelling of vibration assisted machining f.c.c single crystal. Procedia CIRP 2015;31:393–8.

[153] Xi Y, Bermingham M, Wang G, Dargusch M. SPH/FE modeling of cutting force and chip formation during thermally assisted machining of Ti6Al4V alloy. Comput Mater Sci 2014;84:188–97.

[154] Lucca DA, Rhorer RL, Komanduri R. Energy Dissipation in the Ultraprecision Machining of Copper. CIRP Ann - Manuf Technol 1991;40:69–72.

[155] Furukawa Y, Moronuki N. Effect of Material Properties on Ultra Precise Cutting Processes. CIRP Ann - Manuf Technol 1988;37:113–6.

[156] Gubbels GPH. Diamond turning of glassy polymers. 2006.

[157] Sima M, Özel T. Modified material constitutive models for serrated chip formation simulations and experimental validation in machining of titanium alloy Ti-6Al-4V. Int J Mach Tools Manuf 2010;50:943–60.

[158] Zhang S, Zhang H, Zong W. Modeling and simulation on the effect of tool rake angle in diamond turning of KDP crystal. J Mater Process Technol 2019;273:116259.

[159] Kitagawa T, Yabuki K. Physical properties of silk fibroin/chitosan blend films. J Appl Polym Sci 2001;80:928–34.

[160] Choi Y, Cho SY, Heo S, Jin HJ. Enhanced mechanical properties of silk fibroin-based composite plates for fractured bone healing. Fibers Polym 2013;14:266–70.

[161] White RD, Gray C, Mandelup E, Amsden JJ, Kaplan DL, Omenetto FG. Rapid nano impact printing of silk biopolymer thin films. J Micromechanics Microengineering 2011;21.

[162] Lee WB, Wang H, Chan CY, To S. Finite element modelling of shear angle and cutting force variation induced by material anisotropy in ultra-precision diamond turning. Int J Mach Tools Manuf 2013;75:82–6.

[163] Fragassa C, Topalovic M, Pavlovic A, Vulovic S. Dealing with the effect of air in fluid structure interaction by coupled SPH-FEM methods. Materials (Basel) 2019;12.

[164] Choung J, Nam W, Lee JY. Dynamic hardening behaviors of various marine structural steels considering dependencies on strain rate and temperature. Mar Struct 2013;32:49–67.

[165] Lu Y, Liu K, Wang Z, Tang W. Dynamic behavior of scaled tubular K-joints subjected to impact loads. Mar Struct 2020;69:102685.

[166] Yang H, Yang X, Varma AH, Zhu Y. Strain-Rate Effect and Constitutive Models for Q550 High-Strength Structural Steel. J Mater Eng Perform 2019;28:6626–37.

[167] Keten S, Buehler MJ. Geometric confinement governs the rupture strength of h-bond assemblies at a critical length scale. Nano Lett 2008;8:743–8.

[168] Keten S, Bertaud J, Sen D, Xu Z, Ackbarow T, Buehler MJ. Multiscale Modeling of Biological Protein Materials – Deformation and Failure, 2010, p. 473–533.

[169] Keten S, Xu Z, Ihle B, Buehler MJ. Nanoconfinement controls stiffness, strength and mechanical toughness of B-sheet crystals in silk. Nat Mater 2010;9:359–67.

[170] Krasnov I, Diddens I, Hauptmann N, Helms G, Ogurreck M, Seydel T, et al. Mechanical properties of silk: Interplay of deformation on macroscopic and molecular length scales. Phys Rev Lett 2008;100:2–5.

[171] Paros JM, Weisbord L. How to design flexure hinges. Mach Des 1965;37:151–6.

[172] Lin J, Han J, Lu M, Yu B, Gu Y. Design, analysis and testing of a new piezoelectric tool actuator for elliptical vibration turning. Smart Mater Struct 2017;26:85008.

[173] Zhou M, Eow YT, Ngoi BKA, Lim EN. Vibration-Assisted Precision Machining of Steel with PCD Tools. Mater Manuf Process 2003;18:825–34.

[174] Chen W, Zheng L, Teng X, Yang K, Huo D. Cutting Mechanism Investigation in Vibration-Assisted Machining. Nanomanufacturing Metrol 2018;1:268–76.

[175] Chen K, Si C, Guo P. Design of a High Bandwidth Nonresonant Tertiary Motion Generator for Elliptical Vibration Texturing. J Micro Nano-Manufacturing 2017;5:11008.

[176] Yong YK, Lu T-F, Handley DC. Review of circular flexure hinge design equations and derivation of empirical formulations. Precis Eng 2008;32:63–70.

[177] Raghavendra MRA, Kumar AS, Jagdish BN. Design and analysis of flexure-hinge parameter in microgripper. Int J Adv Manuf Technol 2010;49:1185–93.

[178] Yong YK, Lu TF. Comparison of circular flexure hinge design equations and the derivation of empirical stiffness formulations. IEEE/ASME Int Conf Adv Intell Mechatronics, AIM 2009:510–5.

[179] Xu C, Luo Z, Hu X, Jiang W. Finite element fatigue analysis of rectangular clutch spring of automatic slack adjuster. In: Cui J, Tan J, Wen X, editors. Ninth Int. Symp. Precis. Eng. Meas. Instrum., vol. 9446, International Society for Optics and Photonics; 2015, p. 94461E.

[180] Pallarés-Santasmartas L, Albizuri J, Avilés A, Avilés R. Mean Stress Effect on the Axial Fatigue Strength of DIN 34CrNiMo6 Quenched and Tempered Steel. Metals (Basel) 2018;8:213.

[181] Li G, Che L, Wang B, Ding F, Zhang CF. Experimental study on elliptical vibration cutting for optical microstructures. 7th Int Symp Adv Opt Manuf Test Technol Des Manuf Test Micro- Nano-Optical Devices Syst 2014;9283:928304.

[182] Miguélez MH, Soldani X, Molinari A. Analysis of adiabatic shear banding in orthogonal cutting of Ti alloy. Int J Mech Sci 2013;75:212–22.

[183] Mediavilla J, Peerlings RHJ, Geers MGD. A nonlocal triaxiality-dependent ductile damage model for finite strain plasticity. Comput Methods Appl Mech Eng 2006;195:4617–34.

[184] Wang J, Yang Y, Zhu Z, Wang Y, Liao W-H, Guo P. On ductile-regime elliptical vibration cutting of silicon with identifying the lower bound of practical nominal cutting velocity. J Mater Process Technol 2020:116720.

[185] Zhang X, Senthil Kumar A, Rahman M, Nath C, Liu K. An analytical force model for orthogonal elliptical vibration cutting technique. J Manuf Process 2012;14:378–87.

[186] Niknam SA, Zedan Y, Songmene V. Machining Burrs Formation & Deburring of Aluminium Alloys. Light Met. Alloy. Appl., InTech; 2014, p. 99–122.

[187] Aurich JC, Dornfeld D, Arrazola PJ, Franke V, Leitz L, Min S. Burrs-Analysis, control and removal. CIRP Ann - Manuf Technol 2009;58:519–42.